ABSTRACT

Title of dissertation: TOWARDS LOW-FREQUENCY SQUEEZED LIGHT AND ITS APPLICATIONS WITH FOUR-WAVE MIXING IN RUBIDIUM VAPOR

Meng-Chang Wu
Doctor of Philosophy, 2020

Dissertation directed by: Dr. Paul D. Lett
Joint Quantum Institute,
National Institute of Standards and Technology
and the University of Maryland

We study a variety of mechanisms that introduce noise into squeezed light generated by a four-wave mixing (4WM) process in Rb vapor. The noise from the seeding beam itself is a general noise that appears in any squeezed light generated from a seeding process. This noise dominates in the squeezed light at acoustic and lower measurement frequencies. A second excess noise source is observed in the twin beams pumped by either a diode laser system or a Ti:sapphire laser system. This excess noise is much stronger in the diode laser systems. It is present in the twin beams at measurement frequencies when the 4WM gain is reduced toward unity. Most of this excess noise can be removed with a dual-seeded 4WM scheme. A third noise source we examine is from a two-beam coupling that degrades the squeezing of the dual-seeded 4WM process at low frequencies of the order of the atomic transition linewidth. This noise can be avoided by seeding skew rays in the 4WM gain region. This gives us an insight to solve this "cross talk" problem by imaging the source

in the 4WM gain region. In addition to studying noise sources, we propose a gain-independent calibration scheme that relies on higher order correlation function for the absolute calibration of photodiodes.

Having low frequency squeezing is really important if we record quantum images with a CCD camera, which has a slow shutter speed. Also, it's been very difficult for people to get low-frequency squeezing. We obtain a record level of low-frequency squeezing using a simple dual-seeding technique. With this study of noise sources we are closer to having a portable quantum light source using diode lasers.

TOWARDS LOW-FREQUENCY SQUEEZED LIGHT AND ITS APPLICATIONS WITH FOUR-WAVE MIXING IN RUBIDIUM VAPOR

by

Meng-Chang Wu

Dissertation submitted to the Faculty of the Graduate School of the
University of Maryland, College Park in partial fulfillment
of the requirements for the degree of
Doctor of Philosophy
2020

Advisory Committee:
Dr. Paul D. Lett, Co-Chair/Off-Campus Advisor
Dr. Steven L. Rolston, Co-Chair/Campus Advisor
Dr. Mohammad Hafezi
Dr. Alan L. Migdall
Dr. William D. Phillips

Preface

The theory of quantum optics was developed in the early 1960s. With the foundations of Roy Glauber's work [1] researchers have developed a better understanding of the quantum states of light and developed the theory of non-classical light and squeezed light produced with nonlinear optics. In our experiments we generate squeezed light from a four-wave mixing process in hot Rb vapor. In this thesis, we study the noise properties of the squeezed light generated in a diode laser system and a Ti:sapphire laser system.

The first part of the thesis is devoted to building the theory of squeezed states and its application in photodiode calibrations. We construct the squeezed states from Fock states and coherent states with the displacement operator and the squeezing operator (**Chapter 1**). Based on squeezed states we develop a gain-independent calibration scheme for absolute photodiode calibration (**Chapter 2**). We demonstrate several schemes for measuring loss of optical elements and atoms.

The second part of the thesis studies the noise sources that need to be removed to use squeezed light in applications. We show in **Chapter 3** that the low frequency classical noise in the squeezed light can be significantly cancelled out using a dual-seeding technique. This dual-seeding technique, however, can introduce new complications that involve coupling between the two seeding beams which is discussed in **Chapter 4**. We find that this issue can be avoided by seeding with beams that do not intersect in the gain medium. Using this configuration and by mapping the image plane, rather than the Fourier plane, into the four-wave mixing

gain region we can prevent cross talk between pixels of an image. Finally, to produce a portable and cost-effective source of quantum light with semiconductor-based lasers we need to conquer the phase noise of the diode laser and the feedback noise from the tapered amplifier. In **Chapter 5** we study the mechanisms that introduce excess noise into the squeezed light. The mechanisms are not well understood yet, but we at least point out a possible source of this noise.

To

my mother and my father

and to the memory of

Dr. Wei-Chih Liu

Acknowledgments

To begin, I would like to thank my advisor, Paul Lett. He has plenty of innovative projects and clear directions for the research, but still leaves space for our creativity. I feel very fortunate to be in his group. To me the mission of a PhD student is to find out the problem and to solve the problem. Paul insists that we have to know why the problem is being solved. In the end, knowing why we solved the problem helps us to improve the result significantly. The term "philosophy" in the Doctor of Philosophy means the "love of wisdom" from its original Greek meaning. I have learned "philosophy" in its true essence; Paul has taught us that we are not just engineers who solve problems, but we are also lovers of the knowledge behind the solution. One of my impressions of Paul is how he keeps a well-balanced life between research and his personal life. I will keep in mind that doing research with enjoyment in life helps me to maintain my passion and patience for it. At different stages of my PhD journey I have faced different challenges and difficulties, and I am grateful to Paul for his timely help and invaluable advice.

In this PhD program I want to thank Wei-Chih Liu, Michael Coplan, and Charles Clark. Wei-Chih is my advisor for undergraduate research and master's degree. He is also Charles' first PhD student. I learned a lot from him. In addition to doing research, he also shared his PhD life with me and gave me some advice for around eight years before he got a heart attack. He always reminded me of an anonymous quote that says, "If you don't understand a problem, there must be a simpler one you don't understand either." This quote helps me to solve a problem

step by step every time when I encounter a difficult problem. Dr. Coplan was our program director for about twenty-six years. He always calls me Mr. Wu, so I call him Dr. Coplan everywhere. One of my impressions of Dr. Coplan is that he visited a depressed PhD student every day in the hospital. I'm not surprised to hear about this story from my friend since Dr. Coplan always asked me my progress about research when we met. Before I joined Paul's group, Dr. Coplan asked me about my progress in finding a research group frequently and wrote down a list of groups and PhD students for me to contact. He cares about all students like his grandchildren. Dr. Coplan and Charles hold a Kamp Kwal-i-Fire every year to help all PhD students in our program to pass the qualify exams. I thank them for the extra effort for each of us.

I feel very fortunate to have worked and shared conversations in group meetings and lunches with all visiting professors, postdocs, and graduate students in Paul's group. Thank you to Kevin Jones, Quentin Glorieux, Jeremy Clark, Ryan Glasser, Tian Li, Travis Horrom, Brielle Anderson, Prasoon Gupta, Don Fahey, Carla Andrea Hermann Avigliano, Bonnie Schmittberger, Zachary Glassman, Jamie Luskin, Madison Anderson, Nicholas Brewer, Rory Speirs, Xihua Yang, Zhifan Zhou, and Jie Zhao. Each of you has your own manner to go about research and attitude in life. It has been great for me to learn a little from each of you. My later years in the lab I spent more time with Nick. It was a great pleasure working with Nick. Even though sometimes we had opposing opinions about the experiment, eventually we still had a compromised solution to solve the problem successfully. I have really enjoyed working with Nick. We talked a lot about politics, economy, racial issues, and

pets. I didn't feel alone when I did the experiment with Nick. Even though Nick left a little bit earlier, I still have full access to him for consultation. Thank you, Nick. Also, I would like to thank Kevin for the amazing ideas for the experiments. His hearty laughter always made our discussions very relaxed. He is also very generous to provide all the information and advice he has had from his experience.

In addition, I've been lucky to be in the laser cooling and trapping group and the community of the Joint Quantum Institute. I've had the fortunate opportunity to interact with a number of PIs, postdocs, and graduate students: Bill Phillips, Trey Porto, Ian Spielman, Gretchen Campbell, Alan Migdall, Elizabeth Goldschmidt, Alessandro Restelli, Roger Brown, Avinash Kumar, Dina Genkina, Francisco Salces-Cárcoba, Ana Valdés-Curiel, Seiji Sugawa, Hsin-I Lu, Swarnav Banik, Kumel Kagalwala, Haoquan Fan, Donny Pearson, Aditya Sharma, and Martin Ritter. Any short conversations and discussions with you all inspired me a lot. I treasured all the time we stayed together in the seminars, group meetings, and holiday parties. I would like to thank Bill for the endless chocolate. It's also a great time to have a quick discussion with Bill. I enjoy his question time in seminars and group meetings. This helps us to understand the presentation in a different way. I especially want to thank Alan for lending us the equipment and an auspicious lab space after we moved from NIST to the UMD campus. Most of the results in this thesis were finished in this lab space. I admire Alan's passion for making many devices by himself. It was a great pleasure having conversation with Elizabeth during lunch time after our weekly group meetings. This gave me a chance to learn more about other research-related topics in quantum optics. She is also very generous to

give me feedback from her vast knowledge. I also would like to thank her time for mentoring me in the process of reviewing a paper. It was a great privilege to have worked with Alessandro. He is a kind and generous person. In fact, he can even stay with you to troubleshoot electronic issues till 9 pm on Friday night. Finally, I want to thank Dina for the "Dina Shuttle" between Gaithersburg and College Park. I was shy to ask help from people, but her invitation to give me a ride on the "Dina Shuttle" made my daily journey to NIST much easier.

During my PhD student life in Maryland and in the U.S., I have had an amazing support in a variety of aspects from my friends: Li Piin Sung, YongSing You, Isabelle Chianyi Ang, I-Lin Liu, Jim Cheng, Clare Cheng, Yi-Hsieh Wang, Hongcheng Xu, and the saints from the Church in Gaithersburg and the Church in Beltsville. Thank you all for staying with me through this journey to share my excitement in research, and the tough times in different aspects of life. I really have a lot to say here, but words alone cannot capture my gratitude for our memories. In short, all of your company is the best blessings from God.

I should also thank Debbie Jenkins, Pauline Rirksopa, Lorraine Desalvo, Melissa Britton, Paulina Alejandro, Souad Nejjar, Kimberly Emswiler, Gail Griffin-Ferris, and Susan Martin. As an international student here in the U.S., I have had to go through extra procedures for almost everything. However, things are less complicated with all of your help, patience, and smiles.

Finally, I am grateful to my parents for their support so that I can continue to enjoy doing research with full freedom. Even though there are a lot of things that have changed at home for the past few years, knowing you all are still well in

Taiwan through the video chats is another kind of encouragement to me.

Although I am not good at expressing my feelings to people in words or language, I deeply thank all of your company, selfless help, and enlightening advice from my heart. It has been a long journey going through the PhD life. It is my honor to have you all together at different stages of my PhD journey. This thesis is a systematic note of my research in my PhD life. I am fortunate that I have had so many wonderful people, aforementioned or acknowledged in my heart, around me to complete this note. For what shall a PhD profit in life if he/she gains the knowledge, but forfeits his/her enjoyment of doing research? It might not be easy to keep a well-balanced life between the research and enjoyment since there are always some challenges in the experiment. However, with all of your support, I'm glad that I still have my full passion to share my PhD experience and research results with people who are still hesitating about whether to jump into PhD study.

Table of Contents

List of Figures

Chapter 1: Coherent States and Squeezed States

1.1 Introduction

In 1960, the first lasing signal at optical frequencies was observed by Maiman [2] and by the end of the same year several laser systems were realized in different groups. A decade later researchers had better tools to study quantum optics properly after tunable dye lasers were introduced [3, 4]. Among many other things, the development of lasers has given researchers a way to understand atomic states through spectroscopy.

1.2 Fock State, Vacuum State, and Coherent State

One important property of the laser is coherence. A laser generates a coherent light field with well-defined amplitude and phase. In 1963, Glauber [1] described the laser output as a coherent state with the symbol $|\alpha\rangle$. The coherent states can be expressed in terms of superpositions of photon number states or Fock states $|n\rangle$

$$|\alpha\rangle = e^{-\frac{1}{2}|\alpha|^2} \sum_{n=0}^{\infty} \frac{\alpha^n}{\sqrt{n!}} |n\rangle, \tag{1.1}$$

where α is the eigenvalue of the mode annihilation operator $\hat{a}$ and n is the photon number counted in a given interval for a mode of the optical field with a given frequency, propagation vector, and polarization. The probability distribution of sampling the CW laser within a time interval will follow the distribution of the coherent state in Eq. 1.1. Now, we introduce two Hermitian quadrature operators $\hat{q}$ and $\hat{p}$ to replace the non-Hermitian quantum field $\hat{a}$

$$\hat{q} = \sqrt{\frac{\hbar}{2\omega}}(\hat{a}^\dagger + \hat{a}), \tag{1.2}$$

$$\hat{p} = i\sqrt{\frac{\hbar\omega}{2}}(\hat{a}^\dagger - \hat{a}). \tag{1.3}$$

Here, q is the analogue of the position coordinate of a mode oscillator and p represents its momentum. Their corresponding expectation values in the coherent states $|\alpha\rangle$ are

$$\langle\alpha|\hat{q}|\alpha\rangle = \sqrt{\frac{2\hbar}{\omega}}\mathrm{Re}(\alpha), \tag{1.4}$$

$$\langle\alpha|\hat{p}|\alpha\rangle = \sqrt{2\hbar\omega}\mathrm{Im}(\alpha). \tag{1.5}$$

Furthermore, the Heisenberg uncertainty principle tells us the product of the variance of q and p is

$$\langle(\Delta\hat{q})^2\rangle\langle(\Delta\hat{p})^2\rangle \geq \frac{\hbar^2}{4}, \tag{1.6}$$

where $\langle(\Delta\hat{q})^2\rangle$ and $\langle(\Delta\hat{p})^2\rangle$ are fluctuations in observables $\hat{q}$ and $\hat{p}$ for the same state $|\psi\rangle$. We call $|\psi\rangle$ a minimum-uncertainty state when the equality sign in Eq. 1.6 holds. An example of a minimum-uncertainty state is the vacuum state, which is

when $n = 0$. The single-mode radiation field in the ground state, vacuum state $|0\rangle$, satisfies the minimum-uncertainty condition for the observables $\hat{q}$ and $\hat{p}$.

$$\langle 0|(\Delta\hat{q})^2|0\rangle\langle 0|(\Delta\hat{p})^2|0\rangle = \frac{\hbar^2}{4}, \tag{1.7}$$

However, the single-mode number state is a minimum-uncertainty state only for the ground state.

The quantum harmonic oscillator is an analog of the single-mode radiation field. Specifically, the ground state of the quantum harmonic oscillator is a coherent state with α equal zero. We can write down the wave function of the ground state harmonic oscillator as [5]

$$\begin{aligned} \phi_0(q) &= \langle q|0\rangle \\ &= (\frac{\omega}{\pi\hbar})^{1/4}\exp(-\frac{\omega q^2}{2\hbar}). \end{aligned} \tag{1.8}$$

The wave packet variance will remain the same even if displaced by an amount q_α. Immediately after such displacement, the wave function is

$$\phi_\alpha(q) = (\frac{\omega}{\pi\hbar})^{1/4}\exp[-\frac{\omega(q-q_\alpha)^2}{2\hbar}]. \tag{1.9}$$

We can express Eq. 1.9 by the following power series

$$\begin{aligned} \phi_\alpha(q) &= e^{-\frac{1}{2}|\alpha|^2}\sum_{n=0}^{\infty}\frac{\alpha^n}{\sqrt{n!}}\langle q|n\rangle \\ &= \langle q|\alpha\rangle, \end{aligned} \tag{1.10}$$

where $\alpha = (\omega/2\hbar)^{1/2} q_\alpha$. The wave packet in Eq. 1.9 shows the coherent state in Eq. 1.10 is, at any instant in time, also a minimum-uncertainty state, like the wave packet of a vacuum state. In other words, the variance Δq, or fluctuations in observable $\hat{q}$, of coherent states will remain the same as the variance of the vacuum state.

Now, we have a clear picture to explain how a coherent state is a "displaced" vacuum state. The wave function of coherent states can be simply derived from the vacuum state wave function using the displacement operator $\hat{D}(\alpha)$. We can rewrite the coherent states, Eq. 1.1, as

$$|\alpha\rangle = \hat{D}(\alpha)|0\rangle, \tag{1.11}$$

where

$$\hat{D}(\alpha) = e^{\alpha\hat{a}^\dagger - \alpha^*\hat{a}}. \tag{1.12}$$

The wave packets of both the vacuum state and coherent states illustrate that the noise properties of these two states should be the same. Besides the variance of the coordinate quadrature, there is another orthogonal quadrature, the momentum quadrature. We can derive the wave packet for the momentum eigenstate and get the same result, the minimum variance in the momentum wave function. Let's test the Heisenberg uncertainty principle for the coherent states from the expectation

values. The variances of observables $\hat{q}$ and $\hat{p}$ in coherent states are

$$\begin{aligned}\langle\alpha|(\Delta\hat{q})^2|\alpha\rangle &= \langle\alpha|\hat{q}^2|\alpha\rangle - (\langle\alpha|\hat{q}|\alpha\rangle)^2 \\ &= \frac{\hbar}{2\omega},\end{aligned} \tag{1.13}$$

$$\begin{aligned}\langle\alpha|(\Delta\hat{p})^2|\alpha\rangle &= \langle\alpha|\hat{p}^2|\alpha\rangle - (\langle\alpha|\hat{p}|\alpha\rangle)^2 \\ &= \frac{\hbar\omega}{2}.\end{aligned} \tag{1.14}$$

The matrix elements are calculated in rotating frame. We find that both vacuum state and coherent states are minimum-uncertainty states since they satisfy Eq. 1.7.

1.3 From Coherent to Squeezed Light

The vacuum state and coherent states have the same noise properties for each quadrature. From Eq. 1.9 the wave packet in each quadrature of the coherent states does not spread in time even if we have a time dependent displacement on the vacuum state. Also, the fluctuations in either quadrature will not change with the amplitude of the coherent state. These properties make coherent states a good reference for introducing the squeezed state. From the Heisenberg uncertainty relation we can have one quadrature of the minimum-uncertainty state with noise lower than the vacuum noise as long as the noise in the other quadrature is expanded. This is the general idea of squeezed states. We will discuss some properties of the squeezed state in this section. A squeezed state still follows the Heisenberg uncertainty principle although the variance of one of its quadratures is smaller than that of a coherent

state. In 1970, Stoler [6] introduced the squeezing operator

$$\hat{S}_1(z) = exp[\frac{1}{2}(z\hat{a}^{\dagger 2} - z^*\hat{a}^2)], \tag{1.15}$$

where

$$z = re^{i\phi}, \quad 0 \leq r < \infty, \quad 0 \leq \phi \leq 2\pi. \tag{1.16}$$

Single-mode squeezed coherent states can be generated with the squeezing operator from a coherent state

$$|\alpha, z\rangle = \hat{S}_1(z)|\alpha\rangle. \tag{1.17}$$

Note that the squeezing and displacement operators do not commute and their order matters. The following are expectation values of annihilation and creation operators that can be used to derive the variances of quadratures of squeezed coherent states

$$\langle\alpha, z|\hat{a}|\alpha, z\rangle = \alpha \cosh r - \alpha^* e^{i\phi}\sinh r, \tag{1.18}$$

$$\langle\alpha, z|\hat{a}^\dagger|\alpha, z\rangle = \alpha^* \cosh r - \alpha\, e^{-i\phi}\sinh r, \tag{1.19}$$

$$\begin{aligned}\langle\alpha, z|\hat{a}^2|\alpha, z\rangle &= \alpha^2\cosh^2 r - (2|\alpha|^2 + 1)e^{i\phi}\cosh r \sinh r + \alpha^{*2}e^{2i\phi}\sinh^2 r \\ &= (\langle\alpha, z|\hat{a}|\alpha, z\rangle)^2 - e^{i\phi}\cosh r \sinh r,\end{aligned} \tag{1.20}$$

$$\begin{aligned}\langle\alpha, z|\hat{a}\hat{a}^\dagger|\alpha, z\rangle &= (|\alpha|^2 + 1)\cosh^2 r - (\alpha^2 e^{-i\phi} + \alpha^{*2}e^{i\phi})\cosh r \sinh r + |\alpha|^2\sinh^2 r \\ &= \langle\alpha, z|\hat{a}|\alpha, z\rangle\langle\alpha, z|\hat{a}^\dagger|\alpha, z\rangle + \cosh^2 r,\end{aligned} \tag{1.21}$$

$$\begin{aligned}\langle\alpha,z|\hat{a}^{\dagger 2}|\alpha,z\rangle &= \alpha^{*2}\cosh^2 r-(2|\alpha|^2+1)e^{-i\phi}\cosh r\,\sinh r+\alpha^2 e^{-2i\phi}\sinh^2 r\\ &= (\langle\alpha,z|\hat{a}^{\dagger}|\alpha,z\rangle)^2-e^{-i\phi}\cosh r\,\sinh r.\end{aligned} \tag{1.22}$$

Before we derive the variances in a squeezed coherent state, we may define rotated observables $q_{\phi/2}$ and $p_{\phi/2}$ with a rotation by an angle $\phi/2$, where ϕ is between 0 and 2π [5]. The new rotated observables are

$$\hat{q}_{\phi/2}=\sqrt{\frac{\hbar}{2\omega}}(\hat{a}^{\dagger}e^{i\phi/2}+\hat{a}e^{-i\phi/2}), \tag{1.23}$$

$$\hat{p}_{\phi/2}=i\sqrt{\frac{\hbar\omega}{2}}(\hat{a}^{\dagger}e^{i\phi/2}-\hat{a}e^{-i\phi/2}). \tag{1.24}$$

The variances of observables $\hat{q}_{\phi/2}$ and $\hat{p}_{\phi/2}$ in a squeezed coherent state are

$$\begin{aligned}\langle\alpha,z|(\Delta\hat{q}_{\phi/2})^2|\alpha,z\rangle &= \langle\alpha,z|\hat{q}^2_{\phi/2}|\alpha,z\rangle-(\langle\alpha,z|\hat{q}_{\phi/2}|\alpha,z\rangle)^2\\ &= \frac{\hbar}{2\omega}[\langle\alpha,z|(\hat{a}^{\dagger 2}e^{i\phi}+\hat{a}^2e^{-i\phi}+2\hat{a}^{\dagger}\hat{a}+1)|\alpha,z\rangle\\ &\quad -(\langle\alpha,z|\hat{a}^{\dagger}e^{i\phi/2}+\hat{a}e^{-i\phi/2}|\alpha,z\rangle)^2]\\ &= \frac{\hbar}{2\omega}e^{-2r},\end{aligned} \tag{1.25}$$

$$\begin{aligned}\langle\alpha,z|(\Delta\hat{p}_{\phi/2})^2|\alpha,z\rangle &= \langle\alpha,z|\hat{p}^2_{\phi/2}|\alpha,z\rangle-(\langle\alpha,z|\hat{p}_{\phi/2}|\alpha,z\rangle)^2\\ &= \frac{\hbar\omega}{2}[\langle\alpha,z|-(\hat{a}^{\dagger 2}e^{i\phi}+\hat{a}^2e^{-i\phi}-2\hat{a}^{\dagger}\hat{a}-1)|\alpha,z\rangle\\ &\quad +(\langle\alpha,z|\hat{a}^{\dagger}e^{i\phi/2}-\hat{a}e^{-i\phi/2}|\alpha,z\rangle)^2]\\ &= \frac{\hbar\omega}{2}e^{2r}.\end{aligned} \tag{1.26}$$

From Eqs. 1.25 and 1.26 we can easily show the squeezed coherent state is also a minimum-uncertainty state. The parameter r in Eq. 1.16 is called the squeezing

parameter which determines the degree of squeezing. Without the rotation on the observables q and p, we can still write down the generalized expression for their quadrature variance [7]. However, one quadrature can be squeezed while the other is larger than it would need to be for a symmetric minimum uncertainty state. Nonetheless, for our ultimate goal, we only care about the squeezing in one of the quadratures to improve the measurement for phase or amplitude of the field.

1.4 Two-mode Squeezed Light and Four-wave Mixing

From Eqs. 1.15 and 1.17 in preparing the squeezed coherent state we can start with a coherent state light source at the standard quantum limit and compress the noise in one quadrature using a nonlinear two-photon process ($\hat{a}^{\dagger 2}$ and $\hat{a}^2$). The coupling strength, the squeezing parameter r, of the nonlinear process will determine the degree of quadrature squeezing. The squeezing can also be generated from multi-mode coherent states [8, 9] with the product of creation and annihilation operators on the correlated modes, for example two-mode squeezed state [10]. A two-mode squeezed state is a quantum entanglement between two modes of the field. The two modes can, for example, be two different frequencies, two different polarizations, two different states of orbital angular momentum, or different k-vectors. The squeezed quantum fluctuations only exist in the joint properties of the two modes.

Now, we define the two-mode squeezed vacuum state by applying the two-mode squeezing operator $\hat{S}_2(z)$ on the two-mode vacuum $|0\rangle_a|0\rangle_b$. Here we add a

subscript 2 to $|z\rangle$ for the notation of the two-mode squeezed vacuum state

$$|z\rangle_2 = \hat{S}_2(z)|0\rangle_a|0\rangle_b. \tag{1.27}$$

The two-mode squeezing operator $\hat{S}_2(z)$ is a two-photon process from annihilation and creation operators of two different modes that commute

$$\hat{S}_2(z) = exp(z\hat{a}^\dagger\hat{b}^\dagger - z^*\hat{a}\hat{b}). \tag{1.28}$$

Since the squeezing only exists in the superposition of the two modes, we define the superposition quadrature operators as [7]

$$\hat{q}_2 = \sqrt{\frac{\hbar}{4\omega}}(\hat{a}^\dagger + \hat{a} + \hat{b}^\dagger + \hat{b}). \tag{1.29}$$

$$\hat{p}_2 = i\sqrt{\frac{\hbar\omega}{4}}(\hat{a}^\dagger - \hat{a} + \hat{b}^\dagger - \hat{b}). \tag{1.30}$$

For convenience of calculation we use the two-mode Bogoliubov transformation or the Baker-Hausdorf lemma to obtain [5]

$$\hat{S}_2^\dagger\ \hat{a}^\dagger\hat{S}_2 = \hat{a}^\dagger\cosh\, r - \hat{b}\ e^{-i\phi}\sinh\, r, \tag{1.31}$$

$$\hat{S}_2^\dagger\ \hat{a}\ \hat{S}_2 = \hat{a}\ \cosh\, r - \hat{b}^\dagger e^{i\phi}\sinh\, r, \tag{1.32}$$

$$\hat{S}_2^\dagger\ \hat{b}^\dagger\hat{S}_2 = \hat{b}^\dagger\cosh\, r - \hat{a}\ e^{-i\phi}\sinh\, r, \tag{1.33}$$

$$\hat{S}_2^\dagger\ \hat{b}\ \hat{S}_2 = \hat{b}\cosh r - \hat{a}^\dagger e^{i\phi}\sinh r. \tag{1.34}$$

We can derive the variance of the two quadratures easily with these transformations

$$\begin{aligned} {}_2\langle z|(\Delta\hat{q}_2)^2|z\rangle_2 &= {}_2\langle z|\hat{q}_2^2|z\rangle_2 \\ &= \frac{\hbar}{2\omega}(\cosh^2 r + \sinh^2 r - 2\sinh r\cosh r\cos\phi), \end{aligned} \tag{1.35}$$

$$\begin{aligned} {}_2\langle z|(\Delta\hat{p}_2)^2|z\rangle_2 &= {}_2\langle z|\hat{p}_2^2|z\rangle_2 \\ &= \frac{\hbar\omega}{2}(\cosh^2 r + \sinh^2 r + 2\sinh r\cosh r\cos\phi). \end{aligned} \tag{1.36}$$

We find that the two-mode squeezed vacuum state has squeezing in q_2 or p_2 quadratures when $\phi = 0$ or π in Eqs. 1.35 and 1.36.

$$\begin{aligned} {}_2\langle z|(\Delta\hat{q}_2)^2|z\rangle_2 &= \frac{\hbar}{2\omega}e^{-2r} \qquad (for \quad \phi = 0), \\ &= \frac{\hbar}{2\omega}e^{2r} \qquad (for \quad \phi = \pi), \end{aligned} \tag{1.37}$$

$$\begin{aligned} {}_2\langle z|(\Delta\hat{p}_2)^2|z\rangle_2 &= \frac{\hbar\omega}{2}e^{2r} \qquad (for \quad \phi = 0), \\ &= \frac{\hbar\omega}{2}e^{-2r} \qquad (for \quad \phi = \pi). \end{aligned} \tag{1.38}$$

Both of the squeezed quadratures are in minimum-uncertainty states. The two-mode squeezed vacuum state, Eq. 1.27, can also be expressed in terms of the number states [7]

$$|z\rangle_2 = \frac{1}{\cosh r}\sum_{n=0}^{\infty}(-1)^n e^{in\phi}(\tanh r)^n |n\rangle_a|n\rangle_b. \tag{1.39}$$

It shows the two-mode squeezing only occurs in the paired states $|n\rangle_a|n\rangle_b$. Therefore, we also call the two-mode squeezed light "twin beams". Two-mode

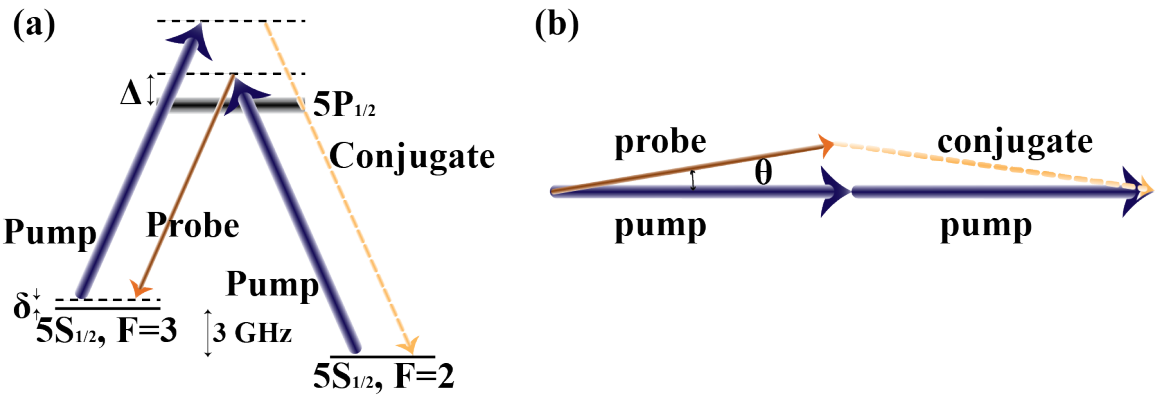

Figure 1.1: (a) Energy level diagram for the non-degenerate 4WM process in ^{85}Rb. The optical wavelength is $\lambda = 795$ nm. The broadened upper level indicates the Doppler broadening of the transition. Typical detunings are $\Delta = 1.3$ GHz and $\delta = 2$ MHz. (b) The geometric phase-matching condition for the 4WM. We show the k-vectors of the pump twice, the probe and conjugate beams. The refractive index of Rb vapor is different for the probe beam and the conjugate beam. To satisfy the phase-matching condition, the probe and conjugate beams have a small angle $\theta \approx 0.4°$ with the pump beam.

squeezed light can be generated from the four-wave mixing (4WM) process in three-level systems [11–14]. The polarization in a medium is described as

$$P_i = \epsilon_0 \chi^{(1)}_{i,j} E_j + \epsilon_0 \chi^{(2)}_{i,j,k} E_j E_k + \epsilon_0 \chi^{(3)}_{i,j,k,l} E_j E_k E_l + ..., \tag{1.40}$$

where $\chi^{(n)}$ is a $(n+1)$th rank tensor and the nth-order susceptibility. In the 4WM process we generate twin beams, the amplified probe beam ($E_{\rm p}$) and the conjugate beam ($E_{\rm c}$), from a strong pump beam ($E_{\rm pump}$) and a weak probe seed beam interacting in a hot rubidium vapor. The twin beams and the pump beam form a double-Λ system, shown in Fig. 1.1 (a). Based on energy conservation, two pump photons are converted into a correlated probe and conjugate photon pair when the phase matching angle, illustrated in Fig. 1.1 (b), is satisfied. The energy conservation and phase matching conditions

$$2\omega_{\rm pump} = \omega_{\rm p} + \omega_{\rm c}, \tag{1.41}$$

$$2\mathbf{k}_{\rm pump} = \mathbf{k}_{\rm p} + \mathbf{k}_{\rm c}, \tag{1.42}$$

where $\omega_{\rm pump}$, $\mathbf{k}_{\rm pump}$, $\omega_{\rm p}$, $\mathbf{k}_{\rm p}$, $\omega_{\rm c}$, and $\mathbf{k}_{\rm c}$ are frequencies and wave vectors of the pump, probe, and conjugate beams. Here, k is equal to $n\omega/c$ and $n(\omega)$ is a dispersive index of refraction. The interaction Hamiltonian can be expressed as

$$\hat{H}_{\rm I} = i\hbar(\zeta \psi^2_{\rm pump} \hat{p}^\dagger \hat{c}^\dagger - \zeta^* \psi^{*2}_{\rm pump} \hat{p}\hat{c}), \tag{1.43}$$

where $\hat{p}^\dagger$, $\hat{c}^\dagger$, $\hat{p}$, and $\hat{c}$ are creation and annihilation operators of the probe and conju-

gate fields and ζ is the interaction strength from the $\chi^{(3)}$ nonlinear polarization. We treat the undepleted pump field, ψ_{pump}, classically in the interaction Hamiltonian. The evolution operator can be written in the form

$$\hat{U} = e^{-\frac{i}{\hbar}\hat{H}_{\text{I}}t}, \tag{1.44}$$

which, when $\hat{H}_{\text{I}}$ is expressed in terms of creation and annihilation operators, is similar to the form of the two-mode squeezing operator, Eq. 1.28. Now we see that the 4WM is a nonlinear process that can generate two-mode squeezed light.

1.5 Noise Measurements

In our laboratory, we usually generate 4WM with a Ti:sapphire laser [15]. To make a portable and cost-effective quantum light source in this thesis we try to set up the experiment using a semiconductor-based laser system. For the experimental setup discussed in this thesis, we use a tapered amplifier (TA) to amplify the laser power from a diode laser. The laser frequency output from the TA should follow the diode laser perfectly so that the linewidth of the output of the TA can be determined by locking the diode laser. Most of the TA power (typically 700-800 mW) near the rubidium 85 D_1 line will go to the rubidium cell as the pump beam for the four-wave mixing. To generate the probe beam, we down-shift a portion of the light from the diode laser by 3.034 GHz with a double-passed 1.5 GHz acousto-optic modulator (AOM). The pump and probe beams are overlapped in the 1.25 cm long ^{85}Rb cell with a small angle of 0.4 degrees in order to meet the phase matching conditions of

the four-wave mixing.

In the experiment we measure the laser noise with photodiode detectors. A photodiode has its quantum efficiency η, which is defined as the ratio of the number of photoelectrons generated to the number of incident photons [16]

$$\eta = \frac{i}{e\Phi}, \tag{1.45}$$

where i is the photocurrent, e is the modulus of the electron charge, and Φ is the photon flux. The photon number fluctuations, noise, will appear in the photocurrent fluctuations Δi. The fluctuations can be read in an RF spectrum analyzer as noise power

$$\begin{aligned} P_{\text{noise}} &= (\Delta i)^2 R_{\text{L}}, \\ &= 2e\Delta f \langle i \rangle R_{\text{L}}, \end{aligned} \tag{1.46}$$

where Δf is the detector bandwidth, $\langle i \rangle$ is the average photocurrent, and R_{L} is the load resistor of the detector. The square of the photocurrent variance is obtained by taking the Fourier transform of $i(t)$ and measuring the current fluctuations within a frequency bandwidth Δf.

The red curve in Fig. 1.2 shows the intensity noise spectrum measured with a single photodiode detector and with current going to an RF spectrum analyzer for the Ti:sapphire laser operating at 795 nm. The laser noise reaches the shot-noise limit, or standard quantum limit, at frequencies above 700 kHz. The "shot noise" is a frequency independent and unavoidable intensity noise. The laser contains additional classical noise, which does not increase linearly with the optical power, at

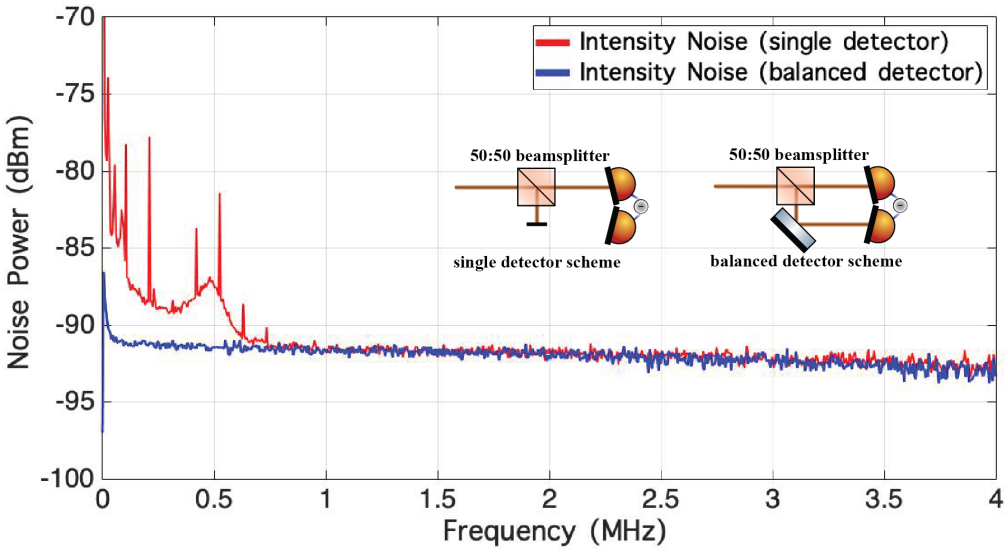

Figure 1.2: Spectra of noise power versus frequency for light from a Ti:sapphire laser, comparing a single detector and balanced detector scheme. The red curve shows the noise measured with a single detector for a power of 80 μW and the blue curve shows the noise measured with a balanced detector for a power of 40 μW on each photodiode. The resolution bandwidth (RBW) is 1 kHz and the video bandwidth (VBW) is 100 Hz for these measurements. Electronic noise is subtracted from these traces. The detector bandwidth is 4 MHz. The intensity noise is not completely flat because it approaches the limit of detector bandwidth.

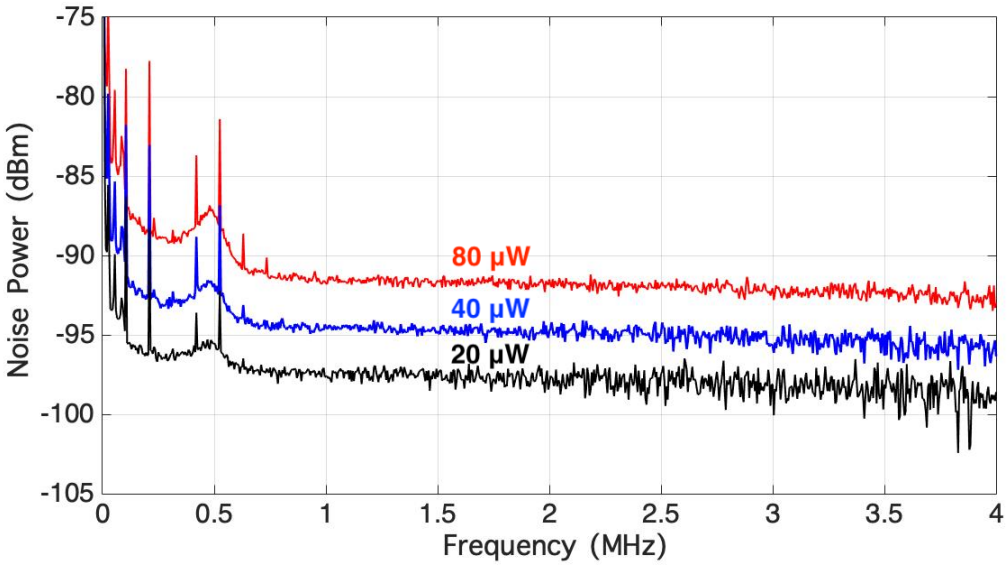

Figure 1.3: The red, blue, and black curves show the intensity noise of light source from a Ti:sapphire laser measured with a single detector for a power of 80 μW, 40 μW, and 20 μW. The resolution bandwidth (RBW) is 1 kHz and the video bandwidth (VBW) is 100 Hz for these measurements. The detector bandwidth is 4 MHz. Electronic noise is subtracted from these traces.

frequencies below 1 MHz, as shot noise does. The classical noise at low frequencies decreases significantly when we attenuate the optical power (Fig. 1.3). We know that the vacuum state is also a coherent state. The noise power at low frequencies will approach the shot noise limit when we attenuate the laser power down to zero because there is no classical noise that can be added to the vacuum state through photons. When we approach lower and lower power, the shot noise becomes the dominant feature.

The classical noise can be removed with the balanced detector scheme, shown in the blue curve of Fig. 1.2. The balanced detector contains two matched pho-

todiodes with similar quantum efficiency. It's a difference amplifier, which can eliminate the common mode fluctuations. To get a clean shot noise measurement at low frequencies the laser beam is split into two beams of equal power with a 50:50 beamsplitter and then detected with a balanced detector. Each beam contains the same amount of classical noise and uncorrelated quantum noise. Only the classical fluctuations are subtracted by the balanced detector. As we shall see in chapter 3 in our 4WM experiment we generate quantum correlated twin beams. We get squeezed noise below shot noise in Fig. 3.2. In our 4WM experiment we generate quantum correlated twin beams, the probe and conjugate beams, and measure the noise difference between the probe and conjugate beams, which is called intensity difference noise. Each beam of the twin beams has its own thermal noise [17] that comes from the 4WM process, and they are correlated to each other. We get squeezed noise below shot noise when the quantum correlated thermal noise is subtracted by the balanced detector. In this thesis we have a similar idea of eliminating classical noise by dual seeding 4WM to improve the intensity difference squeezing at low frequencies.

1.6 Applications

Squeezed light can improve the performance in optical communication systems [18, 19]. Recently, it's been used for the gravitational wave measurement [20, 21]. One important application is to improve the sensitivity of interferometers so that scientists can observe spacetime distorted by massive objects, like black holes

and neutron stars [22]. Many measurements that are limited by the "shot noise limit" of a laser can have further improvements using squeezed light, for example, magnetometry [23, 24]. People can also encode information into squeezed states for quantum computation [25]. With a given maximum optical power, squeezed states allow more information to be encoded.

In our experiment, a correlated twin-beam source can be used for an absolute calibration of analog photodetectors without any standard reference [26–29]. In the 4WM process the photon pairs are created simultaneously at the same angle but in opposite directions on either side of the pump, one photon of a pair can be used as a trigger to tell us that another photon is present in the other beam. These quantum correlated photon pairs can be used for the calibration of photon-counting detectors. However, it requires a low gain for the parametric process to ensure that there is only one photon in a given time interval in each optical mode. On the other hand, with a 4WM-gain-independent calibration scheme [28], we can measure the cross-correlation function and autocorrelation function of the intensities from both detectors to enable the quantum efficiency calibration of analog photodetectors. The cross-correlation function and auto-correlation function correspond to the coincidence rate and the single count rate of the reference detector for the calibration of photon-counting detectors.

The 4WM process without a cavity allows the probe and conjugate beams to have a range of transverse wave vectors with good phase-matching. This gives us a promising way to generate multi-spatial-mode quantum-correlated images and improve the sensitivity in a twin-image subtraction measurement [30]. In our ex-

periment, we try to improve the squeezing at low frequencies so that the detection of quantum-correlated images will not be limited by the low-frequency noise. This should allow the future sub-shot-noise detection of trace absorption signals using imaging detectors, for example, the biological imaging at low light level. In particular, integrating detectors like CCD cameras with shutter time on the order of millisecond look at light over a range of low frequencies. It is the integrated squeezing over this range of frequencies that will determine if lower noise can be achieved.

Chapter 2: Photodiode Calibrations with Squeezed Light

2.1 Introduction

Photodetector calibration is quite important in many fields. We need to calibrate the photodetector so that the detector can give us a correct value of the light signal. For example, patients with severe acute respiratory infection when infected with the coronavirus disease need to monitor their own oxygen saturation with the pulse oximeter. The oximeter contains a photodetector to detect red and infrared light signals that pass through a body part. A calibrated photodetector can provide accurate health information for treatment.

Quantum correlated twin beams from the 4WM process could be used for the calibration of the absolute quantum efficiency of analog photodiodes [27–29,31]. The twin beams (the probe beam and the conjugate beam) are generated in pairs. In the previous chapter we showed that these twin beams display two-mode squeezing. Ideally, each beam has the same photon number that has been generated from the pump beam. In the 4WM process the photon pairs are created simultaneously at the same angle but in opposite directions on either side of the pump, one of the photons can be used as a trigger to tell us there is another photon present in the other beam.

The idea of the absolute calibration for photodetectors has been demonstrated with correlated photons based on the parametric down-conversion process [26,32,33]. The pump photons are converted into correlated photon pairs under the constraints of momentum and energy conservation. Both photons in a pair are generated simultaneously, in directions on either side of the pump. The detection of one photon of the pair provides information about the other photon. In the calibration process two uncalibrated single-photon detectors are prepared to be calibrated. Neither one needs to be a calibrated standard detector. One of the detectors can be treated as the trigger for the other detector. If this trigger detector misses a photodetection due to its own quantum inefficiency, it will not result in a trigger count for the calibration. When it does trigger, the probability that the detector-under-test registers a count is an estimate of the detector efficiency. However, all the losses in the detector-under-test channel need to be measured and included in the calculation of the total quantum efficiency of the detector-under-test. The absolute quantum efficiency can be derived from the total number of coincidence counts, the total number of trigger counts, and the total losses in the entire detection channel.

We use a similar idea to calibrate analog photodiodes. The quantum-correlated twin beams from the 4WM process are generated in continuous waves. We measure the optical power of the twin beams with analog photodiodes instead of registering photon numbers with photon counters. The cross-correlation function between the twin beams is like the "coincidence counts," registering the similarity of the noise fluctuations. The role of the single count rate is taken by the auto-correlation function of the reference beam, the probe beam or the conjugate beam. The total

losses in the optical path will affect the correlation between the twin beams so that we need to separate out the loss in the optical path from the inefficiency of the the detector itself.

2.2 Correlation Functions

Here we calculate correlation functions for the twin beams and express measured correlation functions through the photocurrents with the quantum efficiency of uncalibrated photodetectors. In Eq. 1.43 of the previous chapter we defined the two-mode squeezing operator

$$\hat{S}_2(z) = \exp(z\hat{p}^\dagger\hat{c}^\dagger - z^*\hat{p}\hat{c}), \tag{2.1}$$

and the displacement operator

$$\hat{D}_p(\alpha) = e^{\alpha\hat{p}^\dagger - \alpha^*\hat{p}}. \tag{2.2}$$

Here we add a subscript 2 to the notation of the single-mode squeezed coherent states, $|\alpha, z\rangle$, for the notation of the two-mode squeezed coherent states. The two-mode squeezed coherent states can be generated with the squeezing operator from a coherent state

$$|\alpha, z\rangle_2 = \hat{S}_2(z)\hat{D}_p(\alpha)|0\rangle_p|0\rangle_c. \tag{2.3}$$

We use the Baker-Campbell-Hausdorff theorem to obtain the two-mode squeezed coherent states, Eq. 2.3, in terms of the number states.

$$
\begin{aligned}
|\alpha, z\rangle_2 &= e^{-|\alpha|^2/2} \sum_{n=0}^{\infty} \frac{\alpha^n}{(\cosh\, r)^{n+1}\sqrt{n!}} e^{e^{i\phi}(\tanh\, r)\hat{p}^\dagger \hat{c}^\dagger} |n\rangle_p |0\rangle_c \\
&= e^{-|\alpha|^2/2} \sum_{n=0}^{\infty}\sum_{m=0}^{\infty} \frac{\alpha^n e^{im\phi}(\tanh\, r)^m \sqrt{(m+n)!\; m!}}{(\cosh\, r)^{n+1}\; m!\; n!} |m+n\rangle_p |m\rangle_c
\end{aligned}
\tag{2.4}
$$

For the two-mode squeezed vacuum state it only contains the paired states $|n\rangle_p|n\rangle_c$. The twin-photons are generated pair by pair for the unseeded 4WM process. For the seeded 4WM process the two-mode squeezed coherent states, Eq. 2.4, will become paired states, that are displaced due to a coherent state seed in one of the beams. The amplified probe beam contains the original probe seed beam. We could still use the twin-beams from the seeded 4WM process for the absolute calibration of analog photodiodes. Just keep it in mind that one of the twin-beams contains the probe seed beam.

The expectation values of the amplified probe and conjugate beams are

$$
\begin{aligned}
{}_2\langle \alpha, z|\hat{p}^\dagger \hat{p}|\alpha, z\rangle_2 &= e^{-|\alpha|^2} \sum_{n=0}^{\infty} \frac{|\alpha|^{2n}}{n!}(n\, \cosh^2 r + \sinh^2 r) \\
&= |\alpha|^2 \cosh^2 r + \sinh^2 r,
\end{aligned}
\tag{2.5}
$$

and

$$
\begin{aligned}
{}_2\langle \alpha, z|\hat{c}^\dagger \hat{c}|\alpha, z\rangle_2 &= e^{-|\alpha|^2} \sum_{n=0}^{\infty} \frac{|\alpha|^{2n}(n+1)}{n!} \sinh^2 r \\
&= |\alpha|^2 \sinh^2 r + \sinh^2 r,
\end{aligned}
\tag{2.6}
$$

where $\hat{p}$ and $\hat{c}$ are the field annihilation operators for the probe and conjugate beams.

The difference of the photon number expectation values between the amplified probe beam and the conjugate beam is the expectation of the probe seed beam itself, $|\alpha|^2$. Here we define the optical gain of the probe beam,

$$G = \cosh^2 r. \tag{2.7}$$

The expectation values for the normally ordered operators are given by

$$\begin{aligned} {}_2\langle \alpha, z|\hat{p}^\dagger \hat{p}^\dagger \hat{p}\ \hat{p}|\alpha, z\rangle_2 &= e^{-|\alpha|^2} \sum_{n=0}^{\infty} \left(\frac{|\alpha|^n}{n!(\cosh\, r)^{n+1}}\right)^2 \sum_{m=0}^{\infty} (m+n)(m+n-1)\frac{(m+n)!}{m!}\tanh^{2m} r \\ &= {}_2\langle \alpha, z|\hat{p}^\dagger \hat{p}\ \hat{p}^\dagger \hat{p}|\alpha, z\rangle_2 - {}_2\langle \alpha, z|\hat{p}^\dagger \hat{p}|\alpha, z\rangle_2 \\ &= G^2|\alpha|^4 + 4G(G-1)|\alpha|^2 + 2(G-1)^2, \end{aligned} \tag{2.8}$$

$$\begin{aligned} {}_2\langle \alpha, z|\hat{c}^\dagger \hat{c}^\dagger \hat{c}\ \hat{c}|\alpha, z\rangle_2 &= e^{-|\alpha|^2} \sum_{n=0}^{\infty} \left(\frac{|\alpha|^n}{n!(\cosh\, r)^{n+1}}\right)^2 \sum_{m=0}^{\infty} (m^2-m)\frac{(m+n)!}{m!}\tanh^{2m} r \\ &= {}_2\langle \alpha, z|\hat{c}^\dagger \hat{c}\ \hat{c}^\dagger \hat{c}|\alpha, z\rangle_2 - {}_2\langle \alpha, z|\hat{c}^\dagger \hat{c}|\alpha, z\rangle_2 \\ &= (G-1)^2|\alpha|^4 + 4(G-1)^2|\alpha|^2 + 2(G-1)^2, \end{aligned} \tag{2.9}$$

$$\begin{aligned} {}_2\langle \alpha, z|\hat{p}^\dagger \hat{c}^\dagger \hat{c}\ \hat{p}|\alpha, z\rangle_2 &= e^{-|\alpha|^2} \sum_{n=0}^{\infty} \left(\frac{|\alpha|^n}{n!(\cosh\, r)^{n+1}}\right)^2 \sum_{m=0}^{\infty} (m+n)m\frac{(m+n)!}{m!}\tanh^{2m} r \\ &= G(G-1)\ |\alpha|^4 + (G-1)(4G-1)|\alpha|^2 + (G-1)(2G-1). \end{aligned} \tag{2.10}$$

The measured photocurrents of the amplified probe beam and the conjugate

beam are $\hat{i}_p$ and $\hat{i}_c$. The auto-correlation functions and cross-correlation function of the twin-beams are expressed as

$$\langle \delta\hat{i}_p(t)\delta\hat{i}_p(t+\tau)\rangle = {}_2\langle\alpha, z|\hat{i}_p(t)\hat{i}_p(t+\tau)|\alpha, z\rangle_2 - {}_2\langle\alpha, z|\hat{i}_p(t)\hat{i}_p(t)|\alpha, z\rangle_2, \tag{2.11}$$

$$\langle \delta\hat{i}_c(t)\delta\hat{i}_c(t+\tau)\rangle = {}_2\langle\alpha, z|\hat{i}_c(t)\hat{i}_c(t+\tau)|\alpha, z\rangle_2 - {}_2\langle\alpha, z|\hat{i}_c(t)\hat{i}_c(t)|\alpha, z\rangle_2, \tag{2.12}$$

$$\langle \delta\hat{i}_p(t)\delta\hat{i}_c(t+\tau)\rangle = {}_2\langle\alpha, z|\hat{i}_p(t)\hat{i}_c(t+\tau)|\alpha, z\rangle_2 - {}_2\langle\alpha, z|\hat{i}_p(t)\hat{i}_c(t)|\alpha, z\rangle_2. \tag{2.13}$$

We assume that we obtain the intensity-difference squeezing of the twin-beams from a stationary process and that all the atoms are in a steady state. To simplify the calculation we also assume that the temporal response functions, F(t), of both uncalibrated detectors are equal. Considering the quantum efficiency of the detector in the correlation measurement, the expectation values of the normally ordered field operators are rewritten as [28]

$${}_2\langle\alpha, z|\hat{p}^\dagger\hat{p}|\alpha, z\rangle_2 \to \eta_p\ {}_2\langle\alpha, z|\hat{p}^\dagger\hat{p}|\alpha, z\rangle_2, \tag{2.14}$$

$${}_2\langle\alpha, z|\hat{p}^\dagger\hat{p}^\dagger\hat{p}\ \hat{p}|\alpha, z\rangle_2 \to \eta_p^2\ {}_2\langle\alpha, z|\hat{p}^\dagger\hat{p}^\dagger\hat{p}\ \hat{p}|\alpha, z\rangle_2, \tag{2.15}$$

$${}_2\langle\alpha, z|\hat{c}^\dagger\hat{c}|\alpha, z\rangle_2 \to \eta_c\ {}_2\langle\alpha, z|\hat{c}^\dagger\hat{c}|\alpha, z\rangle_2, \tag{2.16}$$

$${}_2\langle\alpha, z|\hat{c}^\dagger\hat{c}^\dagger\hat{c}\ \hat{c}|\alpha, z\rangle_2 \to \eta_c^2\ {}_2\langle\alpha, z|\hat{c}^\dagger\hat{c}^\dagger\hat{c}\ \hat{c}|\alpha, z\rangle_2, \tag{2.17}$$

$${}_2\langle\alpha, z|\hat{p}^\dagger\hat{c}^\dagger\hat{c}\ \hat{p}|\alpha, z\rangle_2 \to \eta_p\eta_c\ {}_2\langle\alpha, z|\hat{p}^\dagger\hat{c}^\dagger\hat{c}\ \hat{p}|\alpha, z\rangle_2, \tag{2.18}$$

where η_p and η_c are the quantum efficiencies of the photodetectors for the amplified

probe beam and the conjugate beam.

With these assumptions the correlation functions, Eq. 2.11, 2.12, and 2.13, are expressed in terms of the quantum efficiencies of the detectors and the gain of the probe beam.

$$\begin{aligned}\langle \delta\hat{i}_p(t)\delta\hat{i}_p(t+\tau)\rangle &= [\eta_p^2\ {}_2\langle \alpha, z|\hat{p}^\dagger\hat{p}^\dagger\hat{p}\ \hat{p}|\alpha, z\rangle_2 + \eta_p\ {}_2\langle \alpha, z|\hat{p}^\dagger\hat{p}|\alpha, z\rangle_2 \\ &\quad - \eta_p^2({}_2\langle \alpha, z|\hat{p}^\dagger\hat{p}|\alpha, z\rangle_2)^2] \times g_p^2 F(t) \\ &= \{\eta_p^2[2G(G-1)|\alpha|^2 + (G-1)^2] + \eta_p(G|\alpha|^2 + G - 1)\} \times g_p^2 F(t),\end{aligned} \tag{2.19}$$

$$\begin{aligned}\langle \delta\hat{i}_c(t)\delta\hat{i}_c(t+\tau)\rangle &= [\eta_c^2\ {}_2\langle \alpha, z|\hat{c}^\dagger\hat{c}^\dagger\hat{c}\ \hat{c}|\alpha, z\rangle_2 + \eta_c\ {}_2\langle \alpha, z|\hat{c}^\dagger\hat{c}|\alpha, z\rangle_2 \\ &\quad - \eta_c^2({}_2\langle \alpha, z|\hat{c}^\dagger\hat{c}|\alpha, z\rangle_2)^2] \times g_c^2 F(t) \\ &= \{\eta_c^2[2(G-1)^2|\alpha|^2 + (G-1)^2] + \eta_c[(G-1)|\alpha|^2 + G - 1]\} \times g_c^2 F(t),\end{aligned} \tag{2.20}$$

$$\begin{aligned}\langle \delta\hat{i}_p(t)\delta\hat{i}_c(t+\tau)\rangle &= (\eta_p\eta_c\ {}_2\langle \alpha, z|\hat{p}^\dagger\hat{c}^\dagger\hat{c}\ \hat{p}|\alpha, z\rangle_2 - \eta_p\ {}_2\langle \alpha, z|\hat{p}^\dagger\hat{p}|\alpha, z\rangle_2\ \eta_c\ {}_2\langle \alpha, z|\hat{c}^\dagger\hat{c}|\alpha, z\rangle_2) \\ &\quad \times g_p g_c F(t) \\ &= \eta_p\eta_c[2G(G-1)|\alpha|^2 + G(G-1)] \times g_p g_c F(t),\end{aligned} \tag{2.21}$$

where g_p and g_c are the electronic gains of the photodetectors. We define the relative photocurrent correlation functions i_{pp}, i_{cc}, and i_{pc} as

$$i_{pp} = \eta_p G[1 + 2(G-1)\eta_p]g_p^2, \tag{2.22}$$

$$i_{cc} = \eta_c(G-1)[1 + 2(G-1)\eta_c]g_c^2, \tag{2.23}$$

$$i_{pc} = \eta_p \eta_c \times 2G(G-1) g_p g_c. \tag{2.24}$$

For the seeded 4WM process the spontaneous emission part is relatively weaker than the amplified probe seed beam. Therefore, we assume that $|\alpha|^2 \gg 1$ and simplify the ratio between the correlation functions as

$$R_p = \frac{\langle \delta\hat{i}_p(t) \delta\hat{i}_c(t+\tau) \rangle}{\langle \delta\hat{i}_p(t) \delta\hat{i}_p(t+\tau) \rangle} \approx \frac{i_{pc}}{i_{pp}}, \tag{2.25}$$

$$R_c = \frac{\langle \delta\hat{i}_p(t) \delta\hat{i}_c(t+\tau) \rangle}{\langle \delta\hat{i}_c(t) \delta\hat{i}_c(t+\tau) \rangle} \approx \frac{i_{pc}}{i_{cc}}. \tag{2.26}$$

With the electronic gains of the detectors, the gain of the probe beam, and the correlation functions of the twin-beams, we are able to obtain the quantum efficiencies of the photodetectors.

$$\eta_p = \frac{g_p R_p R_c + g_c R_c}{2 g_p [G - (G-1) R_p R_c]}, \tag{2.27}$$

$$\eta_c = \frac{g_c (G-1) R_p R_c + g_p G R_p}{2 g_c (G-1) [G - (G-1) R_p R_c]}. \tag{2.28}$$

2.3 Loss Measurements

The total quantum inefficiencies, $(1-\eta_p)$ and $(1-\eta_c)$, for the detectors of the probe beam and the conjugate beam include the optical losses and detector quantum inefficiencies in each detection channel. In order to get the quantum efficiencies of photodetectors, we have to measure the optical losses of each element after the probe seed beam intersects with the pump beam.

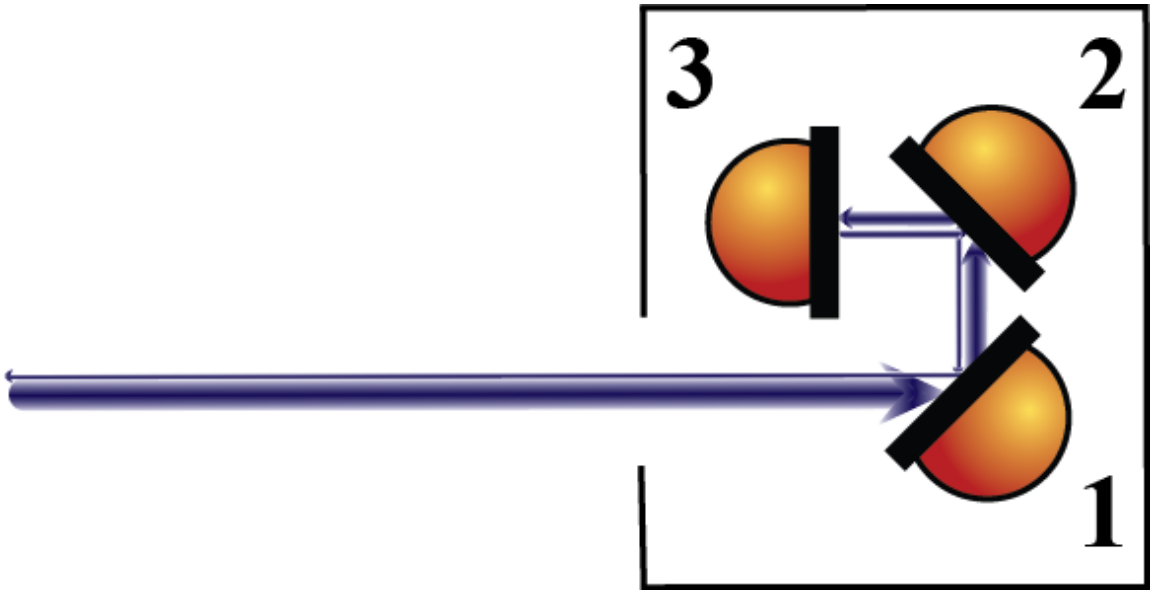

Figure 2.1: Basic arrangement of the trap detector.

The optical loss of each element can be measured by using trap detectors [34]. The trap detector has high quantum efficiency ($> 99\%$), low calibration uncertainty ($< 0.5\%$), and good spatial uniformity ($< 0.05\%$ over 2.5 mm radius) and high linearity for the loss measurement. There are three photodiodes inside the trap detector, shown in Fig. 2.1. The quantum efficiency of each photodiode is low ($\approx 70\%$), but the total quantum efficiency can still be over 99% because four of five reflections from the incident beam are absorbed and measured by the subsequent photodiodes.

The trap detector we use is designed for a collimated beam. In order to measure the transmittance of a lens we can measure the total transmittance of two lenses with the same focal length, as shown in Fig. 2.2, so that the transmitted beam to the trap detector is still collimated. With this method we need at least three lenses

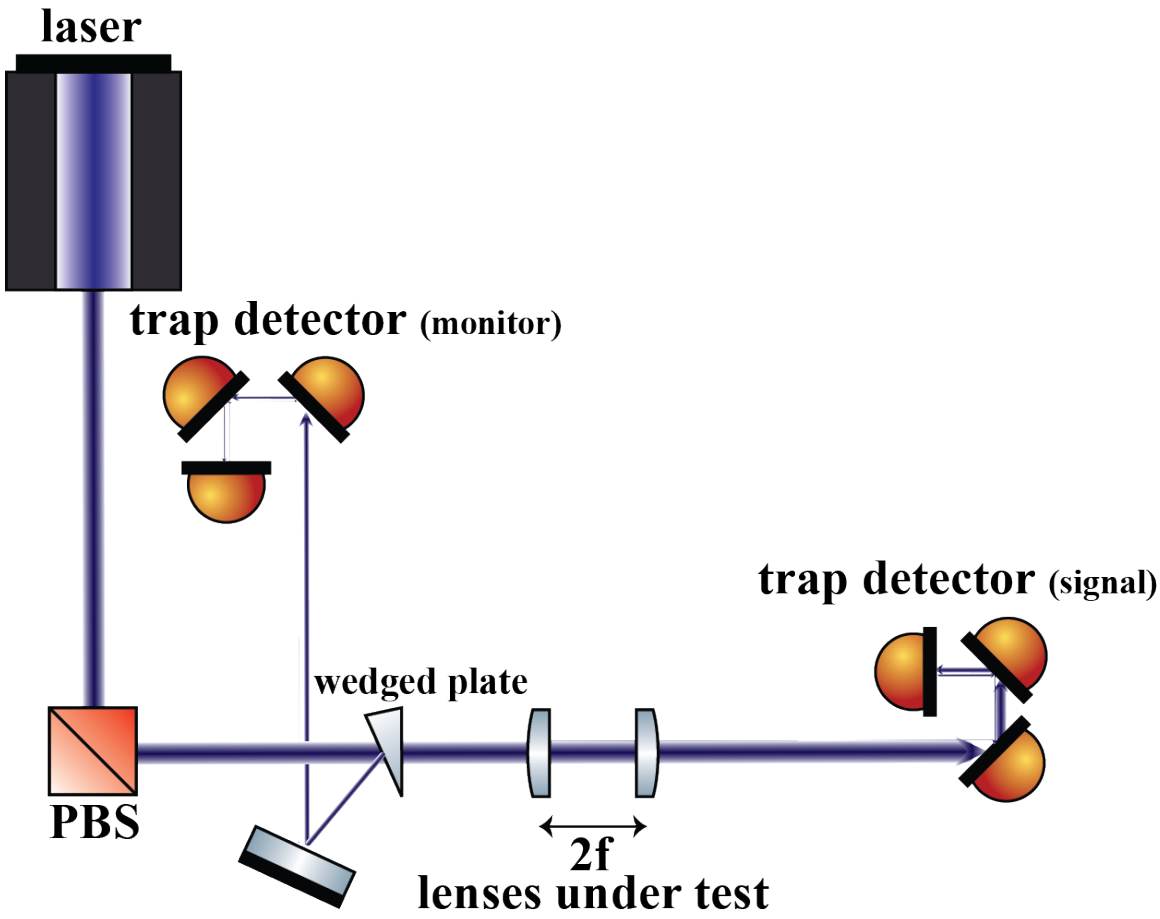

Figure 2.2: Loss measurement of paired lenses. The beamsplitter is a polarizing beamsplitter.

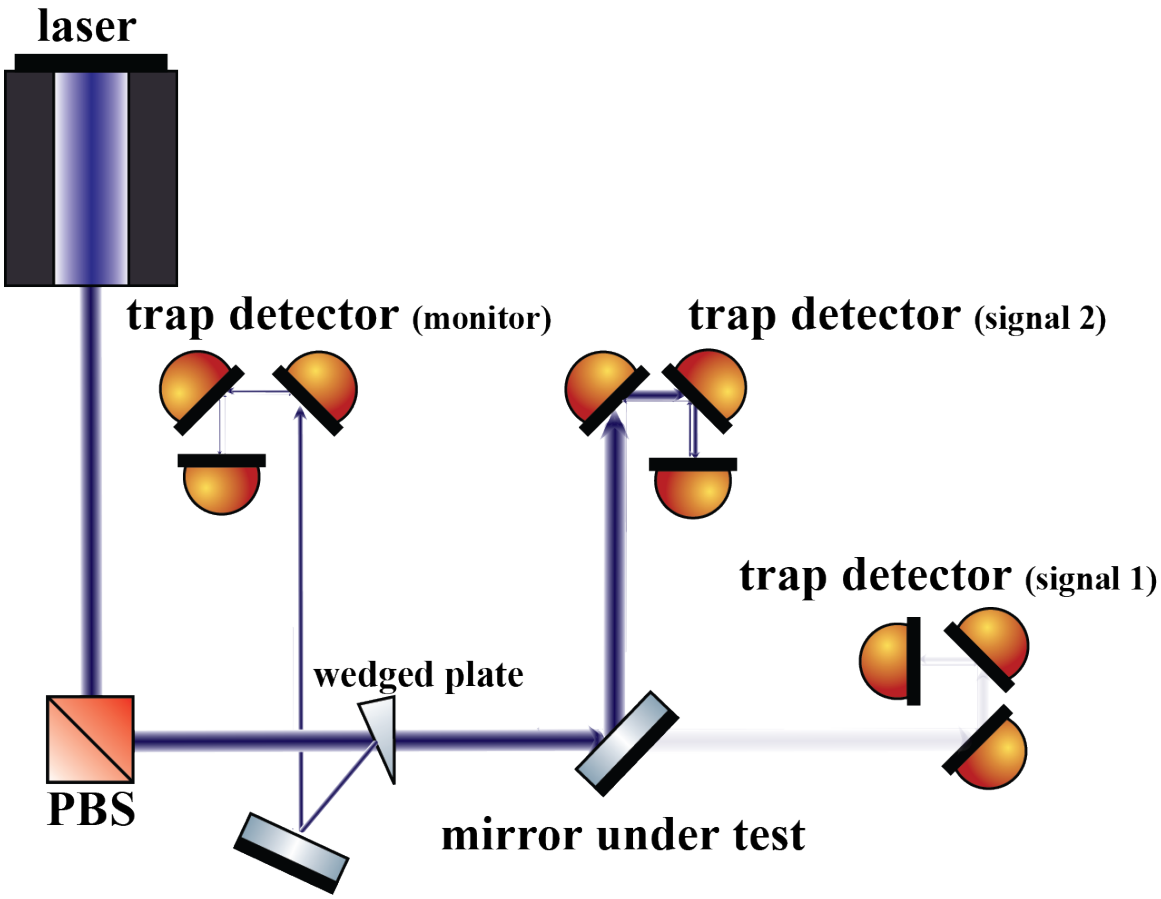

Figure 2.3: Setup for the reflectance measurement. The beamsplitter is a polarizing beamsplitter.

to determine the transmittance of each lens. To get a smaller uncertainty of the transmittance measurement the "overdetermined" approach, which has more than three lenses for the measurement, will improve the accuracy of the measurement [35].

In Fig. 2.2 we send a small amount of the reflected beam from the first interface of the wedged window to the monitor detector as a reference signal. In order to get a good correction signal we need to avoid polarization fluctuations due to the influence of the Brewster's angle reflection. The light source is selected to be an s-polarized

beam with a polarizing beamsplitter since the unpolarized light source after the wedged window will become a partially p-polarized beam. A fully polarized light source makes the ratio of the reflected beam and the transmitted beam after the wedged window stable because the polarization of the transmitted beam will not vary after going through the wedged window. The incident angle on the first surface of the wedged window needs to be very small ($< 0.2°$) to maintain a good correction of the power fluctuations. The reflected beam from the polarizing beamsplitter is not a pure s-polarization. A smaller incident angle at the wedged window reduces any polarization dependent variation of the ratio of the reflected beam to the transmitted beam. At near normal incidence the reflectance of the s-polarized and p-polarized beams are similar and their reflectance variations are less sensitive to the incident angle at small angles.

We have the same setup for the transmittance measurement of the Rb cell and the polarizing beamsplitter. For the transmittance measurement, it is an absolute measurement even without knowing the quantum efficiency of the trap detector, only detector linearity matters. We simply measure the input power with and without the optical elements under test in the beam path. To measure the reflectance of the mirror we need a third trap detector, shown in Fig. 2.3, to measure the input power and the power after the mirror. We still don't need to know the absolute quantum efficiency of the third trap detector to get the absolute reflectance of the mirror. We only need to measure the relative quantum efficiency between two signal detectors with the setup in Fig. 2.2.

For the loss measurement of the Rb vapor cell we don't consider the optical

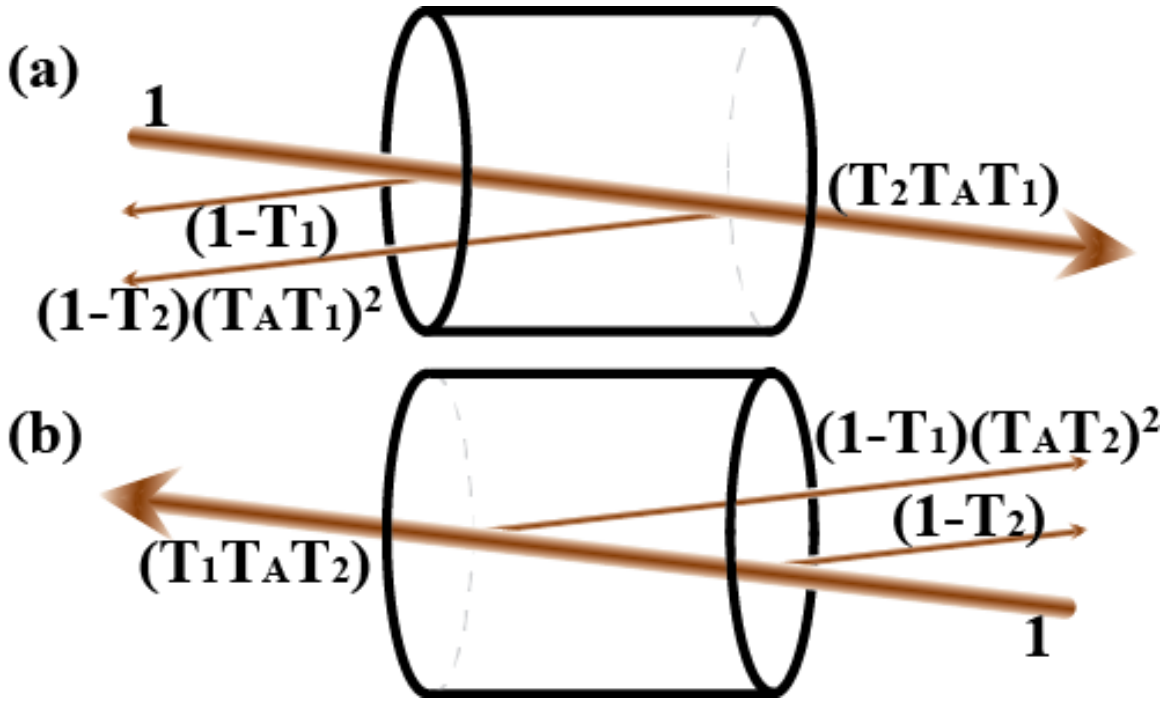

Figure 2.4: The transmittance measurement of the Rb cell. The transmittances of the left window and the right window are T_1 and T_2. We assume that the transmission of the light through the atoms is T_A. The diagram shows the reflected light and transmitted light from the windows of the Rb vapor cell for the incident beam in the (a) positive x direction and (b) negative x direction.

loss that occurs before the 4WM is generated, from the first window, for the quantum efficiency calibration. Only the optical loss on the generated twin beams will contribute to the correction of the quantum efficiency. The transmittance of each window of the Rb cell can be simply measured from the reflected light off of each window, as shown in Fig. 2.4. For an incident beam with a normalized input power of 1, the reflected power from each window is $(1-T_1)$ and $(1-T_2)$ for transmittances of T_1 and T_2 assuming no absorption from the window [36]. The transmission of the Rb atoms, T_A, can be determined from the total transmission along with the measured transmittance of each window. The reflected light from the second window can be used in the "overdetermined" approach, that is there are three equations for two unknown values, for the transmittance measurement. This helps by providing information on the uncertainty of the results.

For the NIST calibration the relative combined standard uncertainty is usually around 0.1% at the wavelength of 800 nm [37]. To compete with the NIST calibration we need a good loss measurement for our system. For the loss measurement in our system the relative standard uncertainty of lenses and mirrors are around 0.01%. For the transmittance measurement of a single window the uncertainty is around 2% at the room temperature. We have the same setup, as shown in Fig. 2.2, for the transmittance measurement of a window and paired lenses. The transmitted power after the window drifts, (Fig. 2.6), a lot more than the measurement of pair lenses, (Fig. 2.5). This is the main challenge in our loss measurement.

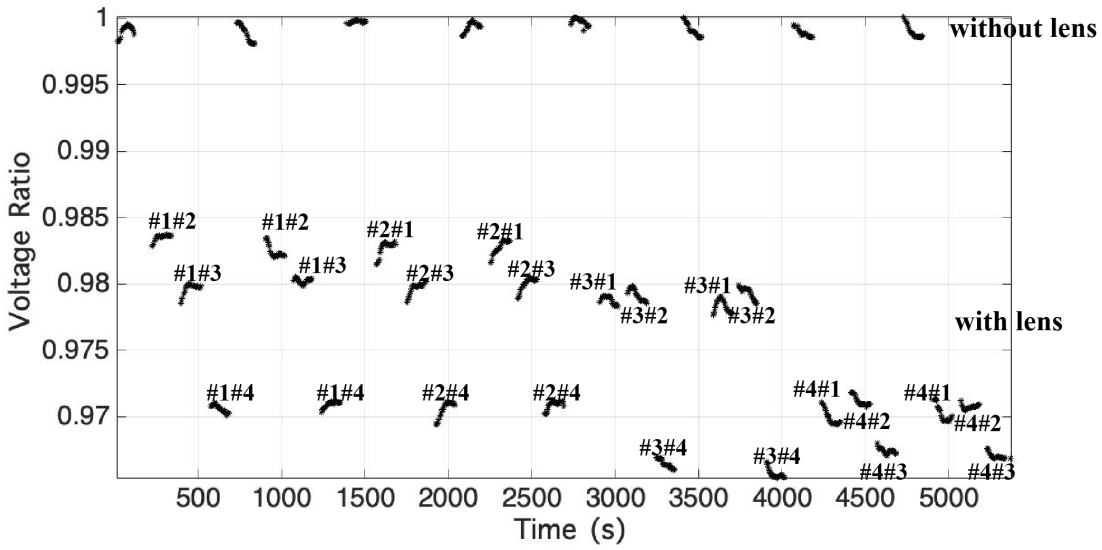

Figure 2.5: The transmittance measurements of paired lenses by using the setup of Fig. 2.2. There are four lenses under test. The signal is normalized using the monitor signal. "#1#2" means the combination of the lens number 1 and lens number 2 is under test.

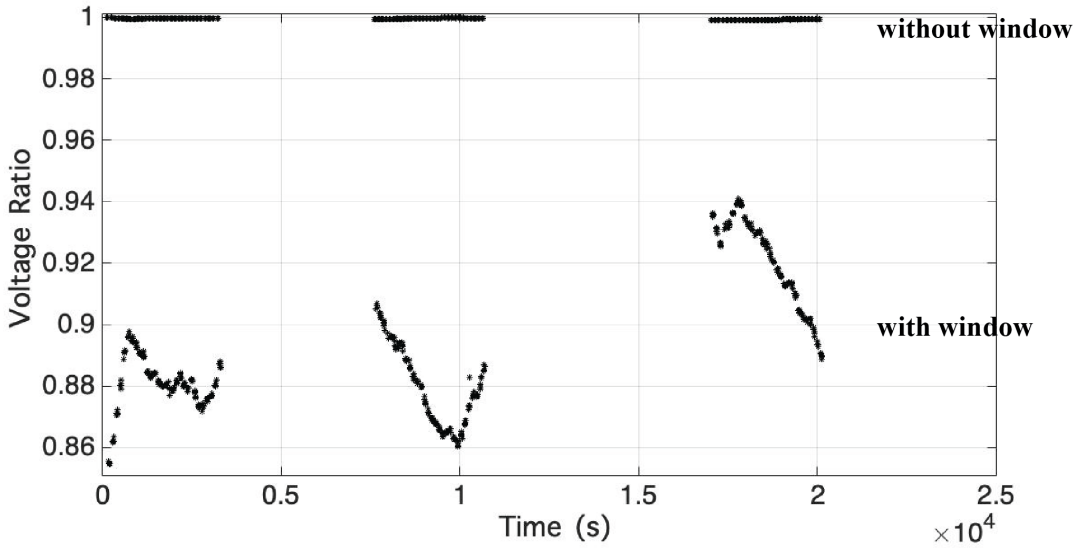

Figure 2.6: The transmittance measurement of a single window by using the setup of Fig. 2.2. The signal is normalized using the monitor signal. The value at around 1.0 is the voltage ratio without the window under test.

2.4 Discussion

For the calibration of photodiodes using twin beams from 4WM the quantum efficiency can be derived from Eq. 2.27 and 2.28. To obtain the quantum efficiency in the equations we need the correlation functions and the gain of the probe beam. The measurement of the gain is the power ratio of the amplified probe beam to the probe seed beam. The estimation of the gain of the probe beam will introduce another uncertainty when we try to measure the probe seed power and the amplified probe power within some time period. To obtain the gain, we can either have another monitor for the probe seed power or measure the power ratio of the amplified probe beam and the conjugate beam [28]. We express the gain of the probe beam in terms of the photocurrent ratio, r_{cp}, of the conjugate beam and the amplified probe beam from Eq. 2.5, 2.6, Eq. 2.14, and 2.16 so that the uncertainty from the estimation of the gain can be avoided,

$$r_{cp} = \frac{\langle \hat{i}_c(t) \rangle}{\langle \hat{i}_p(t) \rangle} = \frac{\eta_c g_c (G-1)}{\eta_p g_p G}, \tag{2.29}$$

$$G = \frac{\eta_c g_c}{\eta_c g_c - \eta_p g_p r_{cp}}. \tag{2.30}$$

With the power ratio, r_{cp}, the quantum efficiencies of the photodiodes, Eq. 2.27 and 2.28, can be rewritten as

$$\eta_p = \frac{1}{2}\left(1 + \frac{g_c}{g_p}\frac{i_{pc} - i_{pp} r_{cp}}{i_{cc} - i_{pc} r_{cp}}\right), \tag{2.31}$$

$$\eta_c = \frac{i_{pc} r_{cp}}{2(i_{cc} - i_{pc} r_{cp})} \left(\frac{g_c i_{pc}}{g_c i_{pp} r_{cp} - g_p i_{cc} + g_p i_{pc} r_{cp}} - 1 \right). \tag{2.32}$$

This gain-independent calibration scheme eliminates the uncertainty from the estimation of the gain. However, we might underestimate the loss in the amplified probe beam from the atomic absorption and this causes an error in the calibration of the quantum efficiency. Remember that we defined the gain of the probe beam as G in Eq. 2.7 after we showed that the difference between the expectation values of the amplified probe beam and the conjugate beam is the expectation value of the probe seed. In the real situation, the power difference between the amplified probe beam and the conjugate beam is always smaller than the probe seed power.

We can improve the estimate of the gain of the probe beam from the higher order correlation functions of the current fluctuations.

$$\begin{aligned}
\langle \delta\hat{i}_p(t)\delta\hat{i}_p(t+\tau_1)\delta\hat{i}_c(t+\tau_2)\rangle &= \langle \hat{i}_p(t)\hat{i}_p(t+\tau_1)\hat{i}_c(t+\tau_2)\rangle - 2\langle \hat{i}_p(t)\rangle\langle \hat{i}_p(t)\hat{i}_c(t+\tau)\rangle \\
&\quad - \langle \hat{i}_p(t)\hat{i}_p(t+\tau)\rangle\langle \hat{i}_c(t)\rangle + 2\langle \hat{i}_p(t)\rangle^2\langle \hat{i}_c(t)\rangle \\
&= \{2G(G-1)\eta_p\eta_c[(3G-2)\eta_p + 1]|\alpha|^2 \\
&\quad + G(G-1)\eta_p\eta_c[2(G-1)\eta_p + 1]\} \times g_p^2 g_c f(t),
\end{aligned} \tag{2.33}$$

$$\begin{aligned}
\langle \delta\hat{i}_p(t)\delta\hat{i}_c(t+\tau_1)\delta\hat{i}_c(t+\tau_2)\rangle &= \langle \hat{i}_p(t)\hat{i}_c(t+\tau_1)\hat{i}_c(t+\tau_2)\rangle - 2\langle \hat{i}_c(t)\rangle\langle \hat{i}_p(t)\hat{i}_c(t+\tau)\rangle \\
&\quad - \langle \hat{i}_c(t)\hat{i}_c(t+\tau)\rangle\langle \hat{i}_p(t)\rangle + 2\langle \hat{i}_c(t)\rangle^2\langle \hat{i}_p(t)\rangle \\
&= \{2G(G-1)\eta_p\eta_c[(3G-3)\eta_c + 1]|\alpha|^2 \\
&\quad + G(G-1)\eta_p\eta_c[2(G-1)\eta_c + 1]\} \times g_p g_c^2 f(t).
\end{aligned} \tag{2.34}$$

We ignore the spontaneous emission part, that is we assume that $|\alpha|^2 \gg 1$,

and define higher order correlation functions i_{ppc} and i_{pcc} as

$$i_{ppc} = 2G(G-1)\eta_p\eta_c[(3G-2)\eta_p + 1]g_p^2 g_c, \tag{2.35}$$

$$i_{pcc} = 2G(G-1)\eta_p\eta_c[(3G-3)\eta_c + 1]g_p g_c^2. \tag{2.36}$$

We define a parameter R_{cp}, the ratio of higher order correlation functions, that we can use to estimate the gain of the probe beam,

$$R_{cp} = \frac{\langle \delta\hat{i}_p(t)\delta\hat{i}_c(t+\tau_1)\delta\hat{i}_c(t+\tau_2)\rangle}{\langle \delta\hat{i}_p(t)\delta\hat{i}_p(t+\tau_1)\delta\hat{i}_c(t+\tau_2)\rangle} \approx \frac{i_{pcc}}{i_{ppc}} = \frac{[(3G-3)\eta_c + 1]g_c}{[(3G-2)\eta_p + 1]g_p}. \tag{2.37}$$

The gain of the probe beam, in Eq. 2.30, can be rewritten as

$$G = \frac{g_p R_{cp}(2\eta_p - 1) - g_c(3\eta_c - 1)}{3(g_p R_{cp}\eta_p - g_c\eta_c)}. \tag{2.38}$$

With a new way to estimate the gain of the probe beam we can obtain the quantum efficiencies, in Eq. 2.31 and 2.32, from correlation functions only:

$$\eta_p = \frac{1}{2}[1 + \frac{g_c}{g_p}\frac{i_{pc}^2 + 2i_{pp}i_{cc} - 3i_{pp}i_{pc}R_{cp}}{3i_{cc}i_{pc} - R_{cp}(i_{pc}^2 + 2i_{pp}i_{cc})}], \tag{2.39}$$

$$\begin{aligned}\eta_c = \frac{1}{2}&\frac{i_{pc}(i_{pc}R_{cp} - 2i_{cc})}{3i_{cc}i_{pc} - R_{cp}(i_{pc}^2 + 2i_{pp}i_{cc})}\times \\ &[\frac{g_c i_{pc}(2i_{pp}R_{cp} - i_{pc})}{g_p(3i_{cc}i_{pc} - i_{pc}^2 R_{cp} - 2i_{pp}i_{cc}R_{cp}) + g_c i_{pp}(2i_{cc} - i_{pc}R_{cp})} - 1].\end{aligned} \tag{2.40}$$

Squeezed light is a promising quantum light source for the absolute calibration for photodiodes. An absolute calibration with 0.5% ($k = 2$) uncertainty was

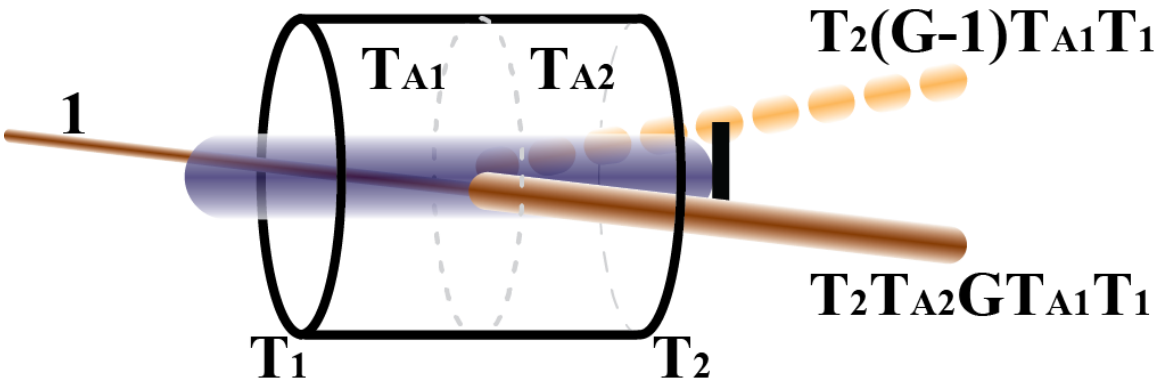

Figure 2.7: Loss measurement of the amplified probe beam. The probe (brown), conjugate (yellow), and pump (purple) are indicated. The transmittance of the left window and the right window are T_1 and T_2. We define T_{A1} as the transmittance of the atoms in the region before the twin beams are generated and T_{A2} is the transmittance of the region of the amplified probe.

achieved by Vahlbruch *et al.* [29] using single-mode squeezing. The limitation of the uncertainty is from the loss measurement of the optical systems, the optical parametric amplification (OPA) escape efficiency and the coupling mirror transmissivity. In our 4WM system, the challenge is the loss measurement of the second window on the Rb cell and the loss of the amplified probe beam through the atoms. The transmittance of the window can be measured from the reflectance, shown in Fig. 2.4, and the measurement changes with its temperature due to interference of the internal reflections *within* the window. This could be avoided with a temperature controller. Loss from the atoms is harder to estimate. The twin beams are generated in the Rb cell and propagate in the cell for a certain distance until they reach the second window. While propagating in the Rb vapor the amplified probe beam experiences more loss from the atomic absorption than the conjugate beam because it is closer

to the atomic resonance. We can estimate this loss from the power ratio of the amplified probe beam and the conjugate beam, shown in Fig. 2.7. For the probe seed beam with a normalized input power of 1, the power of the amplified probe beam, P, and the conjugate beam, C, are

$$P = T_2 T_{A2} G T_{A1} T_1 \tag{2.41}$$

and

$$C = T_2 (G-1) T_{A1} T_1, \tag{2.42}$$

where the transmittance of the first window and the second window are T_1 and T_2. The transmittance of the atoms for the probe seed beam and the amplified probe beam are T_{A1} and T_{A2}. The loss from the atoms for the conjugate beam is negligible because the conjugate beam is far off resonance. The loss of the amplified probe beam, T_{A2}, can be expressed in terms of the gain of the probe beam and the power ratio of the twin beams,

$$T_{A2} = \frac{(G-1)P}{GC}. \tag{2.43}$$

The gain of the probe beam, G, is given by the Eq. 2.38. The quantum efficiencies, η_p and η_c, in the equation of the gain can be replaced by the correlation functions, shown in Eq. 2.39 and 2.40. The estimates of the loss and the gain of the probe beam can be verified by calibrated photodetectors with known quantum efficiencies.

The bandwidth of the 4WM process in our system is around 10 to 20 MHz. We can do the absolute calibration with twin beams for measurement frequencies

below around 10 MHz. Obtaining squeezing at acoustic measurement frequencies is not easy for the seeded 4WM scheme. The probe seed beam itself is a noise source that degrades the squeezing at low frequencies. In next chapter, we introduce a dual-seeded 4WM scheme that allows us to observe squeezing at frequencies below 10 Hz. With the dual-seeded 4WM scheme, we can perform absolute calibrations in the frequency range of 10 Hz to 10 MHz. Besides the dual-seeded 4WM scheme, we can simply send a second probe seed beam from the same source around the gain as a monitor signal for the power loss fluctuations due to the absorption from the Rb atoms.

Finally, we can do the absolute calibration again with the probe seed beam at the conjugate color to verify our measured quantum efficiencies. With the same setup and the same optical alignment we expect the same calibration result if we consider all the losses properly.

2.5 Conclusions

The quantum correlated twin beams can be used for the calibration of photodetectors [38, 39]. The absolute calibration with the 4WM process was proposed by Marino *et al.* [28]. The measurement of the gain of the probe beam from the power ratio of the amplified probe beam and the probe seed beam will introduce an uncertainty into the calibration. The power ratio of the probe and conjugate beams can be monitored simultaneously to reduce errors due to temporal drifts. We note that the loss on the amplified probe beam from the atomic absorption is

not included in the gain estimation, which may cause the measured probe channel quantum efficiency to be smaller than the conjugate channel efficiency.

We developed another gain-independent calibration scheme with higher order correlation functions that gives the gain of the probe beam without correction for loss of the amplified probe beam. Although we can also use the auto-correlation functions of the probe and conjugate beams to estimate the gain, the "overdetermined" approach with higher order correlation functions might improve the uncertainty.

We have presented some loss measurement setups for the lens and mirror. The setup for the transmittance measurement can also be used to measure the relative quantum efficiency between trap detectors. The loss measurement for each window of the Rb vapor cell can be simply obtained from the reflectance of the windows. This reduces the error in transmittance estimation from the total transmission of both windows and atoms. With a better gain measurement from correlation functions, the loss of the amplified probe beam in the Rb cell can be estimated from the photocurrent ratio of the twin beams. The loss from each optical element must be included to correct the photocurrent for the atomic absorption measurement.

The uncertainty of the absolute calibration is mainly from the loss measurement [29]. We estimate the uncertainty of the loss measurement for each optical element in our 4WM system to be $\approx 0.05\%$ [35, 40]. However, the uncertainty of the loss measurement for the window is higher due to the temperature drift of the Rb cell. The uncertainty is $\approx 2\%$ for the loss measurement of window at the room temperature. This is our main source of the uncertainty for the absolute calibration. The uncertainty could be even higher for the loss measurement of window at

high temperature, for example 120°C. Although the uncertainties of the loss measurements limit us compared to traditional calibrations, our main goal is absolute calibration without the need for a calibrated detector as the reference. With a good temperature control for the Rb cell we might still be able to reach a level that is competitive with the traditional calibration at NIST.

Chapter 3: Squeezed Light at Low-frequency

3.1 Introduction

Quantum-enhanced sensing technologies have become increasingly important in a number of fields as the limitations of classical technologies are approached. It will be important for certain applications to perform sub-shot-noise measurements at low frequencies. In particular, gravity-wave interferometers [20, 41] operate in the audio frequency range of 10 Hz to 10 kHz and presently employ single-mode quadrature squeezing, but a number of other potential low-frequency applications of squeezing are possible. These include quantum information storage in optical memories based on electromagnetically-induced transparency, opto-acoustic or thermo-optical spectroscopic techniques [42, 43], as well as magnetometry [44]. Detector calibration techniques involving squeezed light [28, 29] would also benefit from operation at frequencies as low as 100 Hz, as this is where current metrological calibrations are performed [37]. Sub-shot-noise direct intensity-difference measurements on a CCD camera are also an important goal. That, along with relatively portable and affordable sources, such as those based on diode laser systems, would greatly expand the range of potential applications outside of a laboratory setting.

Much of this chapter was published in Ref. [45], where we show how to extend

the generation of bright, two-mode, intensity-difference squeezed light from 4-wave mixing (4WM) in Rb vapor to low frequencies using a diode-laser-based system. In particular, we introduce a dual-seeding technique where two complementary 4WM processes are seeded in order to balance the excess noise due to the seed beams themselves. The present results imply that the squeezing produced by this 4WM process has been previously limited at low frequencies only by technical noise, and thus single-mode quadrature squeezing based on the same 4WM interaction ought to also be extendable down to a similar frequency range.

Twin-beam generation, which produces two entangled beams of light, has long held the promise of being able to bring sub-shot-noise measurements to a variety of applications. A technique called quantum-dense metrology involves measuring two orthogonal quadratures of a frequency-degenerate two-mode squeezed state in order to discriminate against noise leakage between quadratures and remove common-mode classical noise [46,47], and has been proposed for use in gravitational-wave detectors. A direct application to interferometry has also been proposed [48]. Differential-absorption imaging [49] allows sub-shot noise signals to be extracted from the difference of two highly-correlated images. A particularly simple twin-beam generation technique, 4-wave mixing in alkali vapors, has always seemed promising in this regard because the squeezing can be generated in many spatial modes. Observing such squeezing on an integrating detector, like a CCD camera, requires that the light be squeezed when integrated over the entire frequency range of the measured pulse of light, and holds the promise of demonstrating a real quantum sensitivity advantage for a camera array with fixed well-depth pixels. Unfortunately, technical

noise at low frequencies has proven to be a severe limitation in this regard.

Generating squeezing at acoustic frequencies (< 20 kHz) has been pursued in a number of different systems. The lowest frequency squeezing has been observed in single-mode quadrature squeezing, but 2-mode squeezing and polarization squeezing have also been pushed down into the acoustic frequency range. Single-mode quadrature squeezing has perhaps its most important applications in future gravity-wave interferometers [50–52], and such squeezing at frequencies as low as 1 Hz has been observed from an optical parametric oscillator (OPO) with this application in mind [52, 53]. Squeezing has not been reported at such low frequencies for two-mode intensity-difference measurements, and the best results seem to be ≈ 1.5 kHz reported in [54], and ≈ 700 Hz recently reported in [55].

Obtaining squeezing at low frequencies is generally not an easy task, and in the single-mode-squeezing case the above-mentioned results were obtained using a complex system employing two additional frequency-shifted control beams to sense and to feed back on the OPO cavity length and the pump phase. In contrast, the results presented here demonstrate intensity-difference squeezing down to ≈ 10 Hz using an extremely simple, passive optical system (in the sense that there is no active feedback to the optical system beyond the stabilization of the seed laser).

Early OPO systems were constructed with $\chi^{(2)}$ nonlinear crystals in external cavities that enhance the pump field as well as the down-converted fields. These cavities resulted in a high sensitivity to acoustic noise, which limited the squeezing at these frequencies. The use of semimonolithic and monolithic cavity designs, incorporating the cavity into the nonlinear crystal, substantially reduced this sensi-

tivity to noise, and with feedback locking eventually led to the 1 Hz results discussed above. Broadband spontaneous parametric downconversion (PDC) systems that are pumped without cavities have been reported where twin-beam differencing can be performed on an integrating detector, but the photon flux per mode is usually low, requiring a relatively high-power pulsed laser system. For imaging purposes PDC has potentially very high resolution, with many spatial modes. Correlations in the speckle patterns, pixel-by-pixel correlations, and imaging have been demonstrated with these systems [56–59]. Recently Samantaray *et al.* [60] worked with continuous-wave pumping and 100 ms integration times to demonstrate an improved imaging system. An important feature that is common to each of these experiments is that there is no seed beam present, which eliminates the noise associated with the seed.

A different type of squeezing, polarization squeezing, or a squeezing of the Stokes parameters, has also been experimentally observed at low frequencies. This is, in particular, useful for magnetometry applications and has been pushed down to the kHz regime [61], and to $\approx$ 200 Hz in [62]. This particular type of squeezing, however, does not lend itself to the imaging applications that we are interested in (see Chapter 4).

Previous experiments have reported twin-beam intensity-difference squeezing from 4WM down into the kHz range [54,63,64]. Very recently Ma *et al.* [55] reported such squeezing down to frequencies below 700 Hz. In the context of imaging, Kumar *et al.* [65] performed intensity-differencing on an EMCCD camera using a 4WM source similar to ours and were able to obtain a subtraction noise level 2 dB below shot noise. In those experiments two frames are taken in rapid succession for each of

the twin images and are subtracted. This results in images that contain the intensity fluctuations of each beam and removes much of the low-frequency classical noise.

Producing bright twin beams typically requires seeding the beams, but the seeding itself often limits the low-frequency squeezing performance. Here we present a number of improvements to our established 4WM optical set-up that allow bright, low-frequency intensity-difference squeezing to be observed down to frequencies that are limited by the laser beam-pointing stability. We show that we can balance the noise of the seed beam itself by creating two "complementary" seeded 4WM processes that balance the seeds on the two detectors. In addition, in this context we demonstrate the benefits of frequency-narrowing of the diode laser, and of increasing the phase-matching angle. While a number of the techniques introduced here are also applicable to systems based on intrinsically less-noisy technologies, such as Ti:sapphire lasers, we use semiconductor diode laser and tapered amplifier technologies. It is important for practical uses that these more portable and affordable technologies work at these frequencies as well.

3.2 Experiments

While a 4WM process that generates twin beams that are degenerate in frequency is possible in Rb vapor, the strongest and most easily generated 4WM process is a non-degenerate scheme pumped by a single frequency of light [15], as indicated in Fig. 3.1. A seed at the probe frequency is crossed with the pump beam at a small angle in a vapor cell and generates twin beams (an amplified probe and its

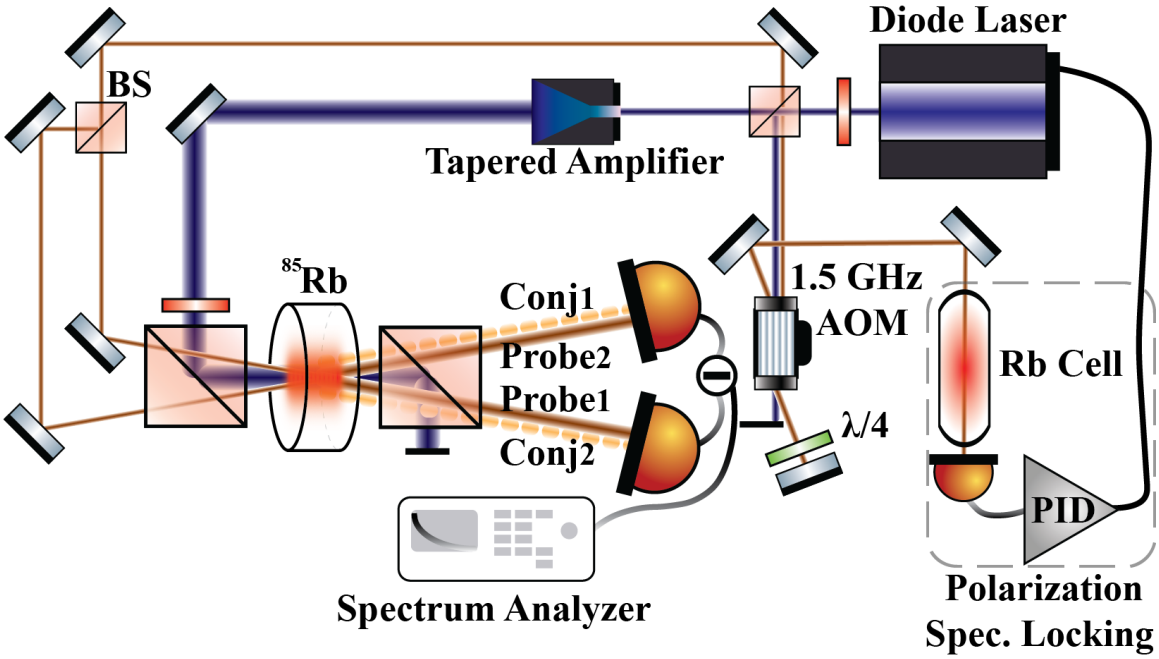

Figure 3.1: Experimental set-up. BS: a non-polarizing beamsplitter; the remaining beamsplitters are polarizing beamsplitters. The dashed box indicates a polarization spectroscopy feedback lock at laser frequency.

conjugate), on opposite sides of the pump. For a seed with a normalized input power of 1, the amplified output probe beam then has a power numerically equal to G (the value of the 4WM gain), and the beam at the conjugate frequency has a power numerically equal to $G-1$. The frequencies of the beams differ by ≈ 6 GHz, and these beams are sent to separate, matched photodiodes in a balanced detector package. The photocurrents are directly subtracted and then amplified, and the noise power is measured with an RF spectrum analyzer. We employ a number of techniques to compensate the DC imbalance of the beams in this configuration and compare the results.

In addition to the intensity balancing techniques discussed below, we can change the conditions of 4WM so as to increase the phase-matching angle. This choice generally results in less 4WM gain and bandwidth. Nevertheless, the larger phase-matching angle reduces the collection of scattered pump light by the detectors. The associated reduction in gain can be recovered to some degree with increased cell temperature (i.e., increased atomic density). With non-integrating detectors the inclusion of a delay line is necessary to compensate for the differing group velocities of the probe and conjugate beams, particularly at higher measurement frequencies [64, 66]. Finally, the locking and frequency-narrowing of the diode seed laser is also important. Using these techniques together we have observed sub-shot-noise intensity-difference signals at frequencies below 10 Hz, and more than 5 dB of squeezing at 20 Hz and above.

The 4WM process and experimental set-up that we use is sketched in Fig. 3.1 and is similar to that of Refs. [15, 64]. A grating-tuned diode laser emitting 90 mW

provides the seed for the tapered-amplifier (pump) as well as the seeds for the 4WM "probe" beams. Approximately 30 mW of light is used to seed a 2 W tapered amplifier. This light is sent through an optical fiber to create a pump beam of $\approx$ 1.5 mm $1/e^2$ diameter with 750 mW of power that is detuned in the range of $\Delta = 800$ MHz to 1.3 GHz to the blue of the $S_{1/2}$ (F=2) $\rightarrow P_{1/2}$ (F=3) transition in ^{85}Rb. The Rb cell is 1.2 cm long and is heated to a temperature of approximately 120 °C. A pair of seed beams at the probe frequency can be introduced on either side of the pump, at a small angle ($\approx$ 0.3 degrees to 0.5 degrees) relative to the pump beam which allows phase-matching of the 4WM process. The probe seed beams have a $1/e^2$ diameter of 0.55 mm and are derived from the diode laser beam by double-passing a fraction ($\approx$ 45 mW) of its output through a 1.5-GHz acousto-optic modulator (AOM), resulting in a stable two-photon detuning of $\delta = -2$ MHz for the process. The detectors have a quantum efficiency of $\approx 95\%$ at 795 nm.

Most of the experiments using this 4WM system have been performed using Ti:sapphire lasers because of their superior beam quality and noise properties. Diode laser/tapered amplifier systems, however, will most likely be required for this sort of squeezing to become portable and useful outside of the lab. Unfortunately, these systems are especially noisy (above shot noise) at low frequencies. In particular, if one derives the probe-frequency seed beam from the output of a tapered amplifier, it can have relatively large amounts of technical noise. In our case, we derive our seed beam(s) by frequency-shifting part of the direct output of our diode laser with a double-passed AOM and coupling into a fiber. Inevitably, extra noise, particularly at low frequencies, is also introduced onto the probe seed beam(s) by the RF amplifier

and beam-pointing instabilities are converted to amplitude instabilities by the AOM and the fiber coupling.

The diode laser can be frequency-narrowed by locking it to a polarization spectroscopy signal in a warm Rb vapor reference cell [67]. This stabilizes the laser against drifts but also narrows the laser linewidth from $\approx$ 200 kHz to $<$10 kHz, full width at half-maximum (FWHM). This locking significantly affects the low-frequency squeezing performance, as described below.

If we input a single seed beam into the 4WM cell we obtain probe and conjugate beams with strong quantum correlations in the MHz frequency range. Our limitation on the squeezing at low frequencies results from the imbalance caused by the presence of the seed. At DC the seeded and unseeded beams will have different intensities, and that difference will change at low frequencies as the gain fluctuates. This imbalance is partially offset by some amount of absorption at the probe frequency, because it is closer to the atomic resonance, but there is always an imbalance at DC. Attenuating the amplified seeded beam to balance the intensities is effective, however this will also reduce the measured low-frequency squeezing if the seed beam is not shot-noise-limited. This can be a particular problem if there is a large amount of gain noise at low frequencies. (For example, by changes in the 1-photon detuning of the unlocked pump. In severe cases, when the noise becomes larger than the common-mode rejection of the balanced detector, the subtraction will be imperfect.) We show in Fig. 3.2 how the low-frequency limit of the squeezing is improved for a lower seed power, with otherwise identical conditions. This is because as we reduce the seed power, the shot noise dominates. The shot noise is measured with light directly

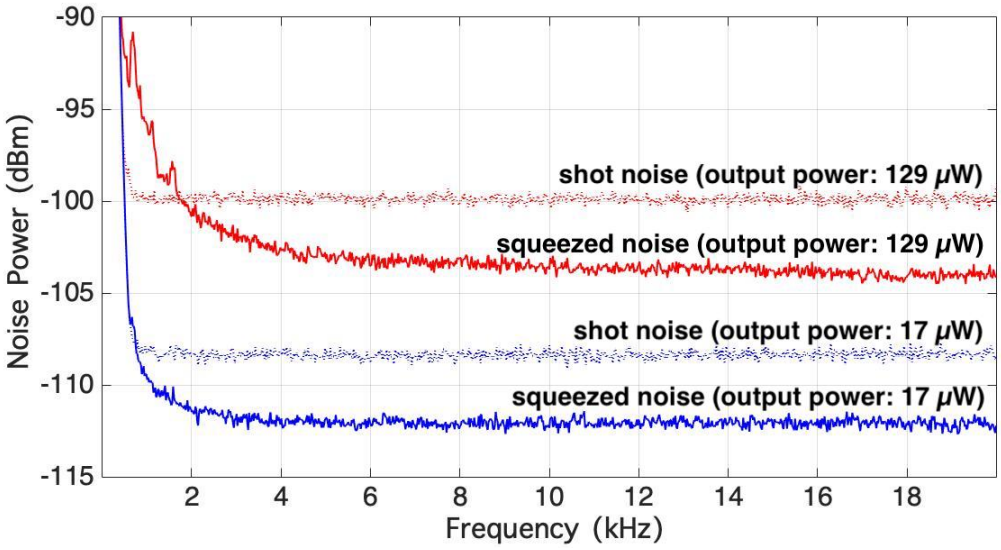

Figure 3.2: Noise power versus measurement frequency for different powers in the seeding beams. The 4WM gain ≈ 20 in each case (pump power = 420 mW, cell temperature = 128 ° C, $\Delta = 1.2$ GHz, $\delta = -2$ MHz, pump-probe angle of 0.5(1) degrees). The upper (red) curves show the measured shot noise and twin-beam intensity-difference squeezing for a seed power of 6.4 μW (output power ≈ 129 μW) and lower (blue) curves show the shot noise level and intensity-difference squeezing for a seed power of 0.9 μW (output power ≈ 17 μW). The resolution bandwidth (RBW) is 100 Hz and the video bandwidth (VBW) is 1 Hz for these measurements. The output beam powers here are unbalanced due to the injected seed beam. For equivalent conditions otherwise, the lower seed power results in the squeezing being extended to lower frequencies. The electronic noise is about 20 dB below the shot noise level and is not subtracted from these traces.

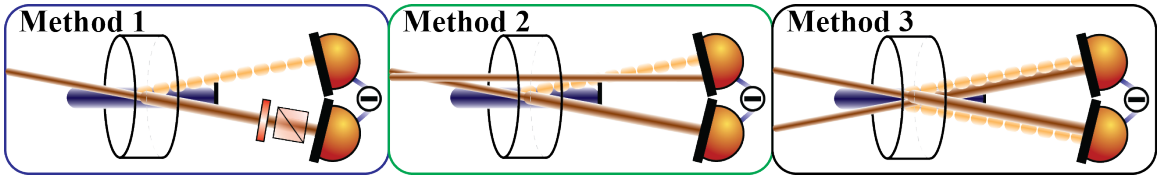

Figure 3.3: Three methods of reducing noise from the seed of the 4WM process: Method 1 - attenuating the amplified seeded beam using a half-wave plate and polarizing beamsplitter to balance the conjugate. Method 2 - the amplified seeded beam balanced by its conjugate and a second seed that goes around the gain. Method 3 - a dual-seeded process, with the two amplified seeded beams and their conjugates balancing on the two detectors.

from the diode laser, sent through a 50:50 beamsplitter onto two detectors, and we take the difference between the two detectors.

There are a number of techniques that can be used to balance the power in the two beams. We will show results from the three approaches indicated in Fig. 3.3. The simplest method (Method 1) is to attenuate the probe (seeded) beam. While this works to balance the average powers, it also slightly attenuates the correlations between the beams, thus reducing the overall squeezing level. In addition, if there are fluctuations in the gain, the fixed attenuation cannot compensate for them. A second approach (Method 2) is to generate two beams at the probe frequency from the same source, but only using one to seed the 4WM process. The amplified probe is sent to one photodiode, while the other beam is sent around the gain region in the cell and is brought to the other photodiode directly, along with the conjugate of the amplified probe. The probe-frequency seeds, in the absence of gain, can be balanced at the shot-noise level, while the light generated by the 4WM gain, at both

probe and conjugate frequencies, is balanced at a sub-shot-noise level. (Absorption in the vapor complicates this picture.) Finally, a third approach (Method 3) is to generate two seed beams and send equal amounts of probe light through the gain medium and onto each photodiode. This creates two pairs of twin beams, resulting in each detector seeing the two frequencies of light from one probe and one conjugate beam. (The probe and conjugate frequencies are sufficiently far apart ($\approx$ 6 GHz) that the beat note is not observable with the detectors used here.) The stimulated portions of the output beams (with power equal to $G - 1$ at each frequency and in each direction) are matched at sub-shot-noise levels on the two detectors, while the injected seed portions of the beams at the probe frequency are balanced on the detectors at the level of shot noise for the seed power. In next section, we analyze how these methods compare for generating squeezing at low frequencies.

3.3 Results

Two observations are important for the achievement of squeezing at very low frequencies. The first is that, while the angle between the seed and the pump partly determines the gain through the phase matching conditions, it also partly determines how much scattered pump light is collected by the photodetectors. The pump light is noisy at low frequencies, and therefore so is the scattered pump light. We observe an improvement in the low-frequency squeezing by increasing the angle between the pump and probe beams beyond that for optimal gain. The pump light is polarized orthogonal to the probe and conjugate beams at the input and is largely deflected

by the polarizing beamsplitter at the output of the 4WM cell. A small amount of pump light, however, is depolarized and scattered, primarily at small angles, and is collected by the detectors. This contributes a large background at low frequencies, when compared to the signal level.

At the cost of smaller gain, this scattering can be reduced by increasing the angle between the probe seed and the pump beam. In Fig. 3.4 we show the power spectrum of the scattered pump light along with the squeezing spectrum for two pump-probe angles. The typical optimal phase-matching angle is ≈ 0.3 degrees Ref. [64]. By increasing this angle to ≈ 0.5 degrees (at a cost of reducing the gain and the gain bandwidth) the scattering background can be reduced by enough to make a difference in the measured squeezing at very low frequencies. (The gain can be recovered by increasing the temperature of the Rb cell or changing the pump detuning, although absorption losses in the Rb vapor are increased as well.) It is apparent in Fig. 3.4 that the scattered pump light limits the low-frequency squeezing for the smaller phase-matching angle and that the low-frequency squeezing can be improved by increasing the pump-probe angle. We note that scattered pump light is not a concern for experiments employing homodyne detection, where interference with the local oscillator effectively provides a narrowband frequency filter, but it does affect direct intensity detection measurements.

The second important practical observation is that, as discussed above, for a single probe-conjugate pair it is the (unbalanced) injected seed light that is one of the major limitations to the squeezing. We see all of the low-frequency technical noise on the seed reproduced in the squeezing spectrum, as well as noise due to the changing

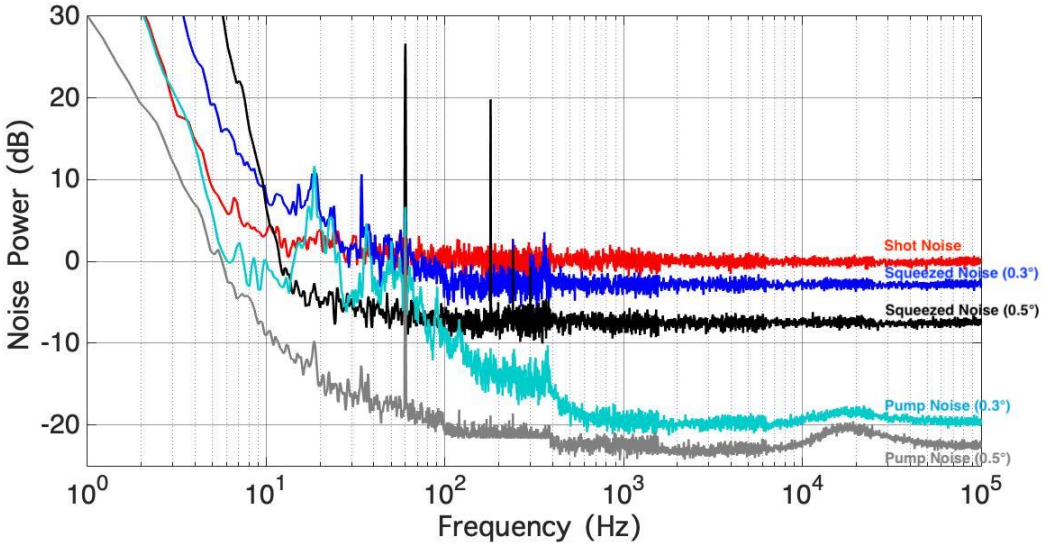

Figure 3.4: Spectra of shot noise, squeezing, and scattered pump light versus frequency, comparing two different phase-matching angles. In this case the 4WM process is dual-seeded (Method 3). The seed laser is locked at a one-photon detuning of 1.3 GHz and frequency-narrowed in each case, and no delay lines are inserted in any of the beams for these measurements. The two-photon detuning is kept at -2 MHz and the pump power is 750 mW. The plotted spectra (from the top at high frequency) are the a) shot noise measurement (red); b) intensity-difference squeezing with a phase-matching angle of 0.3(1) degrees, gain of 5, and cell stem temperature of 91 ° C (blue); c) intensity-difference squeezing with a phase-matching angle of 0.5(1) degrees, gain of 10, and cell stem temperature of 97 ° C (black); d) collected scattered pump light for an angle of 0.3(1) degrees (cyan); e) collected scattered pump light for an angle of 0.5(1) degrees (grey). All uncertainties are one standard deviation statistical uncertainties unless otherwise noted. Electronic noise is not subtracted from these traces, which limits the lower pump noise trace above 100 Hz. The RBW is 0.24 Hz for frequencies below 400 Hz, and progressively larger for higher frequencies, up to 62 Hz above 6 kHz.

imbalance caused by gain fluctuations in the 4WM. The squeezing can generally be improved by intentionally attenuating the stronger, seeded (probe) beam [63] (Method 1). In principle, it can remove the classical noise from the difference signal, but at the cost of reducing the squeezing a little bit. Gain fluctuations will still limit the performance, as this balancing can be optimized for only one fixed value of G, and the gain fluctuations will always result in some imbalance, and consequently excess noise. Since there tends to be more noise in the gain at low frequencies than at higher frequencies, this tends to limit the squeezing in that regime first. In Figs. 3.5 and 3.6 we compare the three approaches to balancing the beams for the two situations of the seed laser being unlocked (Fig. 3.5), and that laser being locked and frequency-narrowed (Fig. 3.6).

Method 2, described in Fig. 3.3, allows one to overcome certain sources of noise in the seed beam by balancing part of the power of the amplified probe beam on one photodiode with that of a separate, un-amplified seed beam derived from the same source (along with the conjugate beam) on the other photodiode. The results of this approach (Fig. 3.5), make clear that this technique provides a substantial improvement over Method 1, particularly for the unlocked laser. This method allows for nearly balanced powers on each photodiode along with a straightforward means to cancel any classical noise on the seed beam itself. However, this method does not provide a means for canceling any noise that arises due to fluctuations in absorption of the probe seed in the gain region of the vapor cell. Such fluctuations might result from fluctuations in the 1-photon detuning of the pump beam.

Method 3 provides a means to overcome excess noise due to fluctuations in

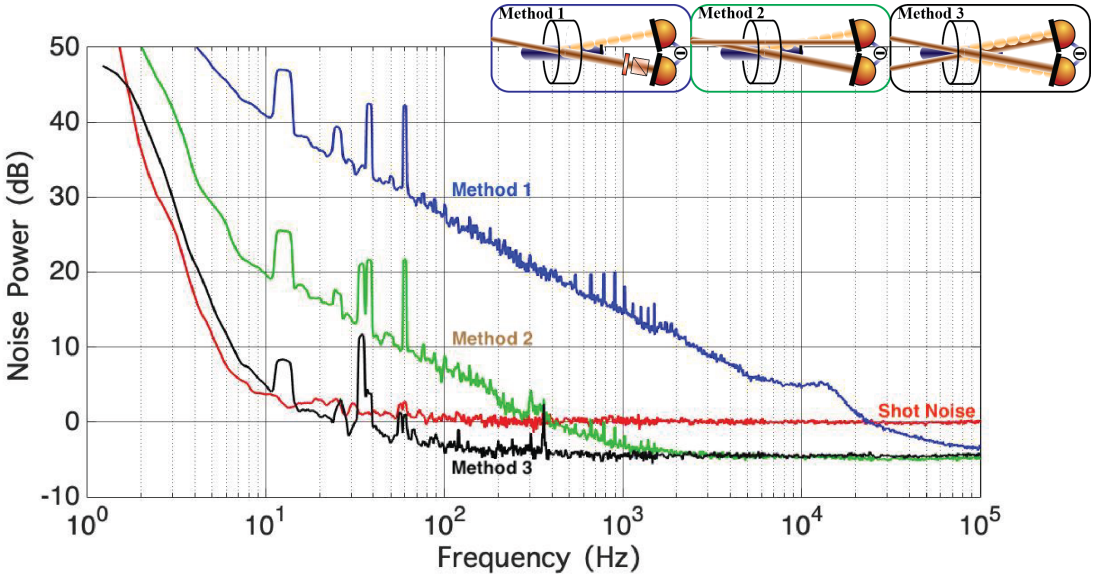

Figure 3.5: Spectra of shot noise and intensity-difference squeezing versus frequency, comparing seeding techniques. The one-photon detuning is 1.3 GHz, the gain is 10, the cell stem temperature is 97 °C, the phase-matching angle is 0.5(1) degrees, and the seed laser is unlocked. The traces are the shot noise measurement (red); intensity-difference squeezing with an attenuated probe beam (Method 1, blue); intensity-difference squeezing with an extra probe seed added to the conjugate beam at the detector (Method 2, green); intensity-difference squeezing with dual probe seeds (Method 3, black). There is a delay line for the conjugate beams in each case, which was included for ease of combining beams on the detectors. (The delay line makes no difference at low frequencies.) The measurements were taken with a box enclosing the beam paths after the 4WM cell. The electronic noise, about 20 dB below the shot noise, is not subtracted from these traces. The RBW is 0.24 Hz for frequencies below 400 Hz, and progressively larger for higher frequencies, up to 62 Hz above 6 kHz. A running average over 11 points (±1% at the measurement frequency) is used to smooth the data.

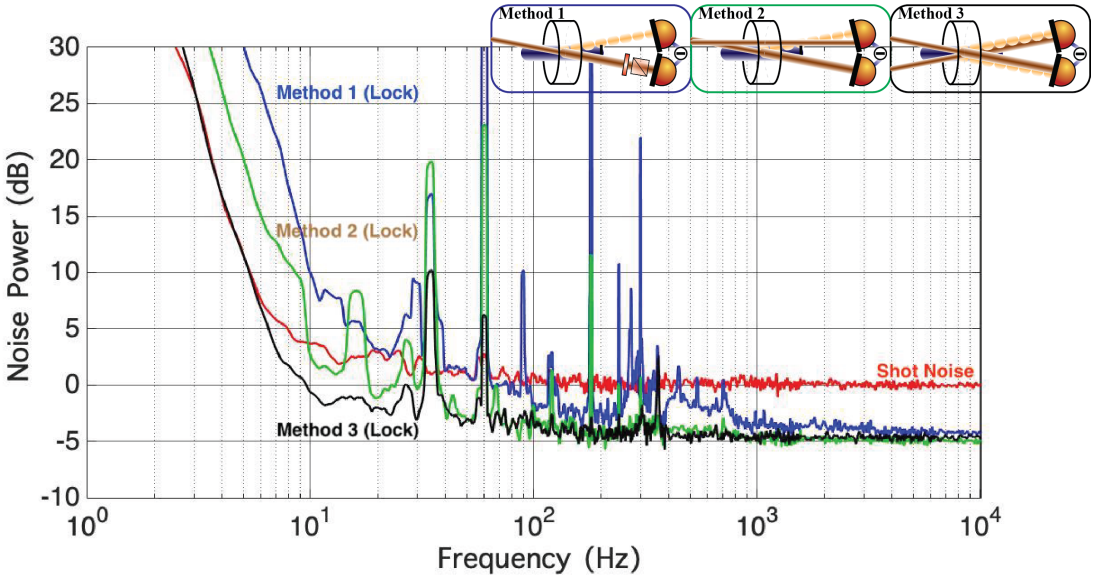

Figure 3.6: All the conditions of each trace are the same as Fig. 3.5 except for the laser is locked and frequency-narrowed for each trace in this figure

the 4WM gain and the absorption. As shown in Fig. 3.3 Method 3 involves two 4WM processes (1 and 2) generated by the dual-seeding. We detect probe 1 and conjugate 2 on one photodiode, and probe 2 and conjugate 1 onto the second photodiode, so that each diode sees a power of $2G-1$ times the input seed power(s). The seeds now balance to the shot noise level, even with noisy bright seeds and relatively low gain, and the amplified portions of the probe beams can balance to well below the shot noise level with the generated conjugate beams. The result of introducing the two probe-frequency seed beams simultaneously in this way is shown in Fig. 3.5. The low-frequency squeezing is noticeably improved beyond Methods 1 and 2 by balancing the beams in this way.

To achieve the best low-frequency results, the seed laser itself needs to be

stable. The polarization spectroscopy lock of the diode laser indicated in Fig. 3.1 stabilizes the drift of the diode laser frequency over the long term but, given that its detuning from the atomic resonance is $\approx$ 1300 MHz, the stabilization of this one-photon detuning is probably not crucial to the squeezing performance. The two-photon detuning and the coherence of the seed are established by an RF source and an AOM, and are also quite stable. In our experiments, however, the lock also takes out many fast frequency fluctuations and narrows the laser to $<$ 10 kHz linewidth, and we feel that this is also an important feature of the lock. In Fig. 3.6 we show how this laser lock impacts the intensity-difference squeezing at low frequencies. It is clear that locking is particularly important at the lowest frequencies.

A complication of the non-degenerate 4WM scheme is that the group velocities in the vapor cell at the probe and conjugate frequencies are different, leading to intensity fluctuations in the conjugate beam running ahead of those in the probe [66]. This results in the need for a delay line in the conjugate beam of about 10 ns, depending on the conditions (in particular the two-photon detuning), in order to optimize the squeezing [64]. This primarily affects the squeezing observed at frequencies higher than about 5 MHz. Delay lines are only included in the present experiments to facilitate combining the multiple beams on the photodetectors.

Finally, beam jitter, or beam-pointing instabilities can couple noise into the present measurements in several different ways. In addition to the beam pointing coupling through the varying efficiency of the AOM, or via optical fiber coupling, the non-uniformity of the photodiodes themselves can have an important effect. McKenzie *et al.* [68] observed that below about 200 Hz beam-pointing instabilities

were big enough that the conversion of beam motion on the diode into apparent intensity noise becomes significant. A box was placed around the beams after the 4WM cell in our apparatus to protect the beams from air currents in the laboratory and was required for the consistent observation of squeezing at frequencies below about 20 Hz.

3.4 Discussion

Careful power balancing, laser locking/narrowing, and a large phase-matching angle all contribute to being able to observe squeezing down to low frequencies. We have obtained squeezing down to frequencies < 10 Hz, limited only by the general stability of the optics and laboratory environment. The 4WM process is not fundamentally limited at low frequencies, and the single-pass-gain optical system used here does not couple acoustic noise into the measurements as a build-up cavity would. The pointing instability of the beams due to air currents surrounding the warm vapor cell seems to be a major contributor to the remaining low-frequency limitations in the system.

The input seed beams for the 4WM processes are constructed with a simple beamsplitter, and thus they have the identical spatial mode structure. The output beams will also reflect the same spatial mode structure, although the beams will perhaps be somewhat distorted by Kerr lensing in the gain medium. The distortions can, in principle, be corrected for, and the intensity subtractions can be made mode-by-mode. Perhaps a more straightforward method would be to employ flat-top

beam-shaping optics for the pump, which could eliminate the lensing and reduce the Kerr effect here to uniform phase shifts across the beams. In that case, with a careful alignment, the probe and conjugate beams could be overlapped by simply seeding the second probe beam along the identical path as the conjugate beam from the first seed. In either case, sub-shot-noise absorption imaging should be possible. For example, we can put an object into the path of the probe beam, and use a CCD camera to measure the noise difference between the twin beams.

Such imaging would be straightforward for broadband absorptive or opaque objects, and even for refractive objects that are far enough off-resonant that the frequency difference (6 GHz in our case) between the probe and conjugate beams is unimportant. On the other hand, one feature of the 4WM generation scheme that is attractive for scientific applications is that it produces narrowband light that can, for example, be used for coupling to cold atoms. In the present configuration the beams are composed of two pairs of non-degenerate, narrowband, multi-spatial-mode twin-beams. In spite of the dual-frequency nature of the beams, they can be adapted to imaging applications, even for narrowband absorbers. One could, as described above, overlap these beams, but then only approximately half of the light would interact with the atoms. Alternatively, one can separately detect the two probe beams (P1 and P2) and conjugate beams (C1 and C2) on a CCD detector, align the beams in software to match the spatial modes, and group them as follows: $C1 = P1 + C2 - P2$. This results in a single-color imaging beam (C1) that can be referenced to the remaining combination of beams that eliminates the noise on the seed beams. While any loss in the optical system will limit the ability to observe

squeezing, CCD cameras with quantum efficiencies of >95% at the Rb D1 line of 795 nm are available commercially. The consequences of the dual-seed scheme for experiments performed with homodyne detection should be relatively limited. In the case of dual-seeding a bi-chromatic local oscillator would be required [69], and the relevant noise signals should simply add.

Finally, if we pump the 4WM process near the frequencies of the probe and conjugate beams indicated above, we can generate single-mode squeezing [70], or we could generate twin beams at the same frequency that are not degenerate in direction [71]. In that case we would not have to use bi-chromatic local oscillators for homodyne detection, but we would have a phase-sensitive process where the twin seeds would have to be carefully phase-stabilized with respect to each other. The present two-mode squeezing results show that the 4WM process is not intrinsically limited at low frequencies, and imply that this sort of phase-sensitive configuration should be capable of generating single-mode squeezing at similarly low frequencies, regardless of whether or not the process is seeded.

3.5 Conclusions

Using a bright-beam 4WM scheme in warm Rb vapor we have been able to achieve intensity-difference squeezing of more than 5 dB down to frequencies below 20 Hz. Experiments that have made the most progress thus far toward quantum-correlated imaging have typically used unseeded nonlinear processes. Our work presents a means to overcome technical limitations associated with the use of a seed

for bright-beam quantum imaging. The lack of a resonator, which is susceptible to acoustic noise coupling, makes these single-pass 4WM schemes capable of generating strong squeezing at very low frequencies, and we have demonstrated this by balancing the seed noise in the detection. Our optimized 4WM scheme, with intensity balancing, an increased phase-matching angle, and the locking/frequency-narrowing of the seed laser, results in the ability to generate intensity-difference squeezing down to frequencies where we are limited by detector electronic noise or by simple beam-pointing instability. This should allow the application of squeezed light to a number of practical applications that demand low frequency measurements. It should also be useful for coupling to cold atoms or to systems such as optical memories based on electromagnetically-induced transparency [52].

Chapter 4: Two-beam Coupling in Four-wave Mixing

4.1 Introduction

Our experiments have shown that the squeezing bandwidths in a 4WM system typically extend out to about 20 MHz, the cut-off depending on the intensity and one-photon detuning of the pump laser. The low-frequency cut-off of the two-mode squeezing was in the kHz range before 2018 [55], but recent advances in obtaining low-frequency squeezing to about 10 Hz using a dual-seeding technique (balancing two seeded beams and their conjugates on the detectors) in this 4WM system, in Ref. [45] and in chapter 3 of the thesis, have now opened up the possibility of extending this technology to other applications. In this chapter we investigate the processes that degrade the squeezing below the frequencies of the order of the atomic transition linewidth, around 5.75 MHz [72].

Our observations show that the dual-seeding technique can bring along with it potential new complications that involve two-beam coupling between the seeding beams. This effect generates large amounts of excess noise as a result of fluctuations in the atomic polarization seen by one beam that are driven by a second beam, and has been previously observed [73, 74] between beams that are degenerate in frequency, near a transition resonance, and that cross in an atomic vapor. The

vacuum sidebands of one seeding beam can interact with another seeding beam in an atomic vapor cell and amplify the noise photons through two-beam coupling. This process occurs when the intensity of the seeding beam is larger than the saturation intensity of the atomic transition [74]. Another mechanism, described in Ref. [73], that can contribute to the noise of the atomic dipoles involves light at the Mollow sideband frequencies, related to the intensity of the other seeding beam, and is another 4WM process with the first seeding beam. The model given in Ref. [73] is for homogeneously broadened two-level atoms. This mechanism generates spontaneously scattered light in the spatial mode of the seeding beam. It can occur at a low power, below the saturation intensity of the atomic transition. These two mechanisms of the two-beam coupling are basically other four-wave mixing processes. We show that similar two-beam coupling can also be present in the dual-seeding situation discussed here. The addition of the pump and 4WM interaction that amplifies the fields of the seed beams enhances this coupling, to the detriment of the observed squeezing at frequencies below the atomic transition linewidth. We find that the issue can be avoided either with sufficiently low power (in both seed and the amplified probe - this was the situation in the previous chapter) or by seeding with beams that do not directly intersect in the gain medium.

The problem appears in the case of generating quantum-correlated images. To have the probe image completely covered by the gain region, we usually focus the probe image into the center of the pump beam in the Rb cell. Under these circumstances the information in the image will be distributed into all of the pixels in the Fourier plane and this will cause "cross-talk" between each pixel of the image

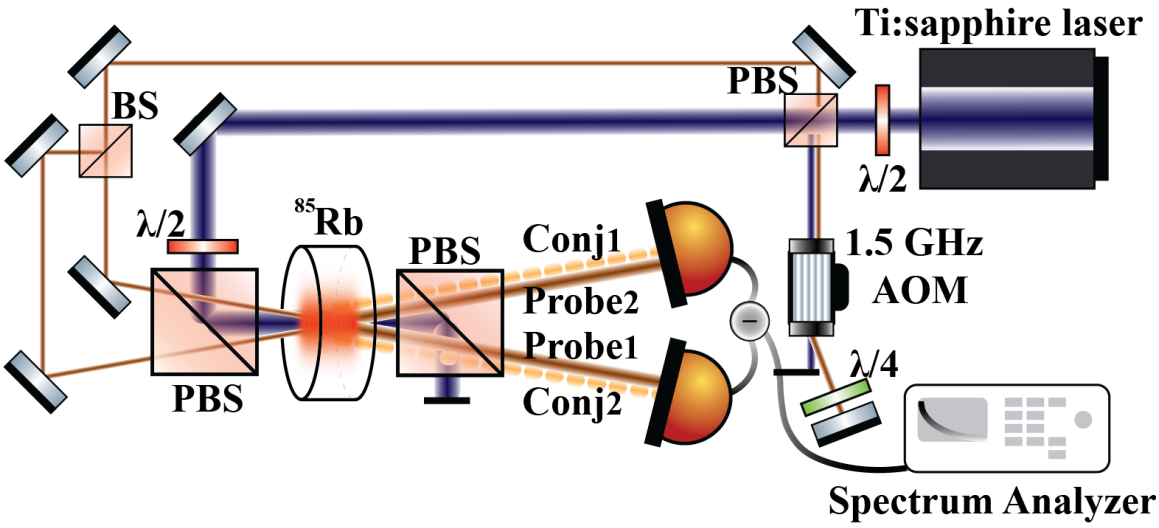

Figure 4.1: Experimental setup diagram for two-beam coupling. BS indicates a non-polarizing beamsplitter, PBS a polarizing beamsplitter. $\lambda/2$ and $\lambda/4$ are half-wave plate and quarter-wave plate.

in the 4WM process. We can eliminate this problem by imaging the seed into the 4WM gain region, that is, each pixel of image does not overlap and cross talk with the others through the atoms.

4.2 Experiments

The experimental setup that we use to demonstrate the two-beam coupling in the squeezed light (Fig. 4.1) and is almost identical to the setup for the low-frequency squeezed light. We replace the laser source by a Ti:sapphire laser because of the excess noise in the squeezed light that is generated at high frequencies from the semiconductor diode lasers. The light from the Ti:sapphire laser is sent through an optical fiber to create a pump beam of ≈ 1.5 mm $1/e^2$ diameter and 650 mW of power. This light is detuned in the range of $\Delta = 800$ MHz to 1.3 GHz to the blue

of the $S_{1/2}$ (F=2) $\rightarrow P_{1/2}$ (F=3) transition in ^{85}Rb. The ^{85}Rb cell is 1.2 cm long and is heated to a temperature of approximately 125 °C. A pair of seed beams at the probe frequency can be introduced on either side of the pump, at a small angle (approximately 0.3 to 0.5 degrees) to the pump beam. The probe seeds are 0.55 mm $1/e^2$ diameter beams derived directly from the Ti:sapphire laser by double-passing $\approx$ 90 mW of this light through a 1.5 GHz acousto-optic modulator, resulting in a 2-photon detuning of $\delta = -2$ MHz for the 4WM process.

There are two other setups in Fig. 4.2 for the quantum correlated imaging. We usually have both of the pump and probe beams overlap at the position of their own beam waists so that they have less-curved wavefronts. The 4WM process has less efficiency when either probe beam or pump beam does not have a flat wavefront in the 4WM gain region because of the momentum conservation (phase-matching) requirement for the four-wave mixing. Fourier setup (Fig. 4.2 (a)), is the typical setup for the 4WM, the Gaussian probe seed beam is focused in the 4WM gain region. With this setup for the imaging experiment, the information at the center of the Rb cell will be the probe image in spatial frequency (that is the Fourier transform of the mask). That means each component of the probe seed in the gain region contains all the information of the probe image with the same spatial frequency. This causes two-beam coupling between pixels when it is reimaged. In Fig. 4.2 (b), the imaging setup, the beam diameter reducing telescope can demagnify the probe beam size and still have the probe beam fit in the center of the 4WM gain region. The most important function of the beam diameter reducing telescope is to maintain the probe image in real space in the 4WM gain region, which avoids the

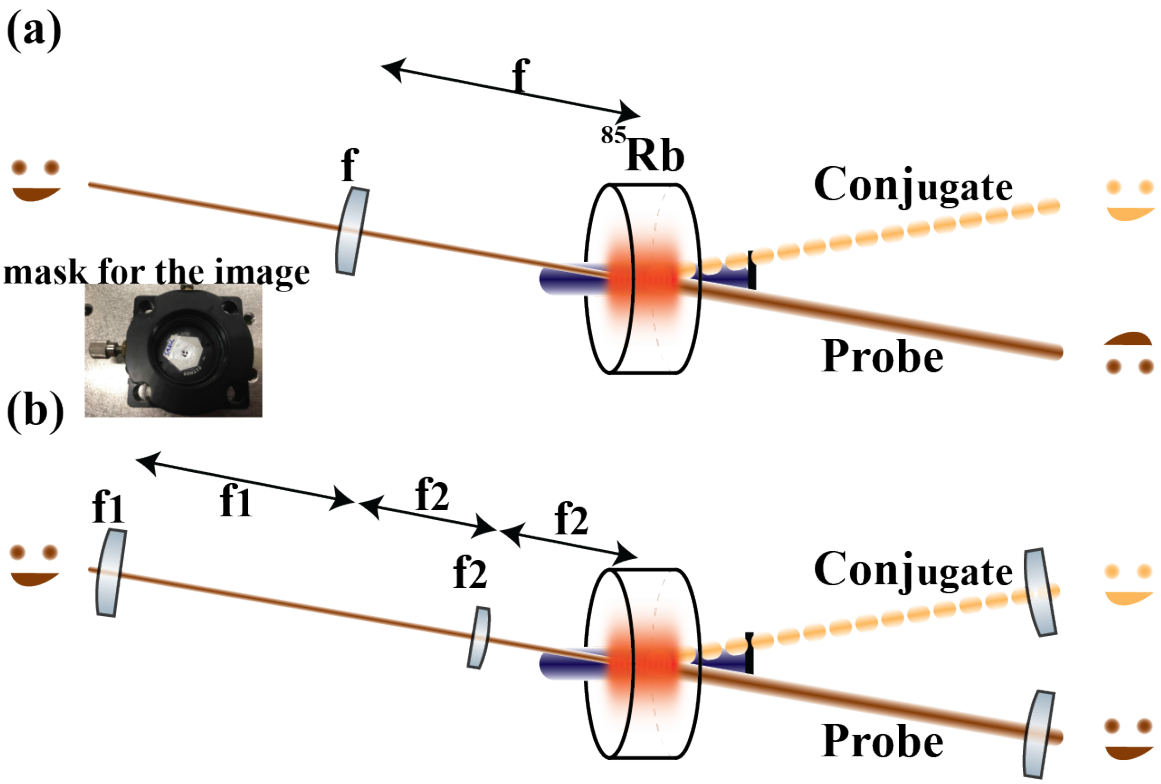

Figure 4.2: Quantum imaging setup. We send the laser beam through a "smiling" mask to generate the image seed. (a) Fourier setup. The Fourier plane of the image is focused into the 4WM gain region. Without the focusing lens the probe does not fit in the 4WM gain region. (b) "Imaging" setup. The real image of the mask is in Rb cell. We have a beam diameter reducing telescope and create a real image of the mask in the 4WM gain region. Note that there is a Kerr lensing effect due to the 4WM gain medium that needs to be considered to understand the images that are observed in the far field.

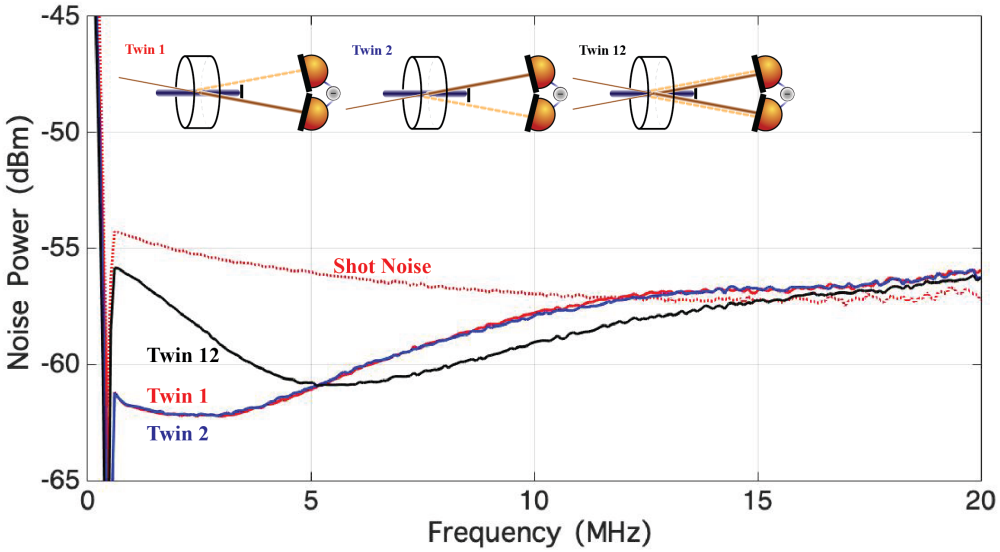

Figure 4.3: Spectrum of intensity-difference squeezing versus measurement frequency. Shown are shot noise (red dashed curve), spectra of two independent single seeded processes (red, blue curves), and dual seeded (black curve), where both of these seeds are present at half the power and crossed at the center of the pump beam in the 4WM gain region. The total output optical power for each trace is 800 μW. The 4WM gain ≈ 10 in each case (pump power = 680 mW, cell temperature = 122 °C, $\Delta = 800$ MHz, $\delta = -2$ MHz). There is a delay line for the conjugate beams in each case. The resolution bandwidth (RBW) is 300 kHz and the video bandwidth (VBW) is 100 Hz for these measurements. The detector bandwidth is 45 MHz. The electronic noise is subtracted from these traces.

two-beam coupling problem in the 4WM process.

4.3 Two-beam Coupling in Dual-seeded Four-wave Mixing

While the dual-seed technique clearly improves the squeezing at low frequencies, it also introduces new problems at low frequencies, where the squeezing is now noticeably reduced at frequencies below the atomic transition linewidth, shown in

Fig. 4.3. A similar effect has been observed in the lab in the past: introducing two bright seeds to seed 4WM with a single pump can couple the beams and affect the observed squeezing. This observation has led to the use of a completely separate pump beam to generate local oscillators (LOs) for homodyne detection in past experiments where that was required [30], ensuring the independence of the two 4WM processes.

The dual-seeding technique can be seen to markedly reduce the squeezing at frequencies below about 5 MHz in Fig. 4.3. It seems that there is a coupling between the seeded beams that degrades the squeezing in this regime. We have investigated this effect as a function of the relative beam powers, as shown in Fig. 4.4. Here we fix the power of one of the seed beams and vary the power of the second input seed, showing that the coupling between the beams increases with intensity or power.

The two-beam coupling observed here is similar to that reported by Kauranen *et al.* [74]. In those experiments two beams of the same frequency, tuned near an atomic resonance, cross in a vapor cell and exchange energy, resulting in enhanced fluctuations in the output intensity of each beam. The excess noise in those experiments was explained in terms of a 4WM interaction in a 2-level atom model [73]. The model allowed for two noise mechanisms. The first is amplification of vacuum fluctuations in the frequency sidebands of one beam, due to a 4WM interaction with the other beam (a stronger "pump" beam in their case). In this case the amplified sidebands beating against the carrier of the injected beam produces a beam that is much noisier than the shot-noise-limited input at low frequencies. A second mechanism proposed by these authors is the spontaneous scattering of light resulting

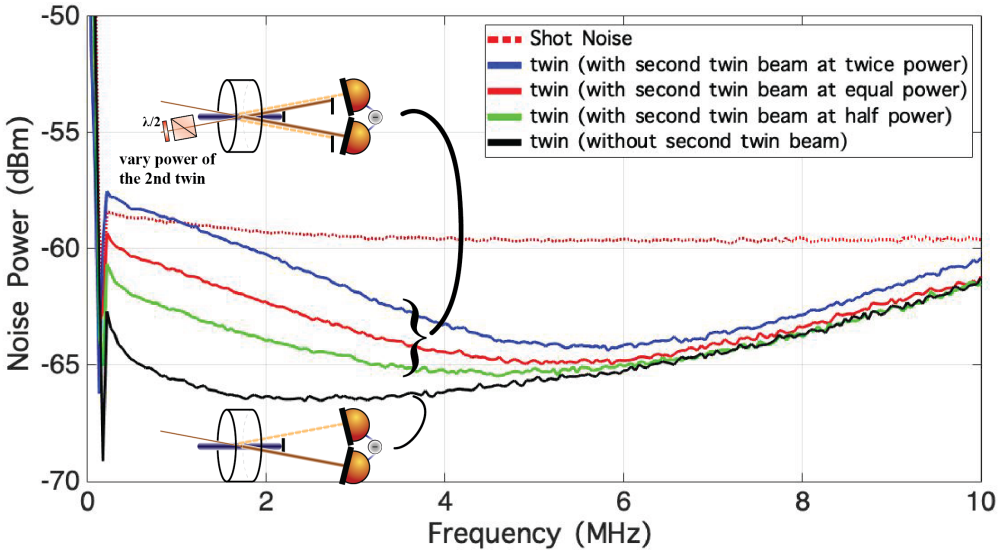

Figure 4.4: Two-beam coupling at 3 relative powers. The plotted spectra are the shot noise measurement (red dashed curve); intensity-difference squeezing of one twin beam in the presence of a second twin beam, where the second twin beam has twice (blue curve), equal (red curve), and half power (green curve) of the measured twin beam, crossed in the 4WM gain region; intensity-difference squeezing of a single twin beam without any other twin beam crossed in the Rb cell (black curve). The total output optical power of each trace is 800 μW. The 4WM gain ≈ 7 in each case (pump power = 750 mW, cell temperature = 120 °C, $\Delta = 800$ MHz, $\delta = -2$ MHz). There is a delay line for the conjugate beams in each case. The resolution bandwidth (RBW) is 100 kHz and the video bandwidth (VBW) is 100 Hz for these measurements. The detector bandwidth is 45 MHz. The electronic noise is subtracted from these traces.

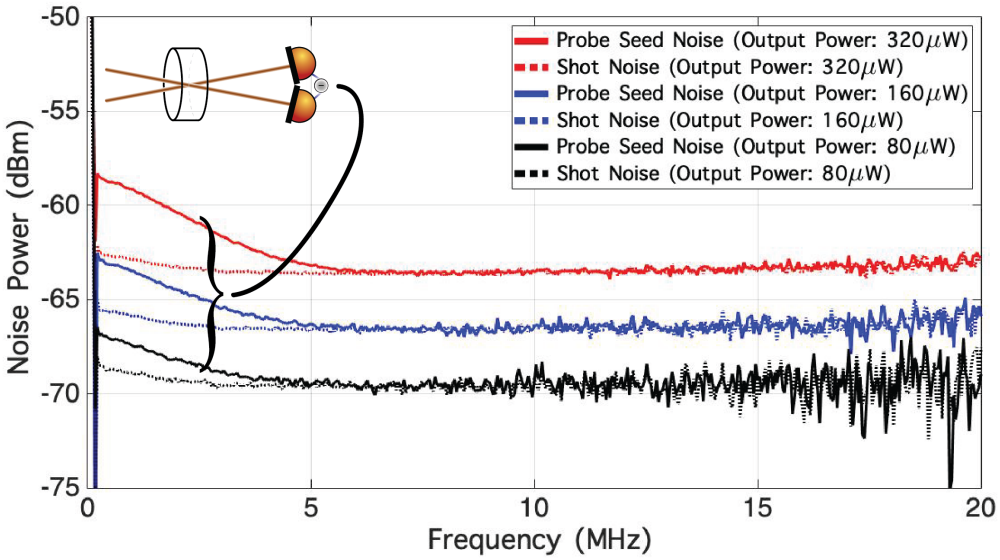

Figure 4.5: Noise spectrum of the intensity-difference of two probe seed beams, derived from the same laser beam, crossing in the Rb vapor cell and in free space. The probe seed beams are detuned $\approx$ 800 MHz to the blue of the $S_{1/2}$ (F=3) $\rightarrow P_{1/2}$ (F=3) transition in ^{85}Rb. Without the Rb vapor present the technical noise on the beams subtracts and gives a measure of the shot noise for the incident power. With the Rb vapor present the two-beam coupling causes the beams to exchange energy and increases the noise power in the intensity-difference at low frequencies. The resolution bandwidth (RBW) is 100 kHz and the video bandwidth (VBW) is 100 Hz for these measurements. The detector bandwidth is 45 MHz. The electronic noise is subtracted from these traces.

from quantum fluctuations of the atomic medium that are induced by the other beam. This mechanism, basically the absorption by the atoms of light from one beam that results in resonance fluorescence being re-emitted into the spatial modes of each beam. This light is also further amplified by a 4WM interaction. The first mechanism is only expected to occur when the light intensity is comparable to the saturation intensity of the transition and the latter mechanism was determined to be the dominant one in [74]. In the present case the intensity of each of the two degenerate beams is generally well below the saturation intensity of the Rb atomic transition, discriminating against the first mechanism. The fact that the coupling is restricted to frequencies at or below the natural linewidth of the atomic transition (the linewidth of the $P_{1/2}$ state in Rb is $\approx$ 5.75 MHz) as observed in Fig. 4.5 is consistent with this interpretation.

The two-beam coupling mechanism occurs with or without the pump beam present and is a 4WM coupling between the degenerate probe beams, mediated by the atomic vapor. This is illustrated in Fig. 4.5 where the two probe seed beams, which are 800 MHz blue of the transition from the higher ground state ($F_g = 3$) to the excited state, are intersected in free space (to determine the shot noise level) and in a Rb cell, with no pump present, at a series of increasing powers. The two-beam coupling effect is a nonlinear process that depends on the intensity of the seed. The excess noise appears over the same frequency range as in Fig. 4.4 where the pump is present, and the amount of excess noise increases with power. This behavior is again consistent with the two-beam coupling explanation given above. However, the two-beam coupling effect does not happen when the degenerate beams are far off

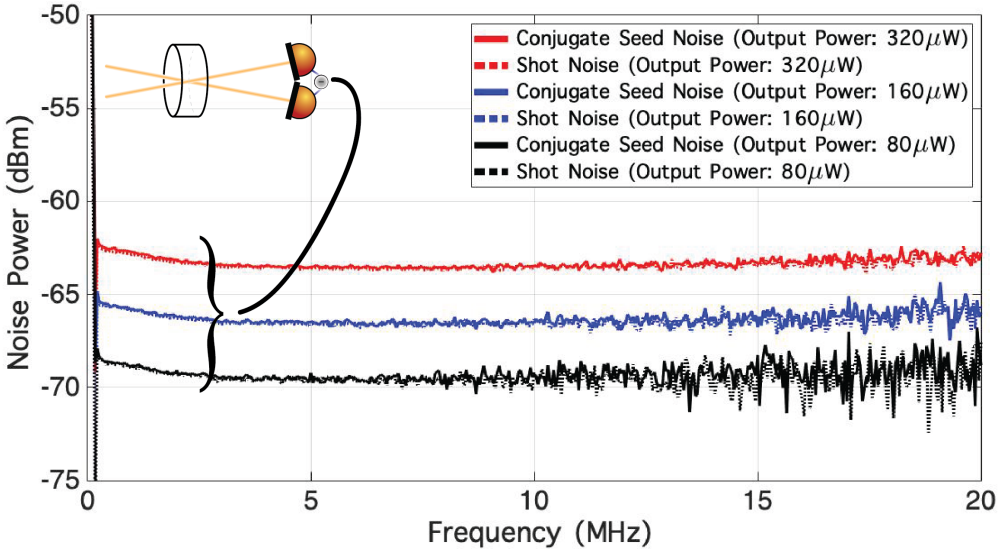

Figure 4.6: Noise spectrum of the intensity-difference of two seed beams at the conjugate frequency crossing in the Rb vapor cell and in free space. The seed beams are $\approx$ 4 GHz to the blue of the $S_{1/2}$ (F=2) $\rightarrow P_{1/2}$ (F=3) transition in ^{85}Rb. Without the Rb vapor present the technical noise on the beams subtracts and gives a measure of the shot noise for the incident power. With the Rb vapor present the noise from the two-beam coupling is still not obvious when the seed beams are far off resonance. The resolution bandwidth (RBW) is 100 kHz and the video bandwidth (VBW) is 100 Hz for these measurements. The detector bandwidth is 45 MHz. The electronic noise is subtracted from these traces.

resonance. For example, in Fig. 4.6 we do not see the excess noise when the seed beams are at the conjugate frequency, which is ≈ 4 GHz blue of the transition from the lower ground state ($F_g = 2$) to the excited state.

The work in [74] was carried out before the current generation of experiments in which strong squeezing was observed using atomic systems such as those used here, and it is interesting to note that these authors state, "We believe that this mechanism can be important in preventing the reduction of noise below the quantum-noise limit in experiments that utilize atomic vapors." We can see here that these concerns were perhaps more sweeping than justified, at least for non-degenerate 4WM processes such as that employed in the present work, where strong squeezing can be obtained. It is, however, clearly a prescient concern in terms of the coupling of 4WM processes in a multi-spatial-mode (imaging) system. It is also unclear whether the 4WM process in which degenerate-frequency twin beams are generated (essentially swapping the roles of the pump and the probe and conjugate frequencies used here) would also suffer from this two-beam coupling noise [71].

The two-beam coupling was not observed, for instance, in Ref. [45] or chapter 3 of the thesis, where very low seed intensities were used, so that the coupling, even at the output, was never very large. The two-beam coupling effect only happens when the two seed beams interact with the same atoms. An obvious way to keep the two probe beams from interacting is to send the two probe beams through the gain medium as skew rays, without intersecting each other. In that way independent groups of atoms contribute to the two 4WM processes and this coupling mechanism should be eliminated. Figures 4.3 and 4.7 show the results of this comparison.

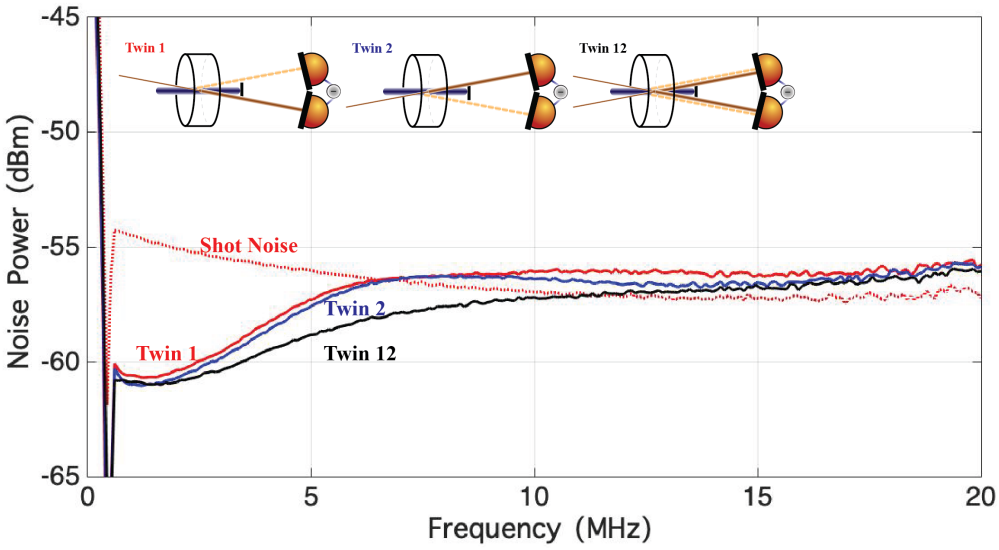

Figure 4.7: Spectrum of intensity-difference squeezing versus measurement frequency with skew rays. The red dashed curve is the spectrum of the shot noise. The blue and red curves are the spectra of two independent single-seeded 4WM processes and the black curve is for dual seeding, where both of these seeds are present at half the power in the 4WM gain region. The two probe beams are offset from the center of the pump beam in opposite directions. The total output optical power for each trace is 800 μW. The 4WM gain ≈ 10 in each case (pump power = 680 mW, cell temperature = 122 °C, $\Delta = 800$ MHz, $\delta = -2$ MHz). There is a delay line for the conjugate beams in each case. The resolution bandwidth (RBW) is 300 kHz and the video bandwidth (VBW) is 100 Hz for these measurements. The detector bandwidth is 45 MHz. The electronic noise is subtracted from these traces.

Figure 4.3 shows the spectra of the two independent 4WM processes (red and blue curves), as well as the simultaneous dual-seed process (black curve) with intersecting beams that displays a large degradation in the squeezing at frequencies below about 5 MHz. Figure 4.7 shows spectra taken under very similar conditions except that the beams have been moved so that the seed beams do not intersect. In this case the simultaneous dual-seeded process shows improved squeezing at frequencies below 5 MHz compared to both single-seeded and dual-intersecting-seeded 4WM processes.

The gain bandwidth of the 4WM is partially determined by the pump power. Figure 4.7 shows that the squeezing with the dual-seeding technique only extends to 10 MHz, which is less than the squeezing bandwidth of 15 MHz in Fig. 4.3. In the dual-seeded 4WM with skew rays the probe seed beams are not at the center of the pump beam in the 4WM gain region, therefore, the 4WM bandwidth is smaller due to the weaker pump power in the 4WM process. At the measurement frequency of 6 MHz, where the two-beam coupling effect is not present, the skew rays scheme in Fig. 4.7 has 2 dB less squeezing than the squeezing in Fig. 4.3 with the probe beams at the center of the pump. The problems of smaller 4WM bandwidth and less squeezing can be avoided by making the pump beam size larger or having flat-top beam-shaping optics for the pump.

4.4 Two-beam Coupling in Quantum Imaging

The low-frequency two-beam coupling mechanism discussed above can be avoided for the simple case of two "beams" that need to be independent. This

could include, for instance, the generation of local oscillator beams for homodyne detection, which need to be independent of the entangled signal beams used in many experiments. While the beam distortions from the Kerr lensing due to the pump beams could be difficult to match if the signal and local oscillator beams pass through different parts of the pump region, this could perhaps be fixed with a flat-top intensity profile for the pump. Unfortunately, this two-beam coupling has significant negative implications for imaging applications, as it is a mechanism for cross-talk between the pixels in an imaging field. If a masked or greyscale image is used to seed a 4WM process (such as in [30, 75, 76]), the seed image is typically focused into the gain medium and re-imaged after emerging, like Fig. 4.2 (a). If two distinct spatial modes (pixels) that are part of an input image are bright they will then necessarily overlap within the gain medium and experience coupling to the extent that the spatial Fourier transform overlaps them. The coupling can be avoided to some degree by imaging the seed pattern into the gain medium, shown in Fig. 4.2 (b), so that the spatial modes largely do not cross and couple in the gain medium.

The "whole beam" measurements in references [30, 75, 76] did not show this effect – that is, if you seed multiple spatial modes (or completely separate beams) but integrate over these beams, the loss of correlations between individual pixels is not apparent. In that case, while two-beam coupling causes, say, two beams or spatial modes at the probe frequency to exchange energy, the correlations are preserved if we integrate over both beams on a single detector. The correlated photons are not lost, they are just moved into another spatial mode, and in that

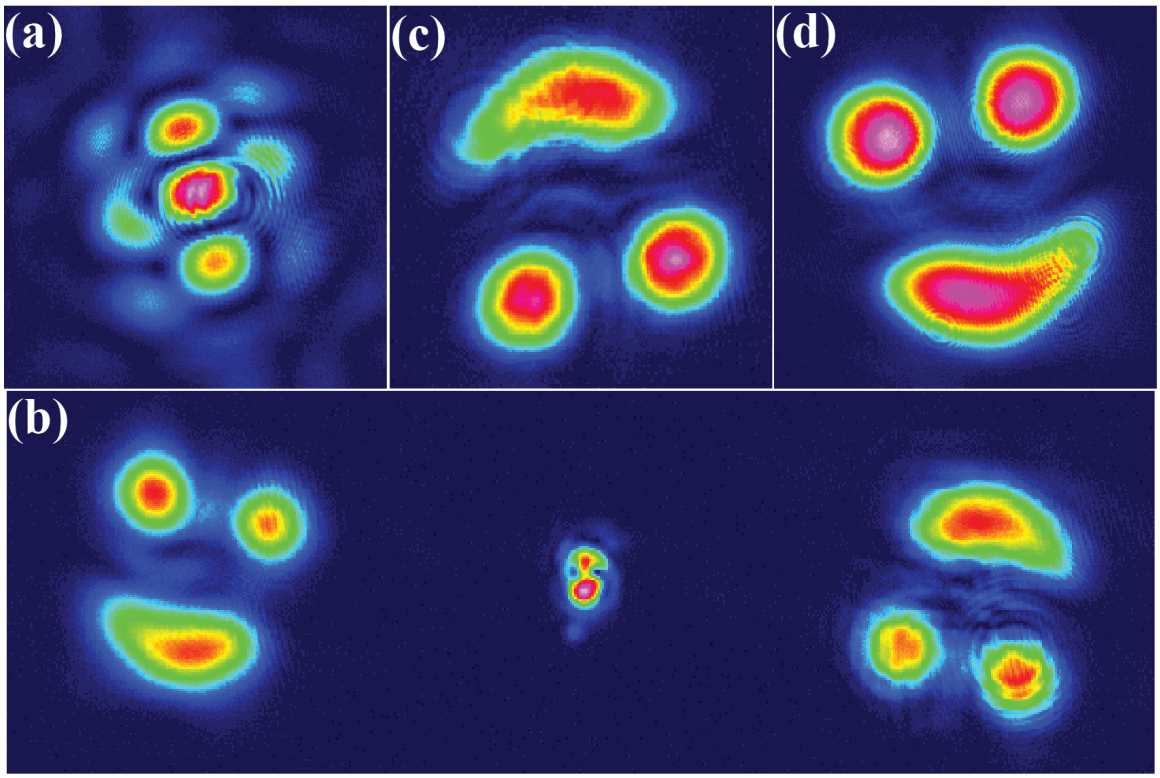

Figure 4.8: Images in the Fourier setup. (a) The transform of the smiley face in k-space at the 4WM gain region. The pump beam size is 1.55 mm $1/e^2$ diameter and the main area of the smiley face in k-space is half of the diameter of the pump. (b) Image of the conjugate (left) and the probe (right) in the far field. The middle spot is the depolarized pump light. (c) The re-imaged probe and (d) the re-imaged conjugate. There is a polarizing beamsplitter before the vapor cell. With a wave plate we can redirect the image to take a picture at the equivalent distance to the cell position.

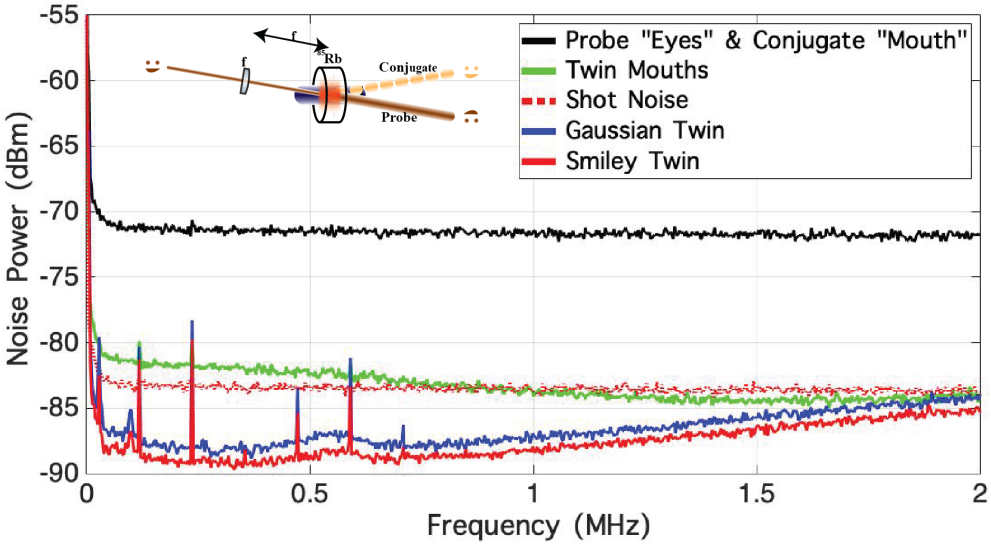

Figure 4.9: Squeezing spectrum obtained using the Fourier setup shown in Fig. 4.2 (a). The pump beam is at a one-photon detuning of 1.3 GHz, the gain is ≈ 6, and no delay lines are inserted in any of the beams for these measurements. The two-photon detuning is kept at -2 MHz and the pump power is 650 mW. The total output power for each trace is $\approx 500\ \mu W$. The traces are the thermal noise of the "eyes" in the probe and "mouth" in the conjugate (black curve); intensity-difference squeezing of twin mouths (green curve); the shot noise measurement (red dashed curve); intensity-difference squeezing of Gaussian probe beam (blue curve); intensity-difference squeezing of smiley face (red curve). The size of smiley face is smaller than the Gaussian beam. The resolution bandwidth (RBW) is 1 kHz and the video bandwidth (VBW) is 100 Hz for these measurements. The detector bandwidth is 4 MHz. The electronic noise is about 20 dB below the shot noise level and is not subtracted from these traces.

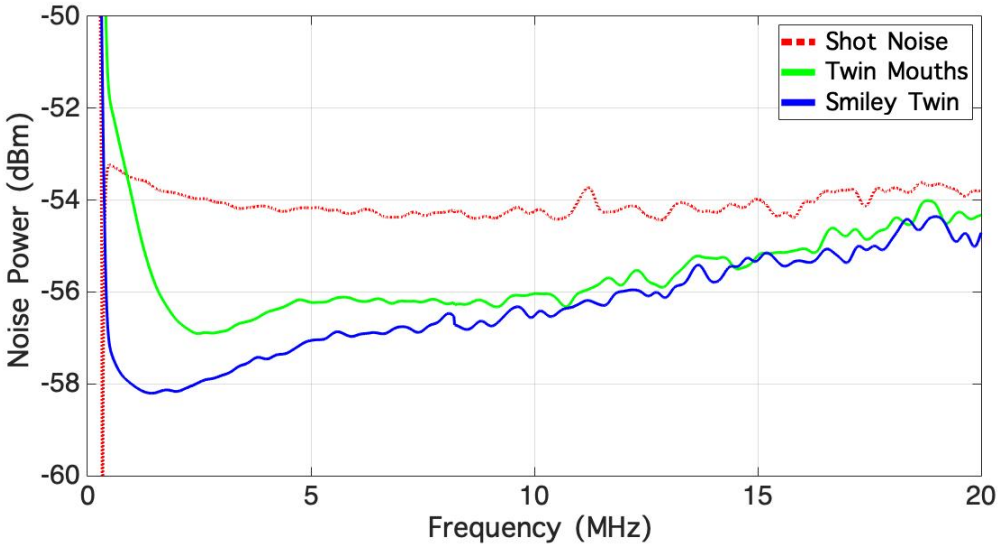

Figure 4.10: Squeezing spectrum obtained using the Fourier setup for wide 4WM bandwidth. The pump beam is at a one-photon detuning of 800 MHz, the gain is $\approx$ 6, and there is a delay line for the conjugate images in each case. The two-photon detuning is kept at -2 MHz and the pump power is 670 mW. The total output power for each trace is $\approx$ 500 μW. The traces are the shot noise measurement (red dashed curve); intensity-difference squeezing of twin mouths only (green curve); intensity-difference squeezing of the entire smiley face (red curve). The resolution bandwidth (RBW) is 300 kHz and the video bandwidth (VBW) is 100 Hz for these measurements. The detector bandwidth is 45 MHz. The electronic noise is subtracted from these traces.

case this mode is also detected. In the present case, however, we integrate over probe 1 and conjugate 2 on a single detector, and now when energy is exchanged between the two probe beams the correlations are rearranged between the two detectors and the squeezing is reduced.

Figure 4.8 shows the k-space image in the 4WM gain region, quantum correlated images in the far field, and the re-imaged outputs obtained using the Fourier setup as shown in Fig. 4.2 (a). In Fig. 4.8 (b) the conjugate image is rotated by

180° because of the momentum conservation in k-space. In the 4WM process the probe frequency is much closer to the atomic line than the conjugate. Given this smaller detuning of the probe compared to the conjugate, we expect to see stronger nonlinear effects on the probe beam. The probe image experiences a self-focusing effect that makes the focus position of the probe and conjugate slightly different in Fig. 4.8 (b). To check the two-beam coupling effect we measure the correlation between the twin images and compare it with the squeezing spectrum of the individual Gaussian twin beams. In Fig. 4.9 the squeezing spectra of the whole smiley face is similar to the squeezing with the Gaussian twin beams as expected. The low frequency technical noise in the shot noise measurement is present on the squeezing spectrum of the smiley twin (red) and the Gaussian twin (blue). However, the Fourier configuration loses squeezing between individual features (such as the eyes or mouths) of the probe and the conjugate images at low frequencies due to the two-beam coupling effect. As we know, the probe or the conjugate beam itself is a displaced thermal beam. The intensity difference noise of different parts of the probe and the conjugate images will result in thermal noise.

In order to see the whole spectrum of the two-beam coupling effect we need a wider squeezing bandwidth as shown in Fig. 4.10 using a smaller one-photon detuning, smaller phase-matching angle ($\approx 0.4°$), and a delay line in the conjugate image. The squeezing spectrum shows that the noise from the two-beam coupling effect mainly degrades the intensity-difference squeezing of the twin mouths only at frequencies below 3.5 MHz. There is still around 1 dB excess noise (twin mouth compared to twin whole face) at frequencies between 3.5 MHz and 6 MHz. Figure 4.4

shows the excess noise from two-beam coupling is larger when the power of the second beam is stronger. In the Fourier imaging setup the two-beam coupling effect is more complicated because each pixel of the image experiences a different extent of coupling in k-space. All in all, the main excess noise is still at the frequencies below 5 MHz, but the noise spectrum will not be the same as the noise from the two-beam coupling of Gaussian beams at equal power.

Figure 4.11 shows images obtained using the imaging setup of Fig. 4.2 (b). The probe image in Fig. 4.11 (a) is taken at the position of the 4WM gain region. In this case, each pixel of the image does not overlap with the others in the gain medium and this eliminates cross talk between the pixels. Because of the Kerr lensing in the vapor cell in this setup, the twin images in the far field are in the k-space shown in Fig. 4.11 (b) and this makes it difficult to separate the twin images when high spatial frequencies are present. For example in Fig. 4.12 (b), the twin images of the letters in the far field will overlap with each other and with the depolarized pump light. The high spatial frequency parts of the twin images in k-space, which include part of the correlation in the twin images, might merge into the other image when we try to separate and re-image them. We can remove the high spatial frequencies with a low-pass spatial filter to make the twin images well separated in the far field, as shown in Fig. 4.12 (d) and keep the quantum correlations between the images, but we also lose resolution in the image. With the smiley face in Fig. 4.11, which was designed to have a low spatial frequency, we are able to separate the twin images in k-space and re-image them to check the correlations. The correlations between the whole images obtained using the imaging setup shown in Fig. 4.13 give the same

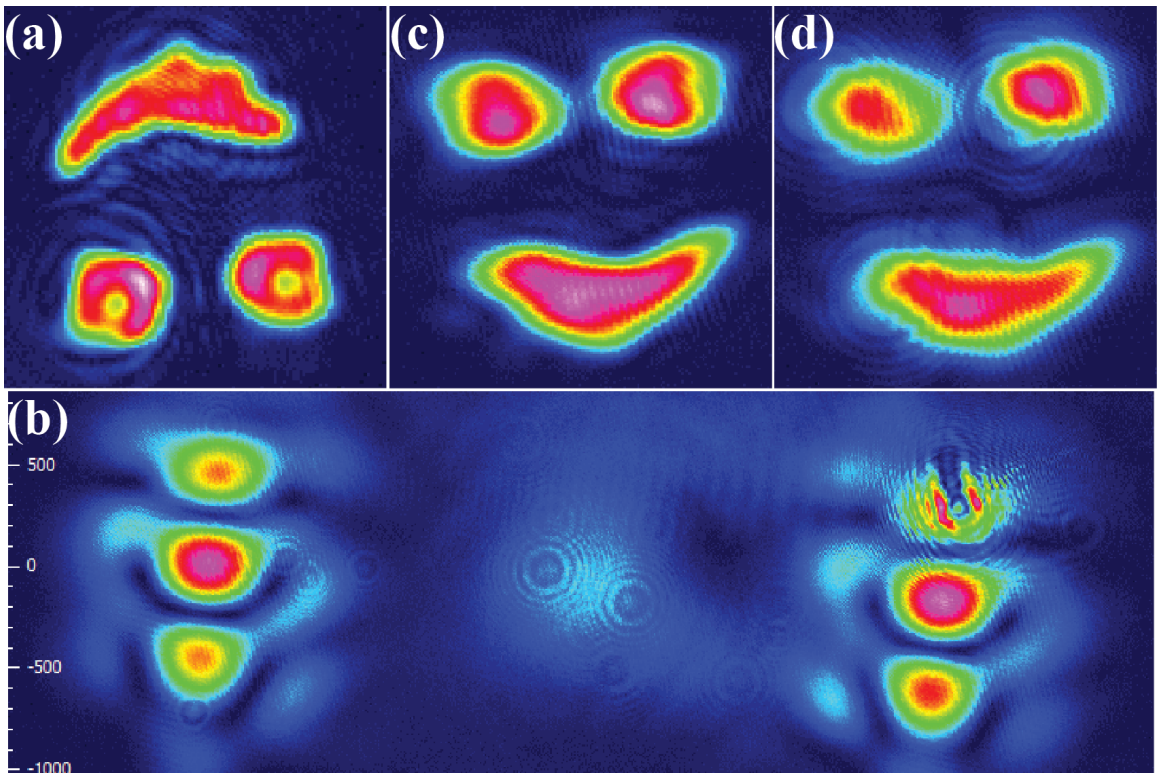

Figure 4.11: Images obtained from the imaging setup of Fig. 4.2 (b). (a) The smiley face is mapped to the 4WM gain region with a beam diameter reducing telescope. The pump beam size is 1.55 mm $1/e^2$ diameter and the size of the smiley face is around one third of the diameter of the pump. (b) Image of the conjugate (left) and the probe (right) in k-space in the far field. The middle spot is the depolarized pump light. (c) The re-imaged probe and (d) the re-imaged conjugate. There is a defect in the camera on the upper right of the image (b).

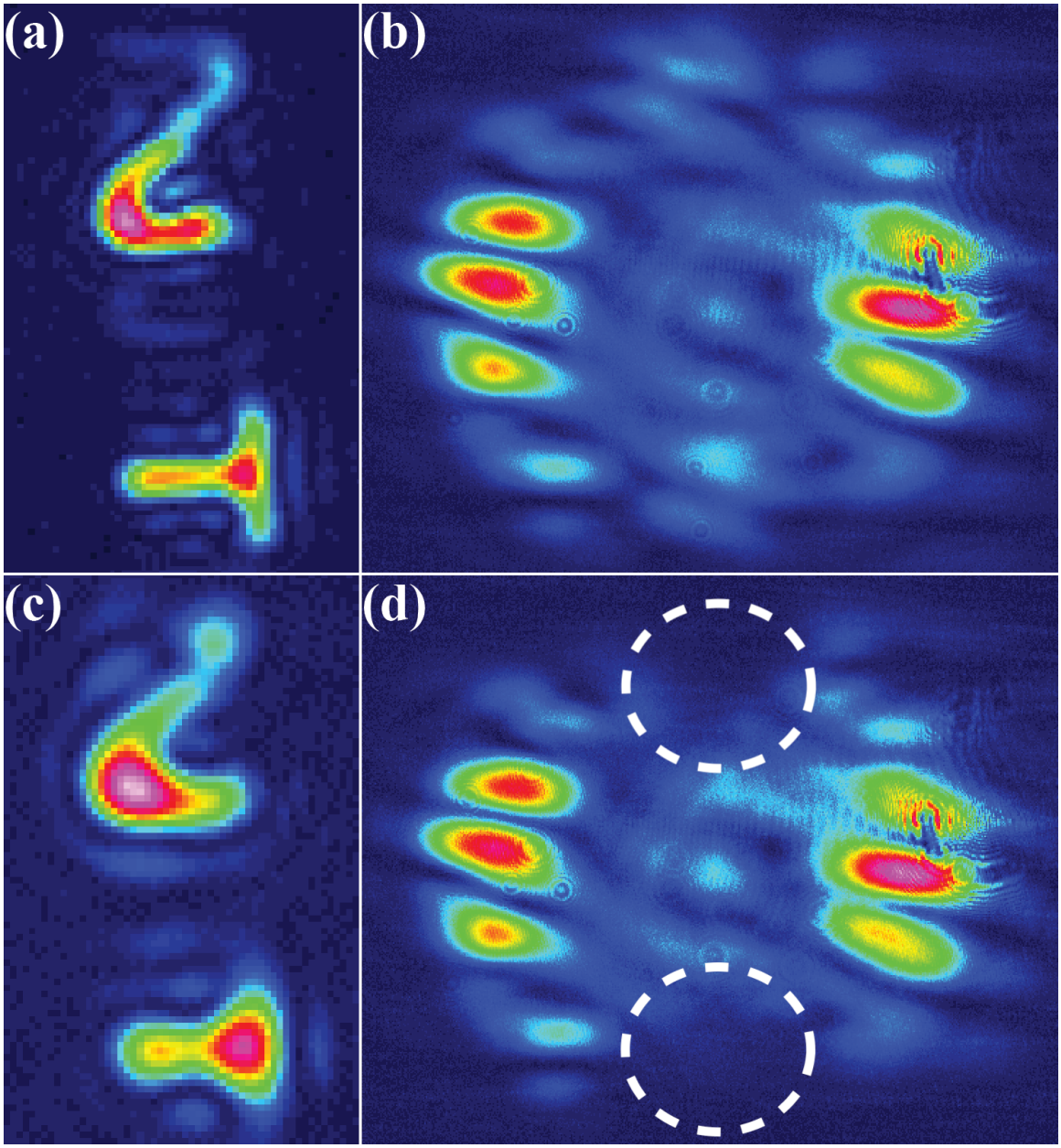

Figure 4.12: High spatial frequency images from the "imaging" setup of Fig. 4.2 (b). (a) The image of the letters N and T at the position of the Rb cell. (b) The twin images of the letters in the far field. Image of the conjugate (left) and the probe (right) in k-space in the far field. The middle spot is the depolarized pump light. (c) The image of the letters N and T filtered to have lower spatial frequency in the Rb cell. (d) The twin images of the letters with lower spatial frequency in the far field. (b) and (d) are images in spatial frequency because of the Kerr lensing effect. Note that the region of the dotted circles in (d) is darker than it is in (b).

result as the one using the Fourier setup, that is, their squeezing spectra are similar to the squeezing spectrum of the Gaussian twin beams. The imaging setup also avoids the exchange of energy between the pixels in the probe image caused by the two-beam coupling effect.

In order to get a wider squeezing spectrum for the imaging setup, we decrease the one-photon detuning to 800 MHz and the phase-matching angle to $\approx 0.4°$, and add a delay line in the conjugate image. Figure 4.14 shows that both the entire twin smiley faces and just the twin mouths have squeezing for frequencies to $\sim$10 MHz. The squeezing spectrum of the twin smiley images and the Gaussian twin beams are quite different here. The optical paths for both cases are exactly the same and we only remove the smiley mask to measure the intensity difference of the Gaussian twin beams as we did for the squeezing spectrum in Fig. 4.13. To explain the difference in the squeezing spectrum we can check the k-space twin images in the far field of the small phase-matching angle setup. The probe and conjugate images in the far field, shown in Fig. 4.15 (b), are too close to separate clearly and to re-image. The noise from the depolarized pump light and the length of the delay line for the conjugate images are not the issues that cause the degradation in the squeezing here since we still get good squeezing for the Gaussian twin beams with the same optical path. Instead, the probe and conjugate images in real space are somewhat distorted (Fig. 4.15 (c) and 4.15 (d)) because of the loss of high spatial frequency components in the separation. This leads to a reduction of squeezing for the smiley face. Compared with the squeezing obtained using the imaging setup with the large phase-matching angle, we have a different frequency extent of squeezing for the

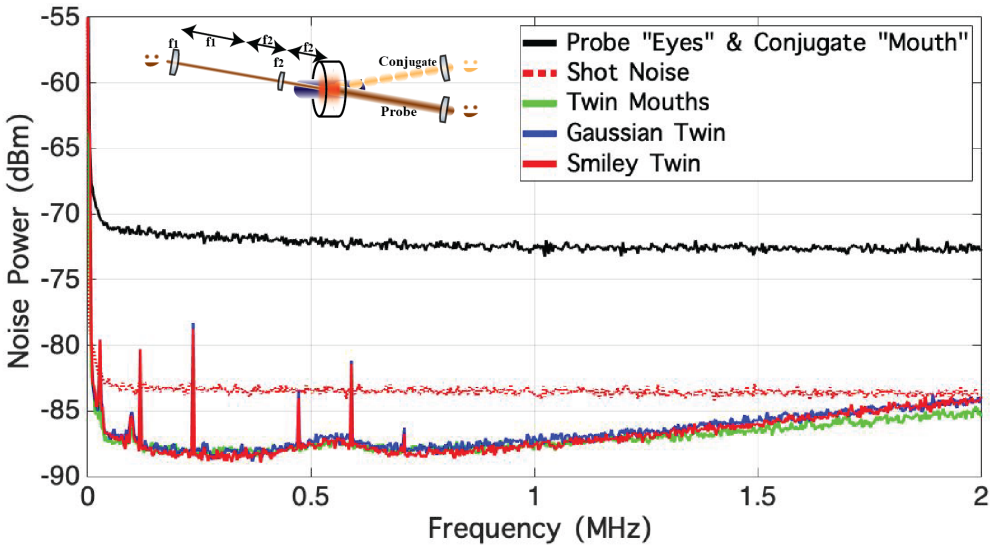

Figure 4.13: Squeezing spectrum obtained using the imaging setup as shown in Fig. 4.2 (b). The pump beam is at a one-photon detuning of 1.3 GHz, the gain is ≈ 6, and no delay lines are inserted in any of the beams for these measurements. The two-photon detuning is kept at -2 MHz and the pump power is 650 mW. The total output power for each trace is $\approx 500\ \mu W$. The traces are the thermal noise of the "eyes" in the probe and "mouth" in the conjugate (black curve); intensity-difference squeezing of twin mouths (green curve); shot noise measurement (red dashed curve); intensity-difference squeezing of Gaussian probe beam (blue curve); intensity-difference squeezing of smiley faces (red curve). The resolution bandwidth (RBW) is 1 kHz and the video bandwidth (VBW) is 100 Hz for these measurements. The detector bandwidth is 4 MHz. The electronic noise is about 20 dB below the shot noise level and is not subtracted from these traces.

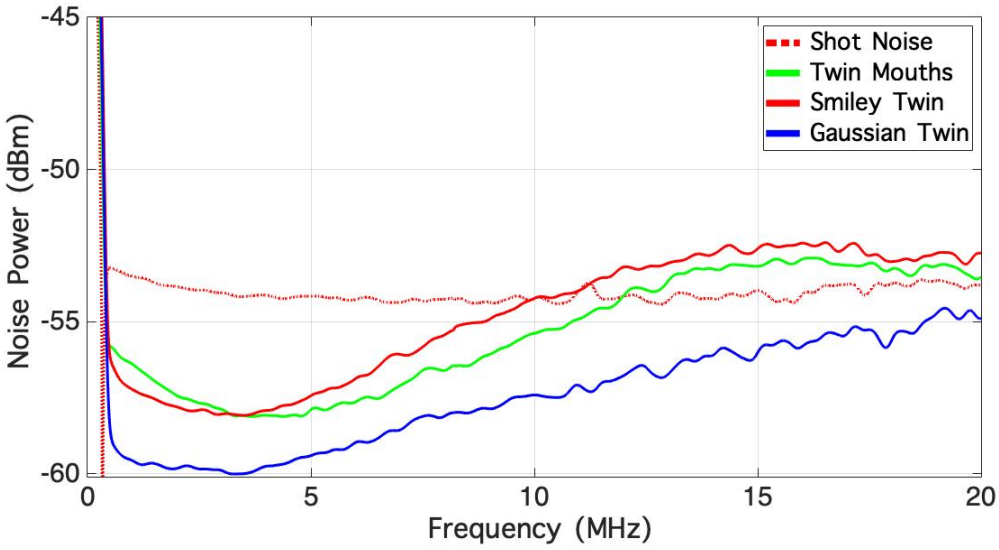

Figure 4.14: Squeezing spectrum obtained using the imaging setup of Fig. 4.2 (b) for wide 4WM bandwidth. The pump beam is at a one-photon detuning of 800 MHz, the gain is $\approx$ 7, and there is a delay line for the conjugate images in each case. The two-photon detuning is kept at -2 MHz and the pump power is 670 mW. The total output power for each trace is $\approx$ 500 μW. The traces are the shot noise measurement (red dashed curve); intensity-difference squeezing of twin mouths (green curve); intensity-difference squeezing of smiley face (red curve); intensity-difference squeezing of Gaussian probe beam (blue curve). The resolution bandwidth (RBW) is 300 kHz and the video bandwidth (VBW) is 100 Hz for these measurements. The detector bandwidth is 45 MHz. The electronic noise is subtracted from these traces.

Gaussian twin beams and for the twin images with the same optics and optical path in the small phase-matching angle setup. The distortion in the images and the loss of squeezing will be problems for direct quantum-correlated image measurements on a charge-coupled-device (CCD) camera. To avoid having to cut high spatial frequencies we can use a larger phase-matching angle, which can give better spatial resolution and intensity difference squeezing. The only disadvantage of the large phase-matching angle is the smaller 4WM bandwidth.

4.5 Discussion

The two-beam coupling mechanism is discussed above starting from the coupling between two Gaussian beams with the same frequency that causes excess noise at measurement frequencies below the atomic transition linewidth. We consider two Gaussian beams as two pixels of an image that can also have cross talk due to the two-beam coupling effect if we do not map the image to the 4WM gain region properly.

In the 4WM process we can focus a collimated Gaussian probe seed beam into the gain region as in the Fourier setup. Then we get a pair of twin beams, the probe and conjugate beams, in real space. We should see the two-beam coupling effect degrades the squeezing if the twin beams are cut to half area from opposite sides of the beams in real space. By contrast, in the imaging setup for the Gaussian twin images, instead, we expect to see each pixel of the images of the Gaussian twin beams is quantum correlated either in k-space or in real space and there should be

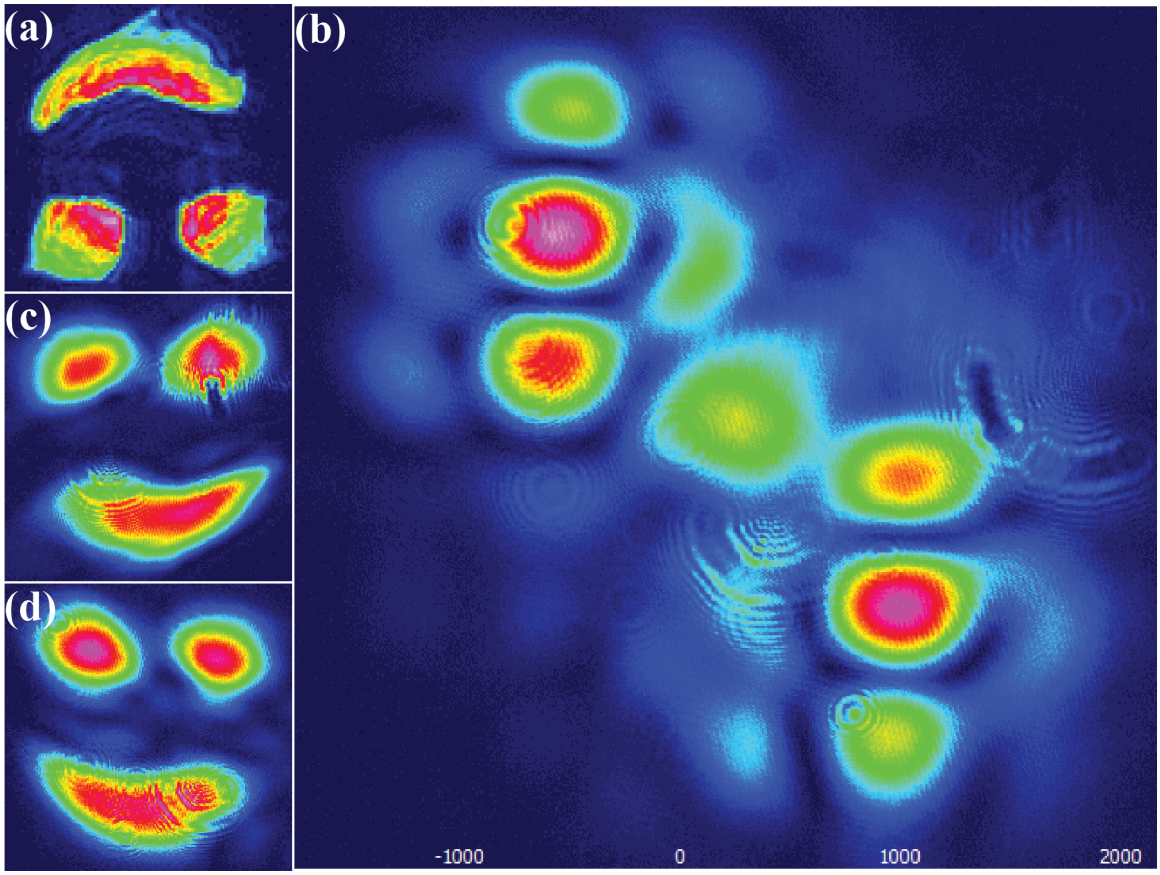

Figure 4.15: Images obtained using a small phase-matching angle in the imaging setup of Fig. 4.2 (b). (a) The smiley face is mapped to the 4WM gain region with a beam diameter reducing telescope. The pump beam size is 1.55 mm $1/e^2$ diameter and the size of the smiley face is around one third of the diameter of the pump. (b) Image of the conjugate (upper left) and the probe (lower right) in k-space in the far field. The middle spot is the depolarized pump light. (c) The re-imaged probe and (d) the re-imaged conjugate.

no degradation in squeezing. That is, we might be able to maintain a good amount of squeezing if we cut the Gaussian twin beams using the imaging setup with irises because we assume that the Gaussian beam is also a kind of a multi-spatial-mode image.

Quantum correlated images have been demonstrated using the four-wave mixing process [30] and parametric down-conversion processes [59, 60, 77]. The exposure time of the single shot in the imaging system of Ref. [60] using parametric down-conversion is 100 ms. The difficulty in their experiment is to achieve a good collection efficiency of the correlated photons and maintain the spatial resolution. In our system we can send one of the Gaussian twin beams onto an absorbing object or through a transparent mask, and measure the transmittance and the correlation.

4.6 Conclusions

We have examined dual-seeded twin-beam generation and intensity-difference squeezing in 4WM in a Rb vapor pumped by a Ti:sapphire laser source. We have identified the noise source from the two-beam coupling effect that causes excess noise in the dual-seeded 4WM process. An intensity-dependent two-beam coupling at low (< 5MHz) frequencies couples bright beams using the same atoms for gain, and would present a problem with any pump system. The low-frequency two-beam coupling can be avoided in many circumstances, such as in the case of the dual-seeding for low-frequency squeezing introduced in [45], by seeding skew rays in the gain medium.

The two-beam coupling mechanism raises concerns for imaging applications, as mixing the quantum correlations between spatial modes or image pixels could severely impact the possibility of obtaining quantum-enhanced sensitivity or resolution in such systems.

The two-beam coupling mechanism should be present in any high nonlinearity 4WM system, not limited to Rb. While we have pointed out significant noise sources for common implementations of atomic-vapor 4WM, we have also discussed techniques to avoid the added noise in a number of circumstances, and the prospects are still quite promising for using alkali-vapor-based 4WM in real applications.

Chapter 5: High-frequency Noise in Four-wave Mixing from Diode Laser Systems

5.1 Introduction

The generation of two-mode or "twin beam" squeezing from four-wave mixing (4WM) in atomic vapors has led to a number of interesting scientific results [30, 78], but also has promise for potential applications outside of the laboratory [79–81]. Sub-shot-noise correlations or entanglement between the beams generated in this system can potentially be used in random number generation [82, 83], continuous-variable quantum communication [84–86], and metrological advances [20, 21, 29, 87].

In the previous chapter we investigated the low-frequency excess noise from the two-beam coupling effect. The noise from two-beam coupling happens when two degenerate beams, near a transition resonance, cross in a Rb vapor cell. This noise can be avoided when we send the two beams through the atoms as skew rays. Here we investigate another process that degrades the squeezing at higher frequencies, on the order of the bandwidth limit of the 4WM process (the bandwidth of the 4WM process is determined by number of factors including 1-photon detuning and intensity of the pump beam). Different two-beam coupling effects in the nonlinear

medium can explain some of the results.

The fundamental differences between pump light sources for squeezed light generation have not yet been investigated. While many important advances in this 4WM system have been demonstrated using Ti:sapphire lasers as the pump source, the movement of this squeezing technology out of the laboratory would require a switch to laser systems based on diode lasers, or other more portable technologies. There have been a number of advances in this regard using semiconductor-based systems, and some problems have arisen that have been noted in the lab, but not widely reported in the literature. Amongst the problems that we have noted is that the use of diode lasers and semiconductor tapered amplifier technologies to generate the power for pumping the 4WM process produces a qualitatively different behavior in the squeezing spectrum at higher frequencies. In particular, the squeezing is lost at a much lower frequency than when the system is pumped in a similar manner with light generated by a Ti:sapphire laser, and that at frequencies above where the squeezing is lost excess noise appears, whereas the Ti:sapphire systems return to shot noise levels at higher frequencies. This bandwidth limit on the squeezing can be seen at 4 MHz in Cs [55]; at 7 MHz [63], 2.5 MHz [88], and 3 MHz [89] in Rb. For the 4WM pumped by a Ti:sapphire laser the squeezing is observed at frequencies below 20 MHz and the noise of the twin beams is around the shot noise levels at higher frequencies [90]. The squeezing bandwidth is usually smaller than 4 MHz for the 4WM pumped by the diode laser systems (the squeezing bandwidth is no bigger than the 4WM bandwidth, but maybe smaller when other noise is involved). It can extend to 7 MHz if a decent squeezing is obtained [63]. However, in contrast

to pumping with a Ti:sapphire laser the squeezing spectrum does not return to the shot noise levels at high frequencies for the diode laser systems. This excess noise was mentioned in [91], and while it was not clear that the noise source is from the diode lasers rather than the semiconductor tapered amplifier, it is believed that it comes from excess phase noise. Here we explore these effects and demonstrate that the dual-seeding technique [45] that enables very low-frequency squeezing to be obtained also allows us to recover squeezing over a similar bandwidth to that seen with Ti:sapphire technology.

The 4WM interaction generates light at two frequencies, separated by the ground state hyperfine splitting (3 GHz in ^{85}Rb) below and above the pump frequency, and indicated as the probe and conjugate, respectively. With the light source from the Ti:sapphire laser, differing group velocity delays in the Rb vapor for light near the probe and conjugate frequencies produce an apparent cut-off of the squeezing in these 4WM systems around 4-5 MHz [64,66,90]. (The phenomenon is not easily observed with the diode laser because of the diode laser excess noise.) In fact, this delay produces an oscillation in the noise spectrum that is well-known in rf engineering and has been noted in some early squeezed light investigations as well [92]. This oscillation in the squeezing spectrum can be taken out by inserting a $\approx$ 10 ns delay line into the conjugate beam path, recovering squeezing out to the typical $\approx$ 20 MHz bandwidth that is expected from the gain bandwidth of the 4WM process. The squeezing observed with the delay line correction in place goes smoothly to the shot noise level at a bandwidth that is set by the gain or pump intensity (see [54]) and typically not much mention is made of this effect. In Fig. 5.1

we display intensity-difference squeezing spectra taken using a Ti:sapphire pump laser (using a single seed for the 4WM process). Here, the intensity of each beam is digitized and the delay can be adjusted in software. Without a delay line the group velocity difference makes the squeezing appear to go away at ≈ 5 MHz, while an optimized delay of 10 ns results in a spectrum of squeezing without oscillations, that smoothly approaches shot noise at about 20 MHz, and shows no significant excess noise above the shot noise level across this range.

An interesting observation is that, while the above is true if the 4WM pump is obtained from a Ti:sapphire laser, we have found that if the pump for the 4WM process is generated using a semiconductor tapered amplifier seeded by diode lasers the introduction of a delay line cannot fully recover the squeezing. In fact, large amounts of excess noise appear in the spectra above the apparent squeezing cut-off, as shown in Fig. 5.2. To our knowledge, all published intensity-difference squeezing spectra generated using semiconductor diode and tapered-amplifier-based systems [55, 63, 88, 89] exhibit a loss of squeezing at frequencies below the natural gain bandwidth of the 4WM process and are consistent with our present observations. Here we show that this behavior is not simply due to the lack of a proper delay between the probe and conjugate beams, but is intrinsic to using the tapered amplifier seeded by a diode laser as the pump source of the 4WM.

Alkali vapor-based 4WM systems that employ semiconductor diode lasers and tapered amplifiers appear to produce squeezing out to only a few MHz. Depending on the individual system alignment and parameters, we have been able to extend this to ≈ 12 MHz by using an appropriate delay line, as shown in Fig. 5.2. The

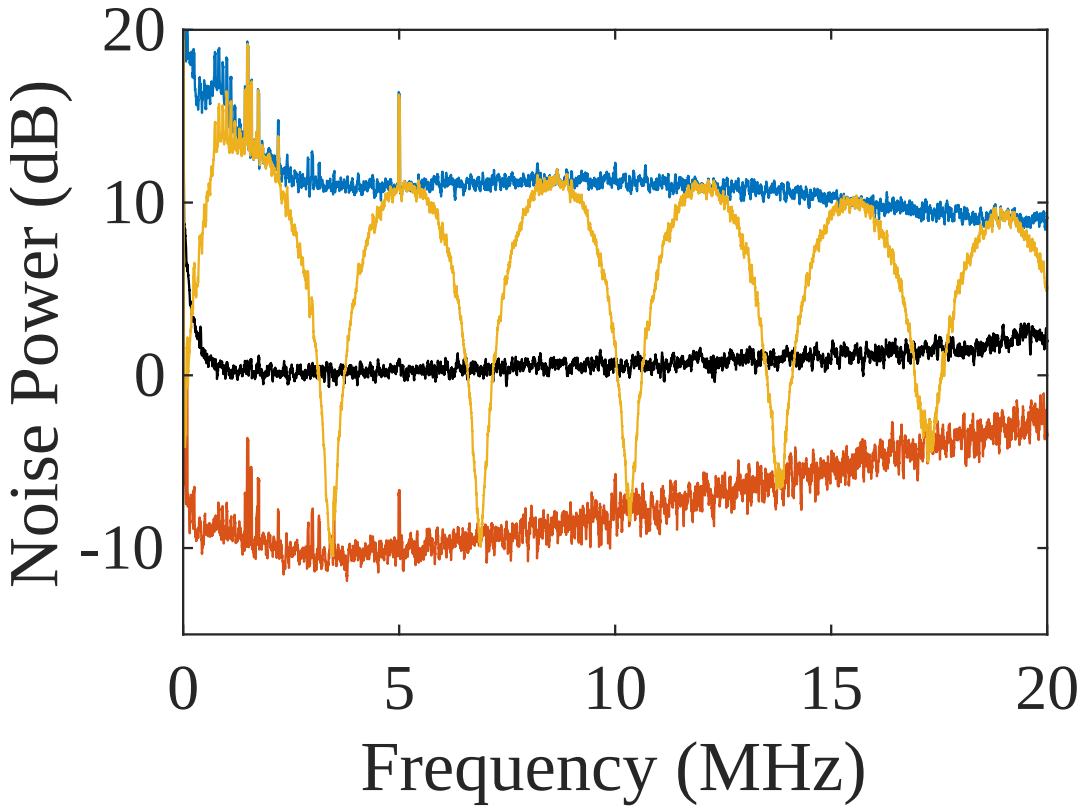

Figure 5.1: Effect of delay lines on the intensity-difference noise spectrum. Spectra obtained from 4WM using a Ti:sapphire pump laser. The intensity difference of twin beams with optimized delay on the conjugate beam (red), the noise on the intensity sum of the twin beams (blue), the shot noise (black), and the intensity difference noise with 300 ns delay time on the conjugate beam (orange).

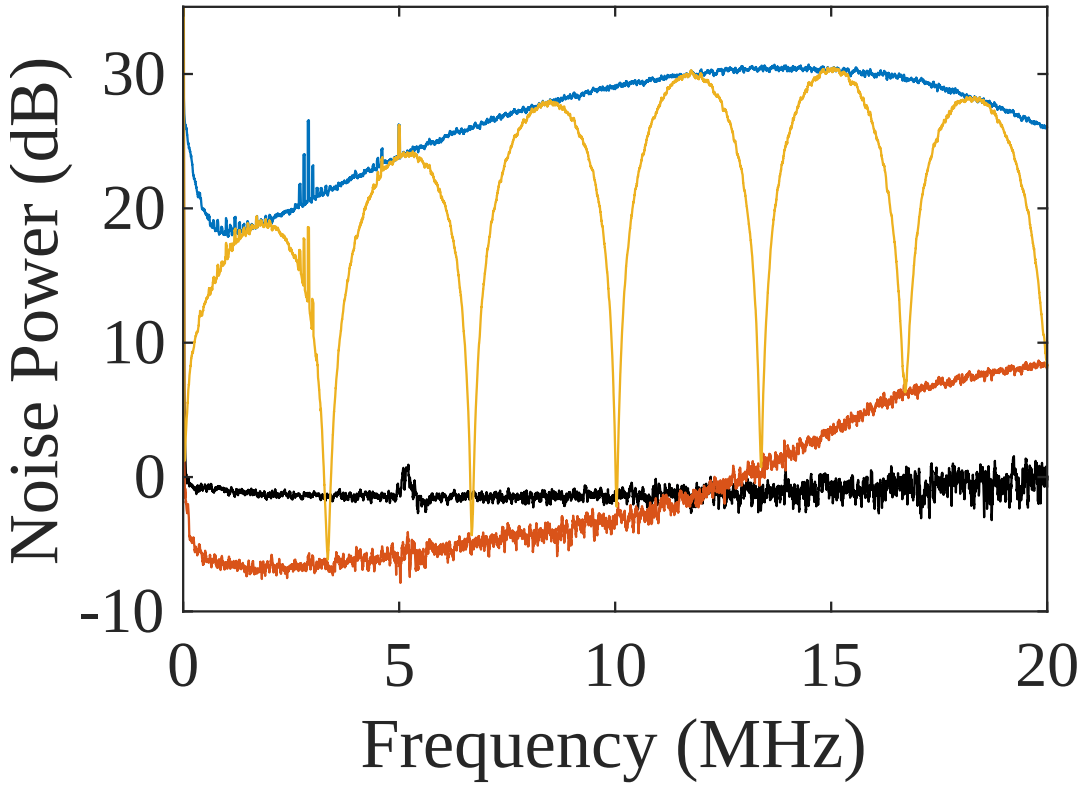

Figure 5.2: Effect of delay lines on the intensity-difference noise spectrum. Spectra obtained from 4WM using diode lasers and a tapered amplifier. The intensity difference of twin beams with optimized delay on the conjugate beam (red), the noise on the intensity sum of the twin beams (blue), the shot noise (black), and the intensity difference noise with 300 ns delay time on the conjugate beam (orange).

delay line cannot extend the squeezing out to the range of the gain bandwidth of the 4WM process, however, as in the case with the Ti:sapphire pump.

The 4WM gain bandwidth can be seen in the noise spectra of the intensity difference between two degenerate beams in Fig 5.3. In our normal setting for the 4WM, the gain bandwidth can be extended out to about 20 MHz at a one-photon detuning of 800 MHz. Here, we show the gain bandwidth is only around 10 MHz when the one-photon detuning is 1330 MHz. To make clear the fact of the gain bandwidth we reduce the gain bandwidth by increasing the 1-photon detuning and compensate the reduced gain by increasing the cell temperature. The low-frequency excess noise from the two-beam coupling effect does not appear on the dual-seeded 4WM in Fig. 5.3 since the seeding power is small and the one-photon detuning is large.

The dual-seeded 4WM process is a scheme that we recently introduced to improve low-frequency squeezing [45] (and chapter 3 of the thesis) by removing excess noise introduced by the seed laser and improving the intensity balance at DC. Two seed beams at the probe frequency are introduced in symmetric directions, so that one amplified probe beam and one conjugate beam fall on each of the two detectors. In spite of the fact we do not fully understand this noise process, we find that to a large degree this dual beam technique also can be used to remove the excess noise that exists at high frequencies in the present situation. Figure 5.3 shows at least 10 dB more noise in the single-seeded 4WM compared to the noise spectra of the dual-seeded 4WM at frequencies above 5 MHz. This excess noise even appears outside the typical gain bandwidth of the 4WM. For the excess noise within the gain

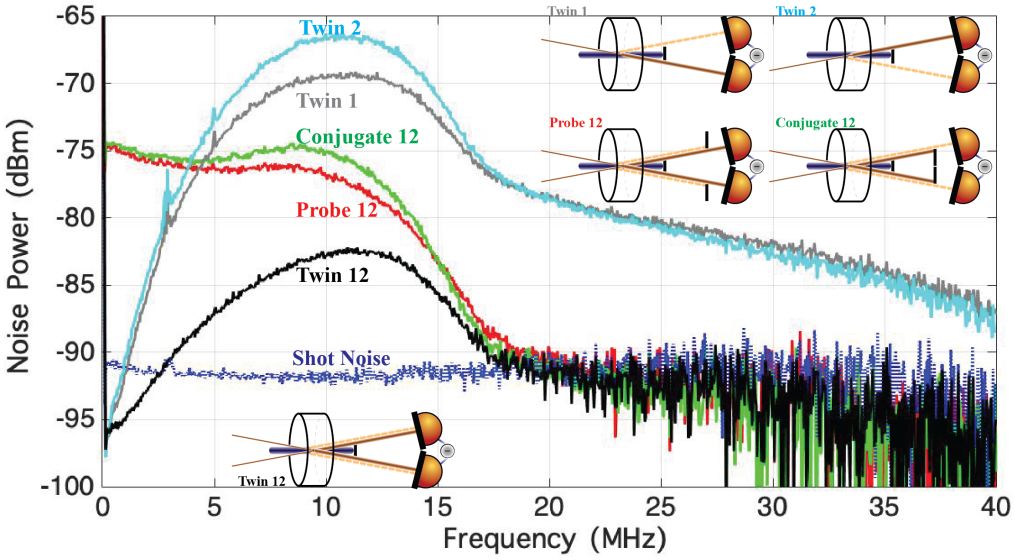

Figure 5.3: Noise spectrum of dual-seeded 4WM from a tapered amplifier seeded by a diode laser. The flat spectrum is the shot noise level (blue dashed curve). The red and green curves are the noise spectra of the difference of two degenerate beams. The cyan and grey curves are the spectra of two independent single-seeded 4WM processes (These curves are slightly different because they pass through different 4WM gain region.) and the black curve is for dual seeding, where both of these seeds are present at half the power. The total output optical power for each trace is 800 μW. The 4WM gain $\approx$ 20 in each case (pump power = 750 mW, cell temperature = 131 °C, Δ = 1330 MHz, $\delta = -2$ MHz). There is no delay line for the conjugate beams in each case. The resolution bandwidth (RBW) is 30 kHz and the video bandwidth (VBW) is 300 Hz for these measurements. The detector bandwidth is 45 MHz. The electronic noise is subtracted from these traces.

bandwidth of the 4WM we might think that the phase noise of diode lasers or the tapered amplifier causes gain fluctuations that generate the excess noise. However, the constant excess noise from a few megahertz to the frequencies outside the 4WM gain bandwidth shows that the noise is not generated through the 4WM process.

As we mentioned before the noise of the twin beams returns to the shot noise level at higher frequencies for the source derived from a Ti:sapphire laser. At frequencies above $\approx$ 20 MHz it is out of the gain bandwidth for the 4WM process and only shows shot noise if the probe seed is shot-noise-limited. From the intensity noise result (see Fig. 5.10), in the absence of Rb vapor there is no obvious difference between Ti:sapphire lasers and diode lasers at frequencies above 20 MHz. When the beam passes through Rb vapor (see Fig. 5.11) we speculate that the phase noise has been converted into intensity noise for the diode laser. We will demonstrate this excess noise with the noise test in the next section. In the 4WM process the amplified probe beam and the conjugate beam contain similar excess noise within the 4WM gain bandwidth because the twin beams are generated from the same noisy probe seed beam. The excess noise is present in the twin beams at high measurement frequencies when the 4WM gain fades away. Another way to investigate the source of this noise would be to measure the bandwidth of the high frequency excess noise with a high-speed photodetector and compare it with the phase noise measurement for the diode laser.

Figure 5.4 shows the individual spectra for the two single-seeded 4WM processes as well as the spectrum for the dual-seeded case at a one-photon detuning of 800 MHz with the pump source from the tapered amplifier pumped by diode

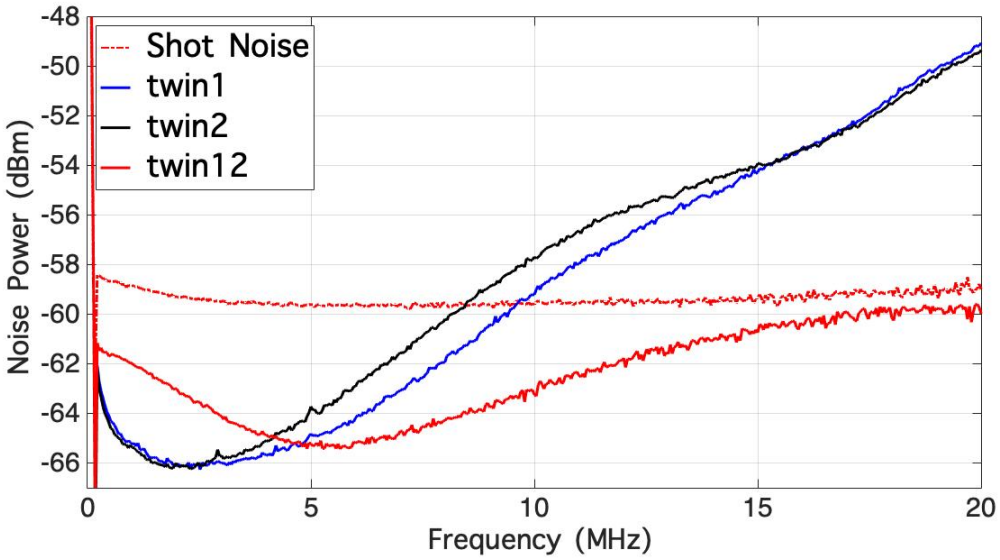

Figure 5.4: Spectrum of intensity-difference squeezing versus measurement frequency. The flat spectrum is the shot noise level (red dashed curve). The spectra of two independent single-seeded 4WM processes (blue, black) and dual seeding (crossed beams), where both of these seeds are present at half the power (red). The total output optical power of each trace is 800 μW. The 4WM gain ≈ 6 in each case (pump power = 750 mW, cell temperature = 119 °C, $\Delta = 800$ MHz, $\delta = -2$ MHz). There is a 10 ns delay line for the conjugate beams in each case. The resolution bandwidth (RBW) is 100 kHz and the video bandwidth (VBW) is 100 Hz for these measurements. The detector bandwidth is 45 MHz. The electronic noise is subtracted from these traces.

lasers. The squeezing spectrum for each single-seeded 4WM process does not converge to the shot noise level at high measurement frequencies even if we have a delay line for each conjugate beam. At this small one-photon detuning the dual-seeded 4WM shows squeezing out to 20 MHz with a $\approx$ 10 ns delay line in each conjugate beam path. Dual-seeded 4WM from the diode laser system can remove the high frequency noise and show the similar squeezing result as the single-seeded 4WM from the Ti:sapphire laser. The excess noise at measurement frequencies below the atomic transition linewidth is from the two-beam coupling effect.

We have shown the two-beam coupling effect by the comparison of crossed beams and skew beams with the dual-seeded 4WM pumped by a Ti:sapphire laser in the previous chapter. The high frequency noise is not present in the spectrum for the 4WM pumped by the Ti:sapphire laser. Fig. 5.5 and 5.6 show the similar two-beam coupling effect for the 4WM process pumped by a diode laser and a tapered amplifier. The high frequency noise is present in each single-seeded 4WM case and is removed to some extent in the dual-seeded 4WM case. The high frequency noise cannot be removed completely because each single-seeded 4WM might experience different loss and different gain if the phase-matching angles are slightly different or the optical paths of the beams are different. Each beam contains different amounts of the excess noise due to the gain difference and the loss difference. Another significant difference between squeezed noise generated by the diode laser and the Ti:sapphire laser is the noise at low frequencies. For the seeding with skew rays each single-seeded 4WM process pumped by the Ti:sapphire laser has similar squeezing as the dual-seeded 4WM at low frequencies. In Fig. 5.6 the single-seeded 4WM beams and

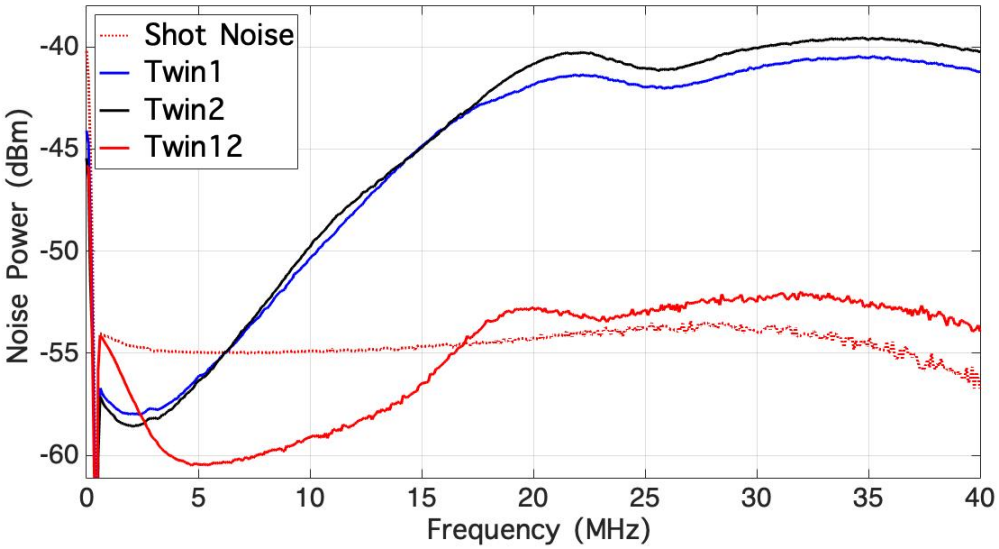

Figure 5.5: Spectrum of intensity-difference squeezing versus measurement frequency. The red dashed curve is the shot noise level. The spectra of two independent single-seeded 4WM processes (blue, black) and dual seeding (red), where both of these seeds are present at half the power and crossed at the center of the pump beam in the 4WM gain region. The total output optical power of each trace is 800 μW. The 4WM gain ≈ 5 in each case (pump power = 750 mW, cell temperature = 121 °C, $\Delta = 800$ MHz, $\delta = -2$ MHz). There is a 10 ns delay line for the conjugate beams in each case. The resolution bandwidth (RBW) is 300 kHz and the video bandwidth (VBW) is 100 Hz for these measurements. The detector bandwidth is 45 MHz. The electronic noise is subtracted from these traces.

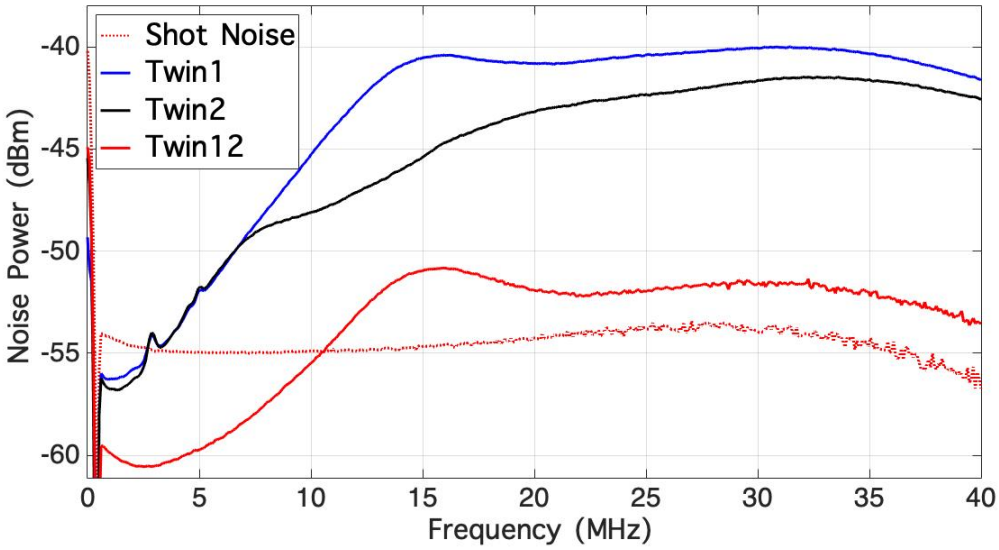

Figure 5.6: Spectrum of intensity-difference squeezing versus measurement frequency. The red dashed curve is the shot noise level. The spectra of two independent single-seeded 4WM processes (blue and black) and dual seeding (red), where both of these seeds are present at half the power and seeded by skew rays in the 4WM gain region. The total output optical power of each trace is 800 μW. The 4WM gain ≈ 5 in each case (pump power = 750 mW, cell temperature = 121 °C, $\Delta = 800$ MHz, $\delta = -2$ MHz). There is a delay line for the conjugate beams in each case. The resolution bandwidth (RBW) is 300 kHz and the video bandwidth (VBW) is 100 Hz for these measurements. The detector bandwidth is 45 MHz. The electronic noise is subtracted from these traces.

the dual-seeded 4WM beams have quite different squeezing at low frequencies when the excess noise is too high. The degree of squeezing is the result of the competition between the 4WM process and the noise from diode laser [93, 94].

The fact that the beams do not overlap in the gain medium and that we are still able to subtract-out much of the excess noise at high frequencies is surprising if the noise is dependent upon the path taken by the laser through the Rb vapor. This suggests that the noise power measured there is not really "random" noise but

a deterministic change of the correlations that is reproduced in both pairs of beams and seems to be due to the diode laser since the noise does not appear when we use a Ti:sapphire laser. This excess noise at high frequencies is somewhat dependent on the optical alignment and this fact indicates that a careful balancing of two pairs of twin beams may be able to largely remove it and allow us to recover squeezing over an extended frequency range, as seen in Fig. 5.5 and 5.6. This makes the use of tapered amplifiers as pumps potentially much more practical in a wider set of contexts.

5.2 Noise Source Test

In this section, we compare the difference of probe seed beam noise and twin beams noise, at high measurement frequencies, using three different laser sources to pump the 4WM process. The first one (Source 1) has both probe seed beams and the pump beam from a Ti:sapphire laser. The noise of Ti:sapphire lasers is quite clean when the laser is in free run status. The laser becomes noisy and its linewidth is broader when the Ti:sapphire is frequency stabilized to an external reference cavity using its internal electronics. This is because the internal electronics is optimized for stabilizing long term drifts, but makes short term noise worse. Therefore, we tried to improve the low-frequency squeezing with diode lasers because we can lock diode lasers easily. In the experiment for the low frequency squeezing the probe seed beams are from a diode laser and the pump beam is from the tapered amplifier seeded by a diode laser (Source 2). However, the 4WM with the pump from a diode

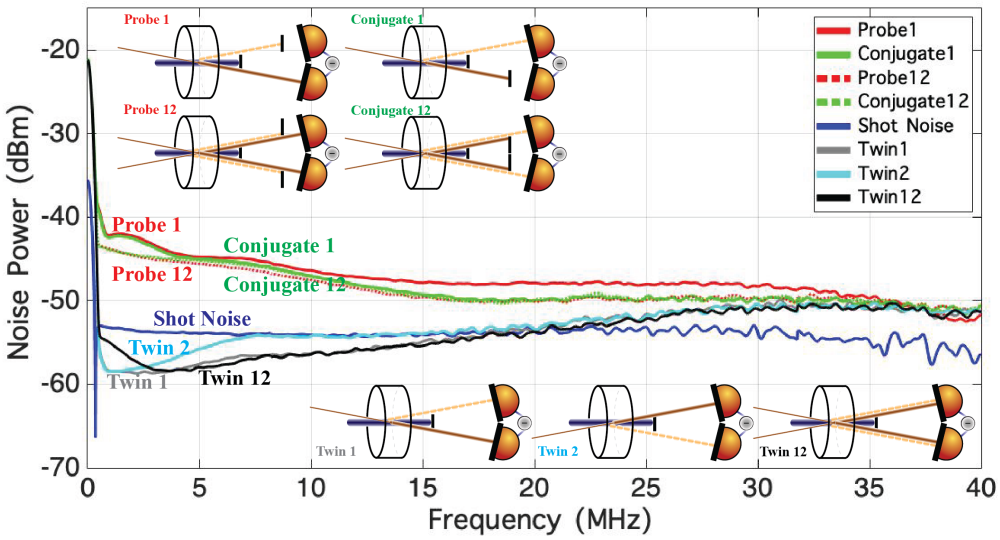

Figure 5.7: Noise spectrum of the amplified probe beam, the conjugate beam, and twin beams versus measurement frequency with light source 1 (Ti:sapphire laser). The blue curve is the measured shot noise level. The spectra of two independent single-seeded 4WM processes (grey and cyan) and dual seeding (black), where both of these seeds are present at half the power; the spectra of the amplified probe beam and the conjugate beam (red and green), respectively; the spectra of the amplified probe beams and the conjugate beams from the dual-seeded 4WM (red dashed curve and green dashed curve). The total output optical power of each trace is 500 μW. The 4WM gain ≈ 5 in each case (pump power = 680 mW, cell temperature = 122 °C, $\Delta = 800$ MHz, $\delta = -2$ MHz). There is a delay line for the conjugate beams in each case. The resolution bandwidth (RBW) is 300 kHz and the video bandwidth (VBW) is 100 Hz for these measurements. The detector bandwidth is 45 MHz. The electronic noise is subtracted from these traces. Note that while both probe and conjugate are incident on the same diode, their paths do not overlap so it is possible to separate them out.

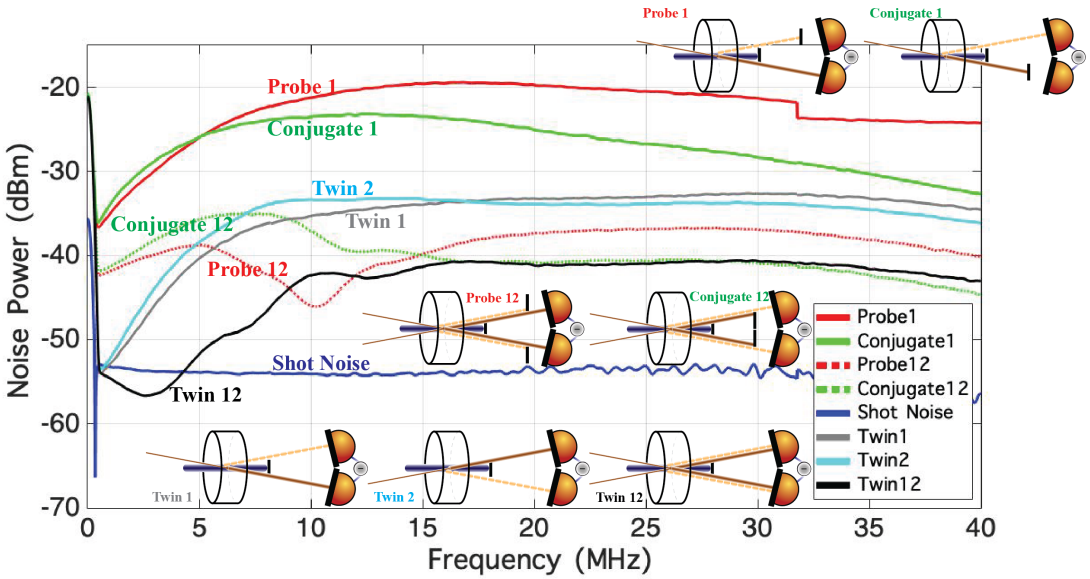

Figure 5.8: Noise spectrum of the amplified probe beam, the conjugate beam, and twin beams versus measurement frequency with the light source 2 (a diode laser and a tapered amplifier). The conditions of the 4WM process are the same as the 4WM with the light source 1 in Fig. 5.7.

laser and a tapered amplifier will introduce high frequency noise. It is not clear whether the diode laser is the noise source or the tapered amplifier. We have the third setup with probe seed beams from a Ti:sapphire laser and the pump beam from the tapered amplifier seeded by the Ti:sapphire laser (Source 3).

The amplified probe beam or the conjugate beam of the single-seeded 4WM have similar noise spectra to the amplified probe beams or the conjugate beams of the dual-seeded 4WM for the light source 1 in Fig. 5.7. The dual-seeded 4WM generates two pairs of twin beams, the amplified probe beam 1, the conjugate beam 1, the amplified probe beam 2, and the conjugate beam 2. The noise difference between two amplified probe beams, or two conjugate beams, from the dual-seeded 4WM

shows thermal noise at frequencies below the gain bandwidth. Most of the excess noise, which includes both technical noise and unknown noise, from the probe seed beams will be cancelled out in the noise difference of the pair of probe beams or the pair of conjugate beams. As we expected, the noise of the amplified probe beam, or the conjugate beam, from the single-seeded 4WM process pumped by light source 1 show similar thermal noise profiles at frequencies below the gain bandwidth.

For the 4WM process pumped by the light source 2, the noise spectra (Fig. 5.8) looks totally different from the noise spectra in Fig. 5.7. The difference between Figs. 5.7 and 5.8 is important for this discussion. The spectrum of squeezing in Fig. 5.8 is also different from the spectra in Figs. 5.4 and 5.5, even though they are all from light source 2. We can keep the one-photon detuning fixed from the diode laser with different settings for the current control and piezo control. With this detuning fixed, as expected the shot noise looks the same for different current and piezo settings, but the squeezing spectra can be totally different. This difference might come from the phase noise of the diode laser at different current settings.

Another noise source from the tapered amplifier could contribute to the phase noise in diode laser systems. There are two optical isolators after the diode laser to prevent the feedback from the tapered amplifier. The amplitude of the light beam with phase noise from the diode laser can be amplified by the tapered amplifier and, in spite of the optical isolators, sent back to the diode laser. This feedback process makes both the pump beam and the probe seed beams noisy. The squeezing spectrum becomes noisy for certain seeding alignments into the tapered amplifier when the phase noise of the diode laser is amplified through the feedback from the

tapered amplifier.

Fig. 5.8 shows ≈ 10 dB of excess noise in the single-seeded 4WM process (twin1 or twin2 compared to twin12). Comparing the single-seeded (probe1) noise and dual-seeded (probe12) noise, suggests that this excess diode laser noise, from the phase noise of diode laser systems, is appearing in the single-seeded probe beam and its conjugate beam. Not only did the probe seed beams contribute phase noise to the twin beams, but the pump beam noise also causes gain fluctuations in the thermal beams and distorts the gain profile of the 4WM. The intensity difference noise of two amplified probe beams, or two conjugate beams, is not as flat as the 4WM gain profile (reflected in the noise spectra of probe12 or conjugate12) of light source 1 in Fig. 5.7. The overall squeezing spectrum of the dual-seeded 4WM displays the squeezed noise with the excess noise from the phase noise of the probe beams and the gain fluctuations due to the pump noise.

The dual-seeded 4WM from light source 1 and source 3 show the same noise spectra, in Figs. 5.7 and 5.9. For these three light sources the light for both the probe seed beams and the pump beam are all sent through fibers. We can switch the light source between each source in a few minutes without changing the alignments, which might change the noise property, for the 4WM. From the intensity difference noise of two amplified probe beams, or two conjugate beams, the gain profile (reflected in the noise spectra of probe12 or conjugate12) in Fig. 5.9 is quite smooth like the gain profile in Fig. 5.7. This demonstrates that the pump beam source from the tapered amplifier seeded by the Ti:sapphire laser is quite stable like the pump beam from the Ti:sapphire laser directly. However, the feedback of the tapered amplifier

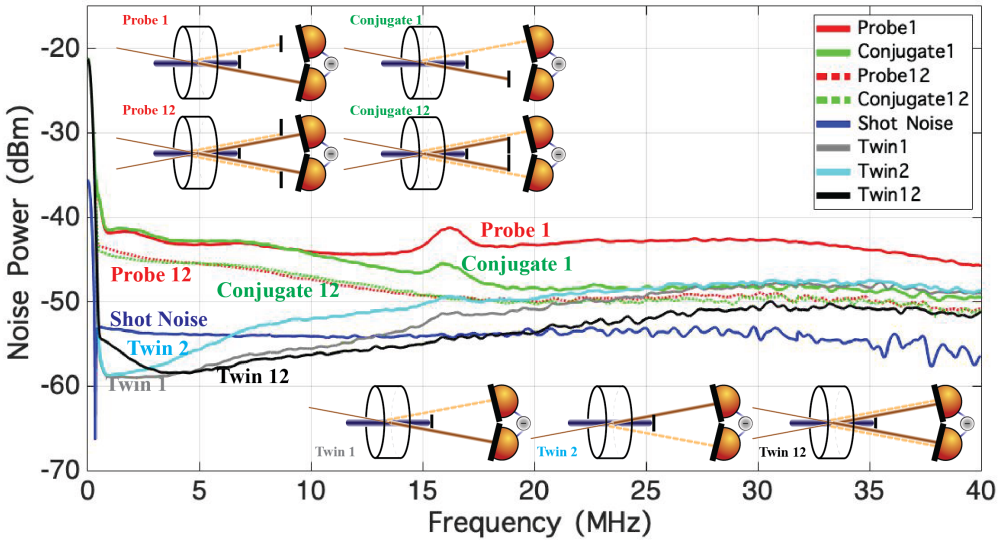

Figure 5.9: Noise spectrum of the amplified probe beam, the conjugate beam, and twin beams versus measurement frequency with the light source 3 (Ti:sapphire seed with tapered amplifier). The conditions of the 4WM process are the same as the 4WM with the light source 1 in Fig. 5.7.

to the Ti:sapphire laser can make the probe seed beams noisy. The single-seeded 4WM process from light source 3 still presents good squeezing, like light source 1, but we can see the high frequency noise is present. In the low frequency region, the 4WM process dominates so that we can still obtain a certain amount of squeezing. When we compare those two cases, we see that there is the difference in the noise. The only change is inserting the tapered amplifier, so we conclude that it must be the feedback from the tapered amplifier. The noise in the probe seed beams caused by the feedback from the tapered amplifier appears in the amplified probe beams of single-seeded 4WM at all measurement frequencies. Within the gain bandwidth of the 4WM, the amplified probe beam and the conjugate beam have the same amount of excess noise because the noise was generated through the 4WM process. When the 4WM process is faded away, there is no gain and no conjugate so the difference signal has the full excess noise of the probe at frequencies above ≈ 15 MHz.

The phase noise on the Ti:sapphire laser cannot be observed directly from the intensity noise test in Fig. 5.10. The noise spectrum of the probe beam, as shown in Fig. 5.11, from the Ti:sapphire laser shows excess noise at frequencies below 5 MHz that is similar to the excess noise profile on the amplified probe beam in Fig. 5.7. Fig. 5.10 shows the diode laser is shot-noise-limited like the Ti:sapphire laser at high frequencies. From the noise measurement of the probe beam from the diode laser, as shown in Fig. 5.11 where the beam passes through Rb vapor, it is not shot-noise-limited anymore at high frequencies. (We do not understand this.) This could explain why the noise on the diode laser introduces excess high frequency noise in the twin beams. Although the probe beam from the light source 3 is shot-noise-

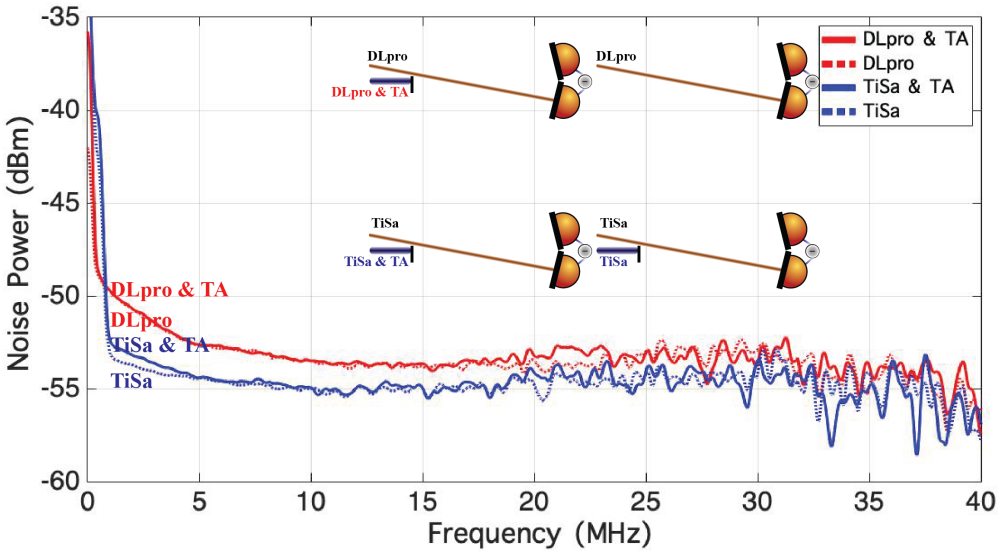

Figure 5.10: Spectra of single beam noise, from different light sources, by a single detector for each trace. The optical power of each trace is 500 μW. The red curve and the blue curve show the noise spectra of beams from a diode laser and a Ti:sapphire laser, and a tapered amplifier seeded by a diode laser and a Ti:sapphire laser, respectively. The red dashed curve and the blue dashed curve show the noise spectra directly from the diode laser and the Ti:sapphire laser without seeding the tapered amplifier. The resolution bandwidth (RBW) is 300 kHz and the video bandwidth (VBW) is 100 Hz for these measurements. The detector bandwidth is 45 MHz. The electronic noise is subtracted from these traces.

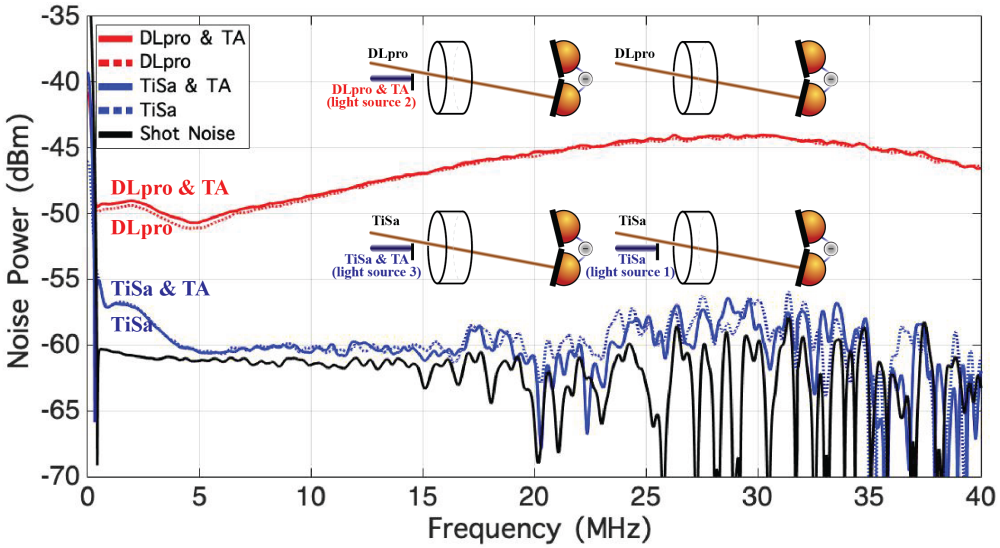

Figure 5.11: Spectra of single beam noise, from different light sources, on a single detector for each trace. The laser beams are sent through the Rb vapor at the frequency of the probe beam. The total output optical power of each trace is 100 μW. The red curve and the blue curve show the noise spectra of the probe beams with the pump source from the tapered amplifier seeded by a diode laser and a Ti:sapphire laser, respectively. The red dashed curve and the blue dashed curve show the noise spectra of the probe beams directly from the diode laser and the Ti:sapphire laser without the tapered amplifier. The resolution bandwidth (RBW) is 300 kHz and the video bandwidth (VBW) is 100 Hz for these measurements. The detector bandwidth is 45 MHz. The electronic noise is subtracted from these traces.

limited at high frequencies, as shown in Fig. 5.11, like the probe beam from the light source 1, the amplified probe beam from the light source 3 could still be noisy, as shown in Fig. 5.9, with the pump beam from the tapered amplifier.

5.3 Discussion

The semiconductor-based laser system is an essential laser source for portable squeezed light. However, there is a large amount of excess noise that appears in the twin beams when the 4WM process is pumped by a diode laser with a tapered amplifier. This noise could mostly be removed with the dual-seeded 4WM scheme. In our setup for the 4WM pumped and seeded by a Ti:sapphire laser, the squeezing can be extended to frequencies around 20 MHz by inserting a delay line into the conjugate beam. The bandwidth of the squeezing corresponds to the bandwidth of the thermal noise, the amplified probe noise or the conjugate noise. The upper-bound frequency for seeing the thermal noise is the gain bandwidth of the 4WM process. The high frequency excess noise is mainly present at frequencies outside the 4WM gain region, which can explain why the noise of the probe seed in the Rb vapor cannot be removed through intensity-balancing the twin beams.

By the comparison of the squeezed noise from three different light sources, it is clear that the excess noise is mainly added to the probe seed beam in the Rb vapor. Besides the phase noise from the diode laser system, the tapered amplifier could also feedback to the diode laser seeding source. Also, the noise from the feedback between the tapered amplifier and the seeding source can make the pump noisy. In Fig. 5.11 we don't see a clear noise difference of the probe seed beams in the Rb vapor for the light source 1 and the light source 3. There is still a small amount of high frequency noise present in the amplified probe beam in Fig. 5.9. It could be the noise from the pump beam that contributes to the noise of the amplified probe

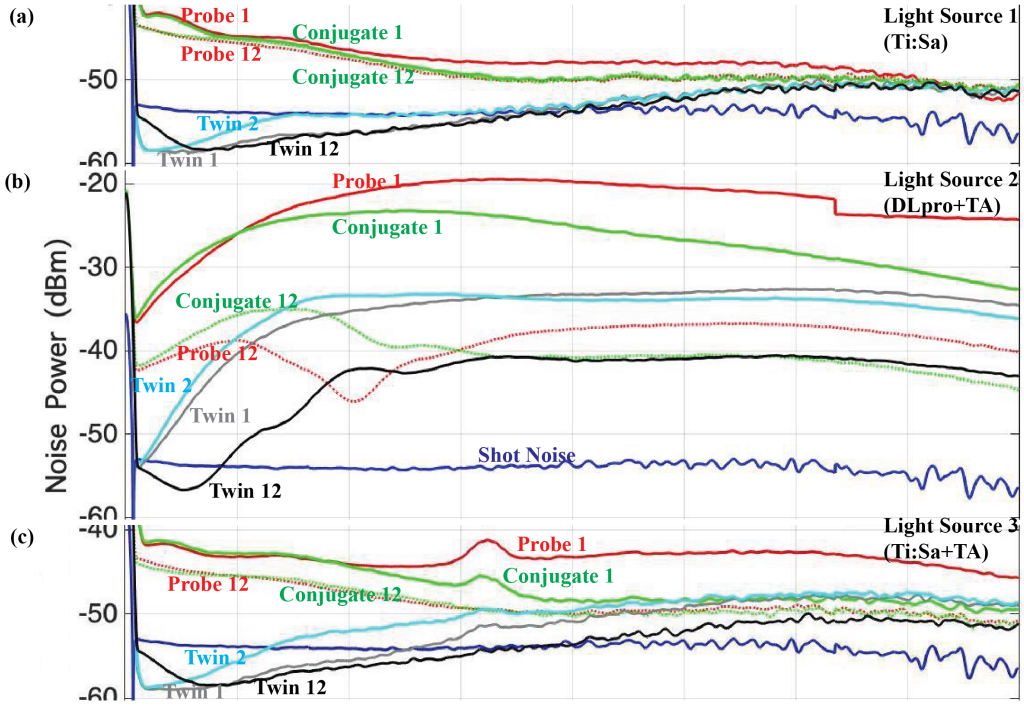

Figure 5.12: Spectra of squeezed noise from different light sources. Comparison of (a) Fig. 5.7 with the pump and probe beams from a Ti:sapphire laser, (b) Fig. 5.8 with the pump beam from a tapered amplifier and the probe beam from a diode laser, and (c) Fig. 5.9 with the pump beam from a tapered amplifier and the probe beam from a Ti:sapphire laser.

beam. In the future, we can measure the noise of the probe beam crossed by a noisy pump beam at a larger or smaller angle in a Rb vapor cell, without the 4WM gain to test this.

In the previous chapter we showed that the dual-seeded 4WM process with skew rays shows better squeezed noise than the single-seeded 4WM process pumped by a Ti:sapphire laser. We expected to see no difference between the single-seeded 4WM process and the dual-seeded 4WM process when we used the skew rays scheme. From the noise test in the previous section there is a small amount of noise in

Ti:sapphire lasers, as shown in Fig. 5.11, that can contribute excess noise to the single-seeded 4WM process at high frequencies. This excess noise on the single-seeded 4WM process can be removed with the dual-seeded 4WM scheme.

The excess noise is correlated and reproduced in both amplified probe beams of the dual-seeded 4WM process for both the skew rays scheme and the crossed rays scheme. In the previous chapter, the noise spectrum of the intensity-difference of two probe seed beams, derived from the diode laser, crossing in the Rb vapor cell, as shown in Fig. 4.5, shows the noise is reproduced in both probe seed beams and can be removed with the dual-seeded 4WM scheme. However, the noise source could be more complicated when there is too much feedback from the tapered amplifier to the diode laser. The high frequency excess noise cannot be removed completely with the dual-seeded 4WM if there is too much noise on the conjugate beam generated by the pump source from the noisy tapered amplifier, as shown in Fig. 5.8.

We know that the 4WM process dominates the noise within the gain bandwidth. The excess noise is present in the probe seed beam before it intersects with the pump beam in the Rb vapor. All the excess noise will be reproduced in both of the probe seed beams. This part of the noise is a technical noise that could be cancelled out with the dual-seeded scheme. The noise spectrum of the conjugate beam is quite similar to the amplified probe beam at low frequencies. It does not approach the shot noise level at high frequencies. This noise might come from the coupling between the noisy pump and conjugate beams.

Although the high frequency noise makes the squeezed light generated by semiconductor-based systems difficult to use as a portable quantum light source, it

still gives us a new idea to diagnose the noise source. The noise from the diode laser is present in the twin beams at high measurement frequencies. We can even see the excess noise on the amplified probe beam at low measurement frequencies. To our knowledge the noise property of Ti:sapphire lasers (light source 1) is quite clean and we do not see excess noise from the intensity noise test. Comparing the dual-seeded 4WM process with the skew rays scheme to the single-seeded process, we observed the single-seeded 4WM process has a little more excess noise. There are still some mechanisms that generate excess noise in the twin beams at high frequencies that we do not fully understand. Measurements like the one described in this chapter could help us to understand the as-yet unknown source of noise in our diode laser.

5.4 Conclusions

We have compared dual-seeded twin-beam generation and intensity-difference squeezing in the 4WM pumped by a diode laser source and a Ti:Sapphire laser source. The diode laser produces large amounts of excess noise in the intensity-difference squeezing spectrum that is not observed in a similar system pumped by a Ti:sapphire laser. We speculate the mechanism creating this noise is the phase noise that becomes intensity noise in the probe seed beam in the Rb vapor cell. The excess noise is mainly present at high frequencies because the quantum correlated twin beams suppress the excess noise at frequencies below the 4WM gain bandwidth. The dual-seeding technique also seems to be able to largely subtract the diode laser induced noise, indicating that the source of the noise is indeed the light source that

is shared by the two 4WM processes, and not the local atomic population in the nonlinear medium, which does not have to be shared in this case.

The tapered-amplifier-induced noise could also be a significant problem, as it prevents the observation of squeezing even under the dual-seeded 4WM scheme, often over much of the gain bandwidth. The excess noise seems to be in the conjugate beam when the pump source is noisy. The observation that the excess noise is not subtracted suggests that it does not come from the 4WM process. It is not clear whether or not other pump sources (fiber lasers, broad-area lasers, alkali-vapor lasers) would be able to replace the tapered amplifier and still be as portable and economical, while avoiding its noise properties. The diode laser and the tapered-amplifier noise is potentially present in any "portable" 4WM source based on these systems and should be investigated in any sensor or other measurement system relying on quantum correlations in which it is used.

Chapter 6: Concluding Remarks

In this thesis, our ultimate goal is to build a portable and affordable quantum light source using semiconductor-based laser systems such as diode lasers and tapered amplifiers. The diode laser can also be locked and frequency-narrowed simply through the feedback to the current controller. We point out what challenges we need to solve to replace the Ti:sapphire laser as a pump source for the squeezed light. For the current status we can build a portable and compact dual-seeded 4WM module with a hot Rb vapor cell and two fiber collimators for the pump and probe beams only. The squeezed light can be obtained by plugging in the fibers with laser beams from either diode laser or Ti:sapphire laser systems. The function of the fiber collimators is to satisfy the phase-matching condition easily.

6.1 Summary of Results

From our previous study with the Ti:sapphire laser system, we should be able, in principle, to obtain squeezing for all frequencies below around 20 MHz, the gain bandwidth of the 4WM process. The different group velocities of the probe and conjugate beams reduces the cut-off of the squeezing to around 5 MHz. With a $\approx$10 ns delay line in the conjugate beam path we can recover the squeezing at

higher frequencies.

Theoretically, we can see squeezing at all frequencies within the 4WM gain bandwidth (order of 20 MHz). The noise on the probe seed beam itself limits the squeezing observed at low measurement frequencies. We implemented a dual-seeded 4WM scheme that helps us to obtain squeezing at acoustic frequencies (Chapter 3). By locking the laser, dual seeding the 4WM process, and using a larger phase-matching angle, we have achieved squeezing at frequencies below 10 Hz.

With the dual-seeded 4WM, we noticed that the two-beam coupling (Chapter 4) degrades the squeezing at frequencies below the natural linewidth of the atomic transition. Two-beam coupling can be mitigated by using low probe power or non-intersecting probe beams in the gain medium. The problem also appears in the case of generating quantum-correlated images when the probe image is projected into the 4WM region in the Fourier plane. In that application we can eliminate this two-beam coupling effect by imaging the seed into the 4WM region. Along with the low-frequency squeezing technique, careful imaging should allow us to avoid the deleterious effects of two-beam coupling and enable direct quantum-correlated image measurements on a CCD camera.

Back to the single-seeded 4WM with the diode laser system, there is a large amount of excess noise that appears in the twin beams at frequencies out of the gain bandwidth for the 4WM process. In the dual-seeded 4WM scheme we showed that most of the excess noise is a correlated noise that is reproduced in both amplified probe beams and can be removed (Chapter 5).

With the results of our study of the quantum correlations of the squeezed

light we can do absolute calibrations of photodiodes for a wide frequency range of 10 Hz to 10 MHz. The scheme of the loss measurement for optical elements by using detectors with unknown quantum efficiencies has been demonstrated (Chapter 2). We developed higher order correlation functions to estimate the gain of the probe beam that also helps us to estimate the loss of the amplified probe beam in the Rb vapor. The absolute quantum efficiencies of photodiodes can be derived from the correlation functions and the loss measurements. The uncertainty level of the calibration is mainly limited by the loss measurement of the window, which is around 2% due to the temperature drifts. As compared to uncertainties of 0.5% ($k = 2$) achieved by Vahlbruch *et al.* [29] using single-mode squeezing.

6.2 Outlook and Remaining Questions

The dual-seeded 4WM scheme gives us a chance to revisit the well understood squeezed light from the 4WM process in hot Rb vapor. We observed that the diode laser has a certain amount of noise that causes excess noise, most obvious at high measurement frequencies in the single-seeded squeezed light generation. For the squeezed light obtained from the Ti:sapphire laser system there is a difference in the amount of squeezing, as shown in Fig. 4.3, Fig. 4.7, and 5.7, between the single-seeded and skew dual-seeded 4WM that suggests there is an additional unknown source of noise in the Ti:sapphire laser. We need to keep in mind that there will be excess noise when we use the quantum light source in a weaker 4WM gain region. It is important to study the mechanism of how the excess noise is added to the probe

seed beam in the Rb vapor. Can we observe similar excess noise from solid-state laser platforms? Can we use a cavity filter to remove the excess noise in the diode laser system? We did not see an improvement in the noise at high frequencies when the diode laser is locked and frequency-narrowed. However, a 40 dB improvement in phase noise can be observed by injection-locking the diode laser system as seen in Ref. [95]. This might be a solution to our noise problem. Is phase noise the main noise source of the excess noise seen in the probe beam in hot Rb vapor?

For quantum-correlated imaging we obtained intensity-difference squeezing between each piece of the probe and the conjugate images. This is a promising result for the direct measurements on a CCD camera. In order to get enough separation between the scattered pump light and twin images we need a larger phase-matching angle that also reduces the 4WM gain bandwidth. Will a smaller 4WM bandwidth affect the result of the direct measurements with a CCD camera? The small phase-matching angle limits the spatial frequency of the twin images, as shown in Fig. 4.12. If the 4WM bandwidth does not matter for the direct quantum imaging measurement, we can process the imaging with a higher spatial frequency. Furthermore, we can check the squeezing levels obtained with the dual-seeded imaging although it would be challenge to avoid the two-beam coupling with dual-seeded imaging. Method 2 (the amplified seeded beam balanced by its conjugate and a second seed that goes around the gain) in chapter 3 might be a good compromise allowing low-frequency squeezing while avoiding overlap between images.

We observed 60 Hz spikes in the low-frequency squeezing experiment. It was hard to figure out the source of this when we used the diode laser system. The noise

can be from the diode laser, the tapered amplifier, or some other pickup (ground currents in the optical table). If we compare the different light sources used in chapter 5, we hope to improve the diagnosis of the 60 Hz noise spikes and hope to obtain a clean spectrum at low frequencies.

Another application of squeezed light is for the absolute calibration of photodiodes. When we mention the applications of squeezed light we might expect to beat the traditional methods. For the photodiode calibration we cannot hope to beat the traditional calibration method unless we have better loss measurements along with the quantum correlated twin beams. We believe that it is worthwhile to make such improved loss measurement because of the intrinsic advantage of the technique that does not require previously calibrated detectors. For the loss measurements with the trap detectors, we don't need to have calibrated trap detectors, but we do need a stable coherent light source for the reference detector and signal detector since the trap detectors operate at low frequencies and need a long integration time to collect the signal. Finally, since the loss of the optical elements does not vary with the measurement frequencies, we can ask if we can perform the loss measurement simply via the twin beams with high-speed photodiodes?

Bibliography

[1] Roy J. Glauber. Coherent and incoherent states of the radiation field. *Phys. Rev.*, 131:2766–2788, Sep 1963.

[2] T. H. Maiman. Stimulated optical radiation in ruby. *Nature*, 187(4736):493–494, May 1960.

[3] Fritz P. Schäfer, Werner Schmidt, and Jürgen Volze. Organic dye solution laser. *Applied Physics Letters*, 9(8):306–309, 1966.

[4] T. W. Hänsch. Repetitively pulsed tunable dye laser for high resolution spectroscopy. *Appl. Opt.*, 11(4):895–898, Apr 1972.

[5] Marlan O. Scully and M. Suhail Zubairy. *Quantum Optics*. Cambridge University Press, 1997.

[6] David Stoler. Equivalence classes of minimum uncertainty packets. *Phys. Rev. D*, 1:3217–3219, Jun 1970.

[7] Christopher Gerry and Peter Knight. *Introductory Quantum Optics*. Cambridge University Press, 2004.

[8] Carlton M. Caves. Quantum limits on noise in linear amplifiers. *Phys. Rev. D*, 26:1817–1839, Oct 1982.

[9] G J Milburn. Multimode minimum uncertainty squeezed states. *Journal of Physics A: Mathematical and General*, 17(4):737–745, mar 1984.

[10] Carlton M. Caves and Bonny L. Schumaker. New formalism for two-photon quantum optics. i. quadrature phases and squeezed states. *Phys. Rev. A*, 31:3068–3092, May 1985.

[11] Horace P. Yuen and Jeffrey H. Shapiro. Generation and detection of two-photon coherent states in degenerate four-wave mixing. *Opt. Lett.*, 4(10):334–336, Oct 1979.

[12] Prem Kumar and Jeffrey H. Shapiro. Squeezed-state generation via forward degenerate four-wave mixing. *Phys. Rev. A*, 30:1568–1571, Sep 1984.

[13] M. D. Reid and D. F. Walls. Generation of squeezed states via degenerate four-wave mixing. *Phys. Rev. A*, 31:1622–1635, Mar 1985.

[14] M. D. Reid, D. F. Walls, and B. J. Dalton. Squeezing of quantum fluctuations via atomic coherence effects. *Phys. Rev. Lett.*, 55:1288–1290, Sep 1985.

[15] C. F. McCormick, V. Boyer, E. Arimondo, and P. D. Lett. Strong relative intensity squeezing by four-wave mixing in rubidium vapor. *Opt. Lett.*, 32(2):178–180, Jan 2007.

[16] Mark Fox. *Quantum optics: an introduction*. Oxford Master Series in Atomic, Optical and Laser Physics. Oxford Univ. Press, Oxford, 2006.

[17] Girish S. Agarwal. *Quantum Optics*. Cambridge University Press, 2012.

[18] N. J. Cerf, M. Lévy, and G. Van Assche. Quantum distribution of gaussian keys using squeezed states. *Phys. Rev. A*, 63:052311, Apr 2001.

[19] Lars S Madsen, Vladyslav C Usenko, Mikael Lassen, Radim Filip, and Ulrik L Andersen. Continuous variable quantum key distribution with modulated entangled states. *Nature Communications*, 3(1):1083, 2012.

[20] J. Aasi *et al.* (Collaboration T.L.S.). Enhanced sensitivity of the LIGO gravitational wave detector by using squeezed states of light. *Nature Photonics*, 7(8):613–619, 2013.

[21] M. Tse *et al.*. Quantum-enhanced advanced ligo detectors in the era of gravitational-wave astronomy. *Phys. Rev. Lett.*, 123:231107, Dec 2019.

[22] B. P. Abbott *et al.* (LIGO Scientific and Virgo Collaborations). Gw170817: Observation of gravitational waves from a binary neutron star inspiral. *Phys. Rev. Lett.*, 119:161101, Oct 2017.

[23] Florian Wolfgramm, Alessandro Cerè, Federica A. Beduini, Ana Predojević, Marco Koschorreck, and Morgan W. Mitchell. Squeezed-light optical magnetometry. *Phys. Rev. Lett.*, 105:053601, Jul 2010.

[24] N. Otterstrom, R. C. Pooser, and B. J. Lawrie. Nonlinear optical magnetometry with accessible in situ optical squeezing. *Opt. Lett.*, 39(22):6533–6536, Nov 2014.

[25] Nathan Killoran, Thomas R. Bromley, Juan Miguel Arrazola, Maria Schuld, Nicolás Quesada, and Seth Lloyd. Continuous-variable quantum neural networks. *Phys. Rev. Research*, 1:033063, Oct 2019.

[26] Alan Migdall. Correlated-photon metrology without absolute standards. *Physics Today*, 52(1):41–46, 1999.

[27] Giorgio Brida, Maria Chekhova, Marco Genovese, and Ivano Ruo-Berchera. Analysis of the possibility of analog detectors calibration by exploiting stimulated parametric down conversion. *Opt. Express*, 16(17):12550–12558, Aug 2008.

[28] Alberto M. Marino and Paul D. Lett. Absolute calibration of photodiodes with bright twin beams. *Journal of Modern Optics*, 58(3-4):328–336, 2011.

[29] Henning Vahlbruch, Moritz Mehmet, Karsten Danzmann, and Roman Schnabel. Detection of 15 db squeezed states of light and their application for the absolute calibration of photoelectric quantum efficiency. *Phys. Rev. Lett.*, 117:110801, Sep 2016.

[30] Vincent Boyer, Alberto M. Marino, Raphael C. Pooser, and Paul D. Lett. Entangled images from four-wave mixing. *Science*, 321(5888):544–547, 2008.

[31] D N Klyshko. Use of two-photon light for absolute calibration of photoelectric detectors. *Soviet Journal of Quantum Electronics*, 10(9):1112–1117, sep 1980.

[32] A L Migdall, R U Datla, A Sergienko, J S Orszak, and Y H Shih. Absolute detector quantum-efficiency measurements using correlated photons. *Metrologia*, 32(6):479–483, dec 1995.

[33] Sergey V. Polyakov and Alan L. Migdall. High accuracy verification of a correlated-photon-based method for determining photon-counting detection efficiency. *Opt. Express*, 15(4):1390–1407, Feb 2007.

[34] N P Fox. Trap detectors and their properties. *Metrologia*, 28(3):197–202, jan 1991.

[35] Jessica Cheung, James L. Gardner, Alan Migdall, Sergey Polyakov, and Michael Ware. High accuracy dual lens transmittance measurements. *Appl. Opt.*, 46(22):5396–5403, Aug 2007.

[36] E. Hecht. *Optics*. Pearson education. Addison-Wesley, 2002.

[37] Thomas C Larason and Jeanne M Houston. Spectroradiometric Detector Measurements: Ultraviolet, Visible, and Near-Infrared Detectors for Spectral Power. *NIST Special Publication*, 41:119, 2008.

[38] G Brida, M Genovese, and M Gramegna. Twin-photon techniques for photodetector calibration. *Laser Physics Letters*, 3(3):115–123, mar 2006.

[39] G. Brida, M. Chekhova, M. Genovese, M.-L. Rastello, and I. Ruo-Berchera. Absolute calibration of analog detectors using stimulated parametric down conversion. *Journal of Modern Optics*, 56(2-3):401–404, 2009.

[40] J Y Cheung, E Usadi, and C J Chunnilall. Laser techniques for high accuracy spectrometric measurements of parallel-sided samples. In *Fifth Oxford Conference on Spectroscopy*, pages 55–64, 2008.

[41] H. Grote, K. Danzmann, K. L. Dooley, R. Schnabel, J. Slutsky, and H. Vahlbruch. First long-term application of squeezed states of light in a gravitational-wave observatory. *Phys. Rev. Lett.*, 110:181101, May 2013.

[42] A. C. Boccara, D. Fournier, and J. Badoz. Thermo-optical spectroscopy: Detection by the mirage effect. *Applied Physics Letters*, 36(2):130–132, 1980.

[43] Christoph Haisch. Photoacoustic spectroscopy for analytical measurements. *Measurement Science and Technology*, 23(1):012001, 2012.

[44] Dmitry Budker and Michael Romalis. Optical magnetometry. *Nat. Phys.*, 3, 2007.

[45] Meng-Chang Wu, Bonnie L. Schmittberger, Nicholas R. Brewer, Rory W. Speirs, Kevin M. Jones, and Paul D. Lett. Twin-beam intensity-difference squeezing below 10 hz. *Opt. Express*, 27(4):4769–4780, Feb 2019.

[46] Sebastian Steinlechner, Jöran Bauchrowitz, Melanie Meinders, Helge Müller-Ebhardt, Karsten Danzmann, and Roman Schnabel. Quantum-dense metrology. *Nat. Photon.*, 7, 2013.

[47] Melanie Ast, Sebastian Steinlechner, and Roman Schnabel. Reduction of classical measurement noise via quantum-dense metrology. *Phys. Rev. Lett.*, 117:180801, Oct 2016.

[48] I. Ruo-Berchera, I. P. Degiovanni, S. Olivares, N. Samantaray, P. Traina, and M. Genovese. One- and two-mode squeezed light in correlated interferometry. *Phys. Rev. A*, 92:053821, Nov 2015.

[49] L A Lugiato, A Gatti, and E Brambilla. Quantum imaging. *Journal of Optics B: Quantum and Semiclassical Optics*, 4(3):S176, 2002.

[50] Kirk McKenzie, Nicolai Grosse, Warwick P. Bowen, Stanley E. Whitcomb, Malcolm B. Gray, David E. McClelland, and Ping Koy Lam. Squeezing in the audio gravitational-wave detection band. *Phys. Rev. Lett.*, 93:161105, Oct 2004.

[51] Kirk McKenzie, Malcolm B Gray, Stefan Goßler, Ping Koy Lam, and David E McClelland. Squeezed state generation for interferometric gravitational-wave detection. *Classical and Quantum Gravity*, 23(8):S245, 2006.

[52] H Vahlbruch, S Chelkowski, K Danzmann, and R Schnabel. Quantum engineering of squeezed states for quantum communication and metrology. *New Journal of Physics*, 9(10):371, 2007.

[53] M S Stefszky, C M Mow-Lowry, S S Y Chua, D A Shaddock, B C Buchler, H Vahlbruch, A Khalaidovski, R Schnabel, P K Lam, and D E McClelland. Balanced homodyne detection of optical quantum states at audio-band frequencies and below. *Classical and Quantum Gravity*, 29(14):145015, 2012.

[54] Cunjin Liu, Jietai Jing, Zhifan Zhou, Raphael C. Pooser, Florian Hudelist, Lu. Zhou, and Weiping Zhang. Realization of low frequency and controllable bandwidth squeezing based on a four-wave-mixing amplifier in rubidium vapor. *Opt. Lett.*, 36(15):2979–2981, Aug 2011.

[55] Rong Ma, Wei Liu, Zhongzhong Qin, Xiaolong Su, Xiaojun Jia, Junxiang Zhang, and Jiangrui Gao. Compact sub-kilohertz low-frequency quantum light source based on four-wave mixing in cesium vapor. *Opt. Lett.*, 43(6):1243–1246, Mar 2018.

[56] O. Jedrkiewicz, Y.-K Jiang, E. Brambilla, A. Gatti, M. Bache, L. A. Lugiato, and P. Di Trapani. Detection of sub-shot-noise spatial correlation in high-gain parametric down conversion. *Phys. Rev. Lett.*, 93:243601, Dec 2004.

[57] Jean-Luc Blanchet, Fabrice Devaux, Luca Furfaro, and Eric Lantz. Measurement of sub-shot-noise correlations of spatial fluctuations in the photon-counting regime. *Phys. Rev. Lett.*, 101:233604, Dec 2008.

[58] Giorgio Brida, Lucia Caspani, Alessandra Gatti, Marco Genovese, Alice Meda, and Ivano Ruo Berchera. Measurement of sub-shot-noise spatial correlations without background subtraction. *Phys. Rev. Lett.*, 102:213602, May 2009.

[59] G Brida, M Genovese, and I Ruo Berchera. Experimental realization of sub-shot-noise quantum imaging. *Nature Photonics*, 4(4):227–230, 2010.

[60] Nigam Samantaray, Ivano Ruo-Berchera, Alice Meda, and Marco Genovese. Realization of the first sub-shot-noise wide field microscope. *Light: Science & Applications*, 6(7):e17005, 2017.

[61] Xin Wen, Yashuai Han, Jinyu Liu, Jun He, and Junmin Wang. Polarization squeezing at the audio frequency band for the rubidium d1 line. *Opt. Express*, 25(17):20737–20748, Aug 2017.

[62] Travis Horrom, Robinjeet Singh, Jonathan P. Dowling, and Eugeniy E. Mikhailov. Quantum-enhanced magnetometer with low-frequency squeezing. *Phys. Rev. A*, 86:023803, Aug 2012.

[63] Zhongzhong Qin, Jietai Jing, Jun Zhou, Cunjin Liu, Raphael C. Pooser, Zhifan Zhou, and Weiping Zhang. Compact diode-laser-pumped quantum light source based on four-wave mixing in hot rubidium vapor. *Opt. Lett.*, 37(15):3141–3143, Aug 2012.

[64] C. F. McCormick, A. M. Marino, V. Boyer, and P. D. Lett. Strong low-frequency quantum correlations from a four-wave-mixing amplifier. *Phys. Rev. A*, 78:043816, Oct 2008.

[65] Ashok Kumar, Hayden Nunley, and A. M. Marino. Observation of spatial quantum correlations in the macroscopic regime. *Phys. Rev. A*, 95:053849, May 2017.

[66] V. Boyer, C. F. McCormick, E. Arimondo, and P. D. Lett. Ultraslow propagation of matched pulses by four-wave mixing in an atomic vapor. *Phys. Rev. Lett.*, 99:143601, Oct 2007.

[67] C. Wieman and T. W. Hänsch. Doppler-free laser polarization spectroscopy. *Phys. Rev. Lett.*, 36:1170–1173, May 1976.

[68] Kirk McKenzie, Malcolm B. Gray, Ping Koy Lam, and David E. McClelland. Technical limitations to homodyne detection at audio frequencies. *Appl. Opt.*, 46(17):3389–3395, Jun 2007.

[69] Alberto M. Marino, Jr. C. R. Stroud, Vincent Wong, Ryan S. Bennink, and Robert W. Boyd. Bichromatic local oscillator for detection of two-mode squeezed states of light. *J. Opt. Soc. Am. B*, 24(2):335–339, Feb 2007.

[70] Neil Corzo, Alberto M. Marino, Kevin M. Jones, and Paul D. Lett. Multi-spatial-mode single-beam quadrature squeezed states of light from four-wave mixing in hot rubidium vapor. *Opt. Express*, 19(22):21358–21369, Oct 2011.

[71] Jun Jia, Wei Du, J. F. Chen, Chun-Hua Yuan, Z. Y. Ou, and Weiping Zhang. Generation of frequency degenerate twin beams in Rb85 vapor. *Opt. Lett.*, 42(19):4024–4027, Oct 2017.

[72] Daniel A. Steck. Rubidium 85 d line data. *http://steck.us/alkalidata*, Nov 2019.

[73] G. S. Agarwal and Robert W. Boyd. Quantum theory of rabi sideband generation by forward four-wave mixing. *Phys. Rev. A*, 38:4019–4027, Oct 1988.

[74] Martti Kauranen, Alexander L. Gaeta, Robert W. Boyd, and Girish S. Agarwal. Amplification of vacuum fluctuations by two-beam coupling in atomic vapors. *Phys. Rev. A*, 50:R929–R932, Aug 1994.

[75] Jeremy B. Clark, Zhifan Zhou, Quentin Glorieux, Alberto M. Marino, and Paul D. Lett. Imaging using quantum noise properties of light. *Opt. Express*, 20(15):17050–17058, Jul 2012.

[76] B. J. Lawrie and R. C. Pooser. Toward real-time quantum imaging with a single pixel camera. *Opt. Express*, 21(6):7549–7559, Mar 2013.

[77] A Meda, E Losero, N Samantaray, F Scafirimuto, S Pradyumna, A Avella, I Ruo-Berchera, and M Genovese. *J. Opt.*, 19:9, 2017.

[78] A. M. Marino, R. C. Pooser, V. Boyer, and P. D. Lett. Tunable delay of einstein-podolsky-rosen entanglement. *Nature*, 457:859, February 2009.

[79] Avik Dutt, Kevin Luke, Sasikanth Manipatruni, Alexander L. Gaeta, Paulo Nussenzveig, and Michal Lipson. On-chip optical squeezing. *Phys. Rev. Applied*, 3:044005, Apr 2015.

[80] Wenjiang Fan, Benjamin J. Lawrie, and Raphael C. Pooser. Quantum plasmonic sensing. *Phys. Rev. A*, 92:053812, Nov 2015.

[81] Mohammadjavad Dowran, Ashok Kumar, Benjamin J. Lawrie, Raphael C. Pooser, and Alberto M. Marino. Quantum-enhanced plasmonic sensing. *Optica*, 5(5):628–633, May 2018.

[82] Bingjie Xu, Ziyang Chen, Zhengyu Li, Jie Yang, Qi Su, Wei Huang, Yichen Zhang, and Hong Guo. High speed continuous variable source-independent quantum random number generation. *Quantum Science and Technology*, 4(2):025013, apr 2019.

[83] Thibault Michel, Jing Yan Haw, Davide G. Marangon, Oliver Thearle, Giuseppe Vallone, Paolo Villoresi, Ping Koy Lam, and Syed M. Assad. Real-time source-independent quantum random-number generator with squeezed states. *Phys. Rev. Applied*, 12:034017, Sep 2019.

[84] A. Furusawa, J. L. Sørensen, S. L. Braunstein, C. A. Fuchs, H. J. Kimble, and E. S. Polzik. Unconditional quantum teleportation. *Science*, 282(5389):706–709, 1998.

[85] Nicolas C. Menicucci, Peter van Loock, Mile Gu, Christian Weedbrook, Timothy C. Ralph, and Michael A. Nielsen. Universal quantum computation with continuous-variable cluster states. *Phys. Rev. Lett.*, 97:110501, Sep 2006.

[86] Hidehiro Yonezawa, Samuel L. Braunstein, and Akira Furusawa. Experimental demonstration of quantum teleportation of broadband squeezing. *Phys. Rev. Lett.*, 99:110503, Sep 2007.

[87] G. Brida, L. Ciavarella, I. P. Degiovanni, M. Genovese, A. Migdall, M. G. Mingolla, M. G. A. Paris, F. Piacentini, and S. V. Polyakov. Ancilla-assisted calibration of a measuring apparatus. *Phys. Rev. Lett.*, 108:253601, Jun 2012.

[88] Paul D. Lett Ulrich Vogl, Ryan Glasser. A compact source for quantum image processing with four-wave mixing in rubidium-85.

[89] Xinrui Wei, Jiteng Sheng, Yuelong Wu, Wuming Liu, and Haibin Wu. Twin-beam-enhanced displacement measurement of a membrane in a cavity. *Applied Physics Letters*, 115(25):251105, Dec 2019.

[90] Paul D. Lett, Vincent Boyer, Alberto M. Marino, Colin F. McCormick, and Ennio Arimondo. Strong relative-intensity squeezing of light from four-wave mixing in hot rb vapor. In *Conference on Coherence and Quantum Optics*, page CTuC3. Optical Society of America, 2007.

[91] B. J. Lawrie, Y. Yang, M. Eaton, A. N. Black, and R. C. Pooser. Robust and compact entanglement generation from diode-laser-pumped four-wave mixing. *Applied Physics Letters*, 108(15):151107, 2016.

[92] Susumu Machida and Yoshihisa Yamamoto. Observation of amplitude squeezing from semiconductor lasers by balanced direct detectors with a delay line. *Opt. Lett.*, 14(19):1045–1047, Oct 1989.

[93] Robert W. Boyd, Michelle S. Malcuit, Daniel J. Gauthier, and Kazimierz Rzaęwski. Competition between amplified spontaneous emission and the four-wave-mixing process. *Phys. Rev. A*, 35:1648–1658, Feb 1987.

[94] Michelle S Malcuit, Daniel J Gauthier, and Robert W Boyd. Competition between four-wave mixing and amplified spontaneous emission. *Hyperfine Interactions*, 37(1):125–139, 1987.

[95] Yu-Hung Lai, Stuart Love, Anatoliy Savchenkov, Danny Eliyahu, Robert Moss, Andrey Matsko, and Skip Williams. Near infrared ultra-narrow-linewidth laser. In *Conference on Lasers and Electro-Optics*, 2020.